

DISCLAIMER:

This document does not meet the
current format guidelines of
the Graduate School at
The University of Texas at Austin.

It has been published for
informational use only.

Copyright

by

Avinash Nayak Pradeep

2015

The Dissertation Committee for Avinash Nayak Pradeep Certifies that this is the approved version of the following dissertation:

Pressure Induced structure-property tuning of

Two Dimensional Materials

Committee:

Deji Akinwande, Supervisor

Jung-Fu Lin, Co-Supervisor

Yaguo Wang

Neal Hall

Zheng Wang

Ananth Dodabalapur

**Pressure Induced structure-property tuning of
Two Dimensional Materials**

by

Avinash Nayak Pradeep, B.S.; M.S.

Dissertation

Presented to the Faculty of the Graduate School of
The University of Texas at Austin
in Partial Fulfillment
of the Requirements
for the Degree of

Doctor of Philosophy

**The University of Texas at Austin
May 2015**

Dedication

This is dedicated to my mother (Rooparani Hireamth) - thank you for everything you have sacrificed.

Acknowledgements

I have realized that I could not have achieved this degree if it were not for so many of my mentors and friends that I have had the privilege of knowing professionally and personally. Thank you.

My heartfelt gratitude goes out to Deji, who took a chance on me even a year before I was accepted into the program. Your capacity in believing in me is only undermined by how kind and patient you have been over the years. You have never capped my potential or restricted me in trying to expand my horizons – both professionally and personally. I have been very lucky to have you as a mentor and friend. Thank you.

I am very grateful to Afu not only for the constant mentorship over the years, but for always being there as moral support. I cannot thank you enough for giving me so many opportunities - from traveling to the many conferences to giving me liberty to try out my own ideas in your lab. Not only this, but you have always made time for me outside of your lab. Thank you for the grandiose dinners, wonderful discussions, and lasting advice over the years. You have not only had a pronounced effect on my professional carrier, but also on my character. Thank you.

Apoorva has always been there for me as a big sister and best friend. Love you for your constant, undying support over the years. My dad (Pradeep) has always kept me in good spirits regardless of what challenges I was facing. His jovial attitude toward life has served as an exemplar to live mine in juxtaposition. Love you for being our pillar. None of this would have been possible if it were not for my mother who always sacrificed for a better life for Apoorva and I. What you have done for us is minuscule in comparison to how much you believe in us. Thank you for giving me wings. Love you for being my biggest supporter.

I could not have made it so far if it were not for all of my friends and colleagues - Jeff, Cheng, Twinkle, Chuck, Markus, Sergej, Karun, Sherry, Xiaohan, Emily, Randall, Flur, Kristen, Tribhuwan, Swasti, Jason, Weinan, Jie, Zhen, Jill, Larry, Li, Fahad, Milo, Ajit, Wei, Maryam, Nassibe, Maruthi, Saungeun, Jongho, Sushant, Amritesh, Hema, Dave, Mark and Sandra. Thank you for the awesome collaborations and good times over the years. I am so proud to have known and worked with a fantastic team of undergraduates - Twinkle, Sam, Ankit and Jennifer. My oldest and dearest friends, Ivan and Avinash, thank you for keeping me levelheaded and sane. I have relied on both of you for endless laughs to keep my spirits up over these years. Thank you.

Along with my committee members – Prof. Yaguo Wang, Prof. Neal Hall, Prof. Zheng Wang, and Prof. Ananth Dodabalapur, I am also grateful to my overseas collaborators Prof. Abhishek Singh, Prof. Tianshu Li, and Prof. Chang-Quing Jin. A special note also to the fantastic MER staff, including Amy, Joann, and Jeannie for their constant help throughout my Ph.D journey. Thank you.

Contents

List of Figures	xvii
Chapter 1. Introduction	1
Significance of Two Dimensional Materials.....	1
History of Two Dimensional Materials.....	3
Tunable Properties of Two Dimensional Materials.....	5
Chapter 2. Effects of pressure on 2D materials	15
Partially Oxidized Hexagonal Boron Nitride	15
Introduction.....	16
Color Change and Optical Properties.....	17
Hydrophobicity of PO-h-BN.....	19
Characterization of PO-h-BN.....	21
Conclusion.....	26
Pressure-Induced Semiconducting to Metallic Transition in Multilayered MoS₂	27
Introduction.....	27
Electrical Conductivity and Electronic Structures.....	28
Optical Raman Vibrational Spectroscopy.....	32
Opto-Electronic Properties.....	35
XRD and HR-TEM Studies.....	37
Conclusion	36
Supplementary Figures.....	37
Pressure-Dependent Optical and Vibrational Properties of Monolayer MoS₂	48
Introduction.....	48

Results and Discussion.....	49
Supplementary Figures.....	63
<u>Pressure Based Large Doping and Metallization of Multilayered WS₂</u>	74
Introduction.....	74
Results and Discussion.....	76
Electrical conductivity and electronic structures of WS ₂	78
Optical and structural measurements of multilayered WS ₂	82
Conclusion.....	84
Supplementary Figures.....	85
<u>Chapter 3. Experimental Procedures and Setup</u>	90
Acoustic Irradiation.....	90
Sample Characterization.....	91
High-Pressure Electrical Resistance Measurements.....	92
High-Pressure Laser Raman Spectroscopy.....	93
<u>Chapter 4. Conclusions</u>	93
Partially Oxidized Hexagonal Boron Nitride.....	93
Pressure-Induced Semiconducting to Metallic Transition in Multilayered MoS ₂	93
Pressure-Dependent Optical and Vibrational Properties of Monolayer MoS ₂	95
Pressure Based Large Doping and Metallization of Multilayered WS ₂	96
<u>Chapter 5. Implications and Opportunities</u>	97
<u>List of publications</u>	104
<u>References</u>	105

List of Figures

Figure 1. Impact of 2D materials. Mind map of two-dimensional materials affecting different regions of commerce and technology. The red text indicates which sector this dissertation addresses..... 1

Figure 2. Atomically thin materials. A few of the popular members who belong to the two dimensional family..... 4

Figure 3. Variables for tuning material properties. There are three primary ways of tuning material properties – temperature, chemistry, and pressure.¹ Of these three variables, we use hydrostatic pressure (boxed) to tune properties of 2D materials by controlling the vdW interlayer distance..... 5

Figure 4. Ultrasonicator setup. (a) The power is supplied to the transducer which generates high frequency acoustic waves that irradiate the sample and solution at the probe tip. (b) Experimental setup used to produce cavitation during ultrasound irradiation..... 7

Figure 5. Diamond Anvil Cell Setup. (a) Diamond has a transmission spectrum ranging from the UV up to the IR range which makes it optimal for studying materials under high pressure. (b) The DAC under a 488nm wavelength laser to examine the Raman and PL properties of the material under high pressure (c) An optical image of the diamond culet which has the sample

placed onto it. The ruby is used as a pressure calibrant. **(d)** One of the two components of the DAC shows the diamond and the cell. **(e)** The complete DAC shown to scale. **(f)** A rendition of the DAC setup showing the two diamonds in contact with a metal gasket, and a green laser shined onto it..... 8

Figure 6. Pressure range frame of reference. A notion of the various pressures exerted in different environments..... 9

Figure 7. Material properties at ambient pressure differ in comparison to high pressure. (a) Periodic table of elements separated by their ambient pressure properties. **(b)** The elemental material properties change with increase in hydrostatic pressure. The inset shows the atomic radii between two atoms being more confined..... 10

Figure 8. Optical properties of h-BN. (a) Crystal structure of h-BN where boron (green) is connected to nitrogen (blue) in a hexagonal lattice structure. **(b)** Deep UV absorption from h-BN. Inset: Tuac’s plot showing the E_g of pristine h-BN to be 5.5eV..... 11

Figure 9. Properties of multilayered MoS₂. (a) Electronic band structure of MoS₂ shows the indirect band gap of 1.3eV. The lowest conduction band and the highest valence band is shown in blue and red respectively. **(b)** A cartoon rendition of multilayered MoS₂..... 14

Figure 10. (a) An illustration of the growth and implosion of acoustically formed bubbles which lead to the inversion of the optical and electrical properties of h-BN flakes. (b) A large decrease in transmission is observed after 60 minutes of acoustic irradiation. The inset shows the optical images of h-BN, before and after irradiation. (c) The normalized change in the h-BN optical transmission at 500nm wavelength reveal two regions of linear dependence. To is the pristine h-BN optical transmission. (d) The ultraviolet-visible (uv-vis) absorbance spectra of pristine h-BN (red) and after 60 minutes of acoustic irradiation (black). A decrease from 5.46eV to 3.97eV (27% decrease) in the optical band-gap is observed. (e) Upon irradiation the h-BN platelets undergo a transition from an insulating to a conductive phase..... 18

Figure 11. (a) Pristine h-BN platelets are observed to have a contact angle of 135° while the (b) contact angle for PO-hBN is 9°. This reduction of hydrophobicity is attributed to hydroxyl ions on the surface of the irradiated h-BN. This suggests that OH ions would likely promote the hydrophilicity to h-BN after irradiation. 20

Figure 12. (a) XPS elemental percentage concentration of various atomic species. The oxygen surface concentration increases from 2% to 41% after irradiation. (b) The Raman peak at 1367cm⁻¹ is observed before and after acoustic irradiation indicating that the crystallinity remains hexagonal. The inset depicts the E_{2g} phonon mode responsible for the Raman peak. (c) XRD shows the β-B₂O₃ peak for the irradiated h-BN which likely arises from the oxidation of h-BN during the high temperature/pressure cavitation conditions. SEM image and SEM-EDS spectra of (d) individual pristine h-BN platelet and (e) PO-hBN platelet after acoustic irradiation. The

energy peaks for N (at 0.2KeV) and B (at 0.4KeV) are observed both before and after h-BN irradiation, but O (at 0.55KeV) is detected only in PO-hBN..... 21

Figure 13. SEM EDS mapping of oxygen, nitrogen, and boron in (a) pristine h-BN and (b) PO-hBN after 60 minutes of irradiation. The presence of oxygen species is evident in the EDS mapping of POh-BN..... 23

Figure 14. (a) Comparison of the OH signal normalized to the total boron count for pristine and irradiated h-BN samples. (b) Overlay of B (red), BO (green) and OH (blue) signals for the pristine and (c) irradiated h-BN sample. The irradiated h-BN platelets reveal coverage by OH species. (d) Dynamic SIMS depth profiles of the boron signal normalized to its coverage area for the pristine (red curve) and irradiated (black curve) h-BN. A steady state is reached after 5 – 10 minutes of sputtering. Dynamic SIMS depth profiles of the (e) OH and (f) BO signals normalized to their corresponding B signals for pristine (red curve) and irradiated (black curve) h-BN. The ratios of the irradiated and pristine curves in each plot are shown in blue..... 25

Figure 15. Experimental setup and the electronic properties of multilayered MoS₂ as a function of pressure and temperature. (a) The cross-section illustration of multilayered MoS₂ with an interlayer (*c*-axis) spacing of approximately 6.5Å. (b) A 3D illustration of multilayered MoS₂ in a DAC pressure medium for compression experiments. (c) Pressure-dependent electrical resistivity of MoS₂. Three characteristic regions have been identified: semiconducting (SC), intermediate state (IS), and metallic regions. Inset: theoretically calculated pressure-dependent electrical resistivity. (d) Temperature-dependent resistivity of MoS₂ in the metallic state. Inset:

The experimental temperature-dependent semiconducting behavior of MoS₂. The solid lines serve as visual guides..... 30

Figure 16. Theoretical charge density isosurfaces of multilayered MoS₂ at different in-plane and out-of-plane strain. Charge accumulation (green) and depletion (orange) at the (a) in-plane and out-of-plane strains of 2.2 and 6.9% respectively, (b) in-plane and out-of-plane strains of 2.2 and 11% respectively, and (c) in-plane and out-of-plane strains of 5.2 and 11% respectively. (d) Same in-plane strain as in (c) but with 6.9 % out-of-plane strain..... 31

Figure 17. Raman spectroscopic results of MoS₂ at high pressures. (a) Raman spectra at representative pressure points. The inset is an illustration of the in-plane and out-of-plane vibrations of the two key modes E_{2g} and A_{1g}, respectively. (b) The Raman shifts of the two modes with increasing pressures. The solid red and blue lines serve as visual guides. (c) The difference in Raman frequencies between the A_{1g} and E_{2g} modes as a function of pressure flattens out in the IS state and rises at a smaller slope in the metallic region. The solid black line is a visual guide. (d) The FWHM for the A_{1g} and E_{2g} Raman modes across the electronic transition. A sharp drop is observed at approximately 19 GPa where MoS₂ transitions from the IS to a metallic phase. The solid red and blue lines serve as visual guides for the A_{1g} and E_{2g} mode respectively..... 34

Figure 18. Theoretical electronic structure and experimental pressure-dependent optoelectronic properties of MoS₂. (a) Theoretical calculation of the pressure-dependent band gap of multilayered MoS₂. The bandgap–pressure dependence can be modeled as a quadratic

function, $E_g = E_{go} + aP + bP^2$ was used, where $a = -70$ meV/GPa and $b = 1.13$ meV/GPa². Inset: the unit cell of MoS₂. **(b)** Theoretical band structure of multilayered MoS₂ under hydrostatic pressure of 23.8 GPa. Valence band maxima and conduction band minima are shown by red lines. **(c)** Optical switch behavior before (blue lines at 3.0 GPa) and after (red line at 21.0 GPa) the S-M transition with various laser intensities. **(d)** Current gain (defined as I_{on}/I_{off} ratio) as a function of pressure when exposed to a 532 nm (2.3eV) laser light with an intensity of 40 W/m²..... 36

Figure 19. Structural deformation in multilayered MoS₂. **(a)** Experimental pressure dependence of the lattice parameters of MoS₂. The volume uncertainty bars are within 1% of the data. **(b)** The experimental SAED patterns of both pristine and decompressed MoS₂. The patterns show that the single crystal structure with the hexagonal symmetry was not significantly affected by high pressures and can be recovered back to its original crystal structure..... 38

Figure 20. Theoretical temperature-dependent resistivity of MoS₂ at selected pressures. **(a)** Semiconducting state, and **(b)** metallic state..... 43

Figure 21. Partial density of states (PDOS) of Mo and S in multilayered MoS₂ at representative pressures. **(a)** PDOS at 0 GPa and **(b)** PDOS at 29.6 GPa. Zoom-in PDOS at **(c)** 0 GPa and **(d)** 29.6 GPa. The bands on each side of the band gap originate primarily from the *d* states of the transition metal for both 0 GPa and 29.6 GPa. For the unpressurized MoS₂, the CBM and the VBM are constituted by Mo-*d* and S-*p* orbitals while at higher pressures, contributions to

CBM from Mo-*d* and S-*p* orbitals decrease, while contributions from S-*d* orbitals increase. The Fermi level is shown as the dotted line. 43

Figure 22. Raman intensity ratio. $I_{A_{1g}}/I_{E_{2g}}$ ratio as a function of pressure shows an increase in the IS region. The maximum intensity ratio is observed in the metallic state. The inset shows the relative intensities of the E_{2g} and A_{1g} peaks at selected pressures..... 44

Figure 23. Theoretically predicted phonon bands at representative pressures. The results indicate that the splitting in the bands increases with increasing pressure. The E_{2g} (blue line) and A_{1g} (red line) modes are identified from the dispersion curves at the Γ point and their frequencies at ambient conditions are 375.5 cm^{-1} and 405.5 cm^{-1} , respectively..... 45

Figure 24. Theoretically-predicted XRD results for multilayered MoS₂ as a function of pressure. The *d*-spacings of representative lattice planes as a function of pressure. No new peaks are observed..... 45

Figure 25. Electron microprobe analyses of the multilayered MoS₂ sample. (a) HR-TEM image of the honeycomb structural arrangement of the multilayered MoS₂. Inset: FFT image of the pristine multilayered MoS₂ sample. (b) Cross-sectional HR-TEM image of a multilayered MoS₂ before compression showing the interlayer distance to be approximately 6.5 Å. (c) TEM-EDX spectra of the multilayered crystalline MoS₂ after decompression. (d) SEM-EDX spectra

for the multilayered MoS₂. Inset: SEM images are shown before loading and after decompression..... 46

Figure 26. Pressure-strain relation and the theoretical band gap dependence on strain. (a)

Pressure relationship to compressive strain, which allows correlation of the applied pressures in this work to strain. The red line is a quadratic fit to the data. **(b)** Band gap reduction with normal compressive strain applied to multilayered (bi-layer, tri-layer, four-layer, five-layer, six-layer and bulk) MoS₂. **(c)** Predicted critical strain threshold ($|\epsilon_{th}|$) as a function of the number of layers. The critical strain threshold is the strain corresponding to the closure of the band gap..... 47

Figure 27. Electrical resistance behavior with temperature. No

superconductivity of multilayered MoS₂ is observed at ~36 GPa..... 47

Figure 28. Structural and Vibrational Properties of Monolayer MoS₂ Polytypes. (a)

Schematic atomic arrangements of the monolayer MoS₂ showing the *a* (in-plane direction) and the cross-section *c* (out-of-plane) view of the monolayer 1T-MoS₂, 1T'-MoS₂ and 2H-MoS₂. **(b)**

Raman active modes of the MoS₂ family. For the 1T'-MoS₂, the J₁ mode is composed of two Raman active modes that are close to one another and appear as one peak at room temperature.

(c) Raman active modes for the restacked monolayer 1T'-MoS₂ and monolayer and bulk 2H-MoS₂. The J₁, J₂, and J₃ modes are only prominent in the 1T'-MoS₂ phase..... 51

Figure 29. Pressure-Dependent Lattice Vibrational Properties of Monolayer 1T'- and 2H-MoS₂. Representative Raman spectra of the monolayer (a) 2H-MoS₂ and (b) 1T'-MoS₂ at high pressures. For the 2H-MoS₂ polytype, the E_{2g} mode diminishes, while the dominant Raman modes are J₂, E_{2g}, and A_{1g} for 1T'-MoS₂ at pressures above 27 GPa. (c) Pressure-dependent Raman frequencies with variation in pressure for the five Raman active modes. The J₃ merges with the E_{2g} mode at around 10 GPa while the J₁ diminishes at 27 GPa. The solid line indicates the theoretical agreement with the J₁, J₂, and J₃ modes and further supports the phonon merging of the J₃ and E_{2g} modes. (d) Applied strain is plotted with respect to the energy required to compress the in-plane and out-of-plane bonds, suggesting that the in-plane mode vibration is suppressed at higher pressures. Inset: Schematic representing the application of strain in the in-plane direction (ϵ_x, ϵ_y) (upper inset) and out-of-plane (ϵ_z) directions..... 53

Figure 30. Pressure Modulated Photoluminescent Properties of Monolayer 2H-MoS₂. (a) Representative PL spectra as a function of pressure. An increase in the band gap with increasing pressure and then the diminishing of the PL signals at ~16 GPa indicates a direct-to-indirect band gap shift. (b) Derived band gap at high pressures. Extracted from the Lorentzian fit from the PL peaks, the band gap is shown to increase as a function of pressure. Red solid line: a polynomial fit to the experimental data described by $E_g = 1.88 + 0.03P - 8.59 \times 10^{-4}P^2$ where E_g is optical band gap and P is pressure. Inset: The theoretical prediction of the direct-to indirect band gap transition. (c) Band gap diagrams at K, Λ , and Γ point at two representative pressures of 0 GPa and 22.3 GPa depicting the direct to indirect transition. Here D and I indicate the direct and indirect band gaps respectively. The observed direct and indirect band gap values are also presented for clarity. At 0 GPa, the E-k diagram indicates a direct-band gap between the CBM

and the VBM, while at 22.3 GPa, band gap shift from direct (from in between K-K' points) to indirect in between K- Λ points at 22.6 GPa that agrees with the experimental observations. At around 67.9 GPa the valence band maxima (VBM) and the conduction band minima (CBM) cross the Fermi level, leading to a semiconductor-to-metal transition..... 57

Figure 31. Electronic Structures of the MoS₂ Polytypes under Hydrostatic Pressure. (a)

Band gap energies of the polytypes as a function of pressure. (a) Below 22.3 GPa, an increase in the direct band gap is observed for the monolayer 2H-MoS₂. While for higher pressure, the band gap decreases with strain and closes at 67.9 GPa indicating a metallization transition. A smaller critical pressure of 39.2 GPa and 29.5 GPa is observed for the bilayer and trilayer 2H-MoS₂ respectively. (b) Hydrostatic pressure effects on monolayer, bilayer, trilayer, bulk MoS₂ and 1T'-MoS₂. A metallic state is more easily reached in the bulk state since more interlayer interactions are present..... 60

Figure 32. Vibrational and Optical Properties of Bulk and Monolayer 2H-MoS₂ at High Pressures. (a)

Intensity ratio of the A_{1g} and E_{2g} peaks. The E_{2g} mode is observed to diminish in comparison to the A_{1g}. The insets show the relative intensities of the E_{2g} and A_{1g} peaks at selected pressures. (b) Pressure dependence of the Raman frequencies of the A_{1g} and the E_{2g} modes as a function of pressure. The behavior of these vibrational Raman modes in monolayer 2H-MoS₂ at high pressures (blue circles) deviates significantly from that of the bulk counterpart (red circles) due to the absence of interlayer interactions. Inset: representative vibrations involved in A_{1g} and E_{2g} modes. The A_{1g} modes originate from transverse vibrations of S-S atom, however the E_{2g} mode emerges from longitudinal vibrations of Mo and S atoms in opposite

directions. (c) Raman frequency separation between the A_{1g} and E_{2g} peak as 1) a function of pressure for monolayer and bulk 2H-MoS₂. Inset: representative Raman spectra highlighting the separation at 0 GPa and 30.8 GPa. The in-plane A_{1g} mode becomes more dominant in intensity than the E_{2g} past ~16 GPa for the monolayer 2H-MoS₂. (d) PL FWHM with pressure up to 16 GPa. The black lines serves as visual guidelines..... 63

Figure 33. Modeling of hydrostatic pressure on monolayer MoS₂ (a) Compression of atoms plotted with respect to energy required to compress in-plane (x, y) and out of plane (z) bonds. (b) Compression of atoms is plotted with respect to pressure. Till 20 GPa pressure there is equal compression in all the three direction. After 18 GPa Pressure compression along z direction becomes more favorable. Inset: Schematic representing the compression of atoms in the in-plane direction (upper inset) and out-of-plane directions..... 64

Figure 34. Raman Spectroscopic Results of Restacked 1T'-MoS₂ and monolayer 2H-MoS₂ at High Pressures. (a) FWHM of J_1, J_2 and J_3 Raman modes. The J_3 mode tends to saturate at 10 GPa while J_2 and J_3 increase in FWHM. (b) The FWHM of the E_{2g} and A_{1g} increases with pressure. (c) The FWHM of the E_{2g} and A_{1g} Raman modes for 2H-MoS₂. The FWHM is notably smaller for the 2H-MoS₂ monolayer than the 1T'-MoS₂ since the J_3 mode merges with the E_{2g} mode..... 65

Figure 35. Phonon Dispersions for Monolayer 1T'-MoS₂ at representative pressures. The Raman active modes for 1T'-MoS₂ are highlighted with different colors for clarity at **(a)** 0 GPa and **(b)** 23 GPa. The Raman active A_{1g}, E_{2g}, J₁, J₂ and J₃ modes are identified from the dispersion curves at the Γ point. As can be seen in case of 1T'-MoS₂ three new modes J₁, J₂ and J₃ appear, whereas the frequency of the E_{2g} mode decreases significantly compared to bulk MoS₂. The J₃ mode merges with the E_{2g} mode at ~10 GPa..... 65

Figure 36. Raman Intensity Map of 1T'-MoS₂. The pressure dependence Raman shows the shift and broadening of the 1T'-MoS₂ Raman active modes. The dominant Raman active modes at high pressure are J₂, E_{2g}, and A_{1g}. 66

Figure 37. Raman Shift with Pressure. The pressure dependence of the Raman modes for the monolayer 2H and 1T'-MoS₂ polytypes compared to the bulk 2H-MoS₂ analog in their semiconducting (SC) and metallic (M) regime. 67

Figure 38. Reversible Pressure Effects on Monolayer MoS₂. **(a)** PL of from monolayer MoS₂ before and after hydrostatic pressure of 30 GPa is applied across the monolayer 2H-MoS₂. **(b)** The PL for the 1T'-MoS₂ and 2H-MoS₂ at 0 GPa. The 1T'-MoS₂ does not show PL behavior. **(c)** Upon decompression, the Raman active A_{1g} and E_{2g} modes compare well with the Raman spectra with increasing pressure, suggesting that the pressure effects are reversible. **(d)** Pristine and

relaxed 1T'-MoS₂ show the J₁, J₂, and J₃ active modes, indicating that the pressure effects are reversible..... 68

Figure 39. FWHM of the PL Spectra from Monolayer MoS₂. (a) The FWHM map showing an increase with hydrostatic pressure at 0.6 GPa (b) 12.5 GPa and (c) 21.3 GPa show the diminishing of the PL peak suggesting that the PL at high pressures is unresolvable past 16 GPa at room temperature. The black dots represent where the peaks are diminished into the background noise..... 69

Figure 40. Fluorescence Spectra Shift in Ruby. The R₂ and R₁ ruby luminescence peaks are used to measure the pressure shift. The evolution of the PL spectra from ruby is used as a calibrant to measure the pressure experienced by the sample..... 70

Figure 41. Relation between Volume Strain and Pressure for 2H-MoS₂ Family. 2L, 3L and Bulk Follow same trend and the data can be fitted to a third order polynomial gives as $P = -0.36 + 59.81\varepsilon + 137.96\varepsilon^2 + 325.93\varepsilon^3$. However 1L depicts a completely different behavior, the polynomial fit of 1L data can be given as $P = 0.39 + 101.24\varepsilon - 220.72\varepsilon^2 + 446.7\varepsilon^3$. These different behaviors arise due to absence of interlayer interaction for monolayer MoS₂. Inset: 2L, 3L and bulk have almost same dependence between volume strain and pressure..... 71

Figure 42. Band Structure and Density of States for the 1T'-MoS₂ Monolayer. (a) At 0 GPa pressure and (b) 30 GPa. The monolayer 1T'-MoS₂ is metallic and becomes more metallic under hydrostatic pressure. Upon application of hydrostatic pressure the hybridization between Mo *d*-orbitals (mainly d_z^2 , d_{xy} and $d_{x^2-y^2}$) and S *p*-orbitals increases, there is an increase in the overlap between conduction and valence bands, increasing the extent of metallization.... 72

Figure 43. (a) Variation in slab thickness (c_{2L}) and in-plane lattice parameter *a* under hydrostatic pressure . Illustration of slab thickness for (b) bulk and (c) 1L, 2L and 3L MoS₂..... 73

Figure 44. Pressure-induced metallization of the multilayered WS₂ in a diamond anvil cell.

(a) Pressure-dependent resistivity (ρ) as function of pressure at selected temperatures shows a six order change in resistivity leading to the gradual metallization at higher pressures. (b) Temperature-dependent resistivity of the multilayered WS₂ at given high pressures shows a change in $d\rho/dT$ from negative to positive for the semiconducting to metallic state, respectively..... 77

Figure 45. Metallization mechanism of the multilayered WS₂ as a function of hydrostatic pressure. (a) The temperature-pressure contour shows the transition region from the semiconductor to metallic region that is derived from experimental electrical conductivity measurements in a DAC. The dashed line is plotted to highlight the metallization P-T boundary

as well as the overall negative slope of the transition. **(b)** The Arrhenius plot shows the activation energy exponentially decreases with pressure indicating a gradual metallization past ~22 GPa. Estimates of the semiconducting bandgap are obtained using $\ln R \propto E_g/2k_B T$ in the 50–100 K range. The value of the energy gap was derived from the resistance measurements decreased a lot with increasing of the pressure. **(c)** Band gap diagrams at M, K, and Γ point at three representative pressures of 0, 20.4, and 39.5 GPa from theoretical calculations depict the closing of the bandgap from 1.3 eV to 0 eV. At 39.5 GPa, the VBM and the CBM are shown to cross the Fermi level, suggesting a complete metallization. The increase in interactions between the orbitals are show with the increase in pressure. 79

Figure 46. Electronic carrier dynamics of the multilayered WS₂ as a function of pressure.

(a) The resistivity ratio (r_p) shows that above 22GPa, $r_p > 1$, which signifies a metallic state while at lower pressures, $r_p < 1$ is observed. **(b)** The carrier density increases by a factor of two in carrier concentration from 10^{19} cm^{-3} at 15 GPa to 10^{21} cm^{-3} at 35 GPa in the semiconductor and metallic region respectively. In comparison to the carrier density at 0 GPa, we observe a four order increase in magnitude.² **(c)** The mobility decreases by two orders of magnitude signifying more interlayer interaction. The mobility in the material decreases in the metallic state..... 81

Figure 47. Optical and structural properties of the multilayered WS₂ under high pressure.

(a) *In-situ* XRD shows that the sample remains in the hexagonal structure up to 60 GPa. The *c* axis is more compressible than the *a* axis at pressures below approximately 22 GPa and becomes

much less compressible at pressures higher than 22 GPa where the metallization occurs. The dashed grey line shows the S-M transition pressure at ~22 GPa at 280K. **(b)** Raman profiles for selected temperatures and pressures. With increasing temperature, the A_{1g} mode becomes more prominent while the $2LA(M)$ is suppressed (left panel). Applied pressure suppressed the E_{2g} mode (right panel). **(c)** Pressure-dependent Raman map showing phonon hardening for both the E_{2g} and A_{1g} modes. The solid lines show the theoretical overlay which is in good agreement with observed experimental results. **(d)** Temperature-dependent Raman map indicating phonon softening from at a rate of $-0.02 \text{ cm}^{-1}/\text{K}$ and $-0.01 \text{ cm}^{-1}/\text{K}$ for the E_{2g} and A_{1g} modes respectively..... 83

Figure 48. The diamond anvil cell setup. **(a)** Schematics of the diamond anvil cell is used for studying multilayered WS_2 at quasi-hydrostatic high-pressure conditions. The interlayer interactions (indicated by the blue glow) between the layers promote the metallization of WS_2 . **(b)** Representative optical image of the WS_2 sample in a DAC at ~37 GPa. The multilayered WS_2 is connected to four gold electrical probes for measuring the electrical resistivity in a DAC and the diameter of the DAC surface is 300 μm 85

Figure 49. Comparison of high-pressure behavior of multilayered WS_2 and MoS_2 . **(a)** Due to the pressure resilience of WS_2 in comparison to MoS_2 , the theoretical bandgap with change in hydrostatic pressure of MoS_2 and WS_2 show the metallization of MoS_2 to occur at a faster rate (eV/GPa) than WS_2 . **(b)** Larger out-of-plane (c -axis) strain is experienced in comparison to in-plane (a -axis) for both WS_2 and MoS_2 . In comparison to WS_2 , MoS_2 experiences more strain

along the *a*-axis as well as the *c*-axis. **(c)** In-plane Raman pressure dependence ($\text{cm}^{-1}/\text{GPa}$) of WS_2 is smaller than MoS_2 suggesting that the W atom is more resistant to hydrostatic pressure. The transition pressure for a S-M transition for MoS_2 is lower than WS_2 , but interestingly we do not observe as drastic of a drop in resistivity in WS_2 . When comparing the resistivity values of MoS_2 and WS_2 at semiconductor (~ 10 GPa) and metallic (~ 36 GPa) regions, we observe a six order of magnitude drop in WS_2 86

Figure 50. Carrier density variation with temperature and pressure. The carrier density increases by two orders of magnitude from ~ 15 GPa to ~ 35 GPa..... 87

Figure 51. Lattice distortion with increase in hydrostatic pressure. Theoretical calculations agree with experimental results show distortion along the out-of-plane (*c*-axis) and in-plane (*a*-axis) axis. The *c*-axis is more compressible in comparison to the *a*-axis due to weak Van der Waals in-between layers..... 88

Figure 52. Raman full width half max, pressure and temperature dependence. **(a)** The pressure and **(b)** temperature dependence of the E_{2g} and A_{1g} Raman modes and the associated full width half max (FWHM). **(c)** The intensity ratio between the A_{1g} and E_{2g} peaks show the E_{2g} mode being repressed at higher pressures. **(d)** The intensity ratio between the A_{1g} and E_{2g} peak shows the A_{1g} peak decreasing at higher temperatures..... 89

Figure 53. Horn position for ultrasonication irradiation. For optimal acoustic irradiation of h-BN, the horn tip needs to be 10 cm above the base of the 200ml beaker..... 90

Figure 54. Designer ultrasonication chamber. This setup would allow for the stability of the sample while the ultrasonication irradiation is in progress. 91

Figure 55. XPS sample preparation. To avoid oxide signals from the substrate, the samples (before and after processing) were placed directly on the o-ring such that the substrate did not play any effect on the sample signal. 92

Figure 56. Procedure to avoid external contamination. The main causes of contamination are that the sample is exposed to air (i.e. not in a vacuum sealed container), the needle tip that is being used is not clean, and the target transfer substrate is not clean..... 94

Figure 57. Sample loading in a DAC. (a) Two samples gas loaded in a DAC with the ruby which can be probed using optical spectroscopy. (b) One sample c-BN loaded in DAC with four probes connected for electrical resistivity measurements..... 96

Figure 58. Setup for measuring Raman under high pressure. The completed configuration of the DAC and the objective microscope for Raman spectroscopy under high pressure..... 97

Chapter 1. Introduction

Significance of Two Dimensional Materials

Before delving into a research topic, it is important to understand the significant impacts and implications of the research that will be undertaken. Looking back at the research done on silicon, the study of its superior behavior to other semiconductors and the great versatility of silicon dioxide manufacturing process has led to its current dominance in the semiconductor industry. Similarly, it is projected that two dimensional materials also exhibit properties that could play a critical role in future technologies. The projected technological impact of 2D materials include intelligent clothing,³ medical diagnostics,⁴ energy harvesters,⁵ tunable materials,⁶ energy storage,⁷ personal care,⁸ and flexible electronics^{9,10} (**Figure 1**). Due to the potential impact that 2D materials may have to augment current technologies, further investigation relating to their material and electronic properties need to be undertaken.

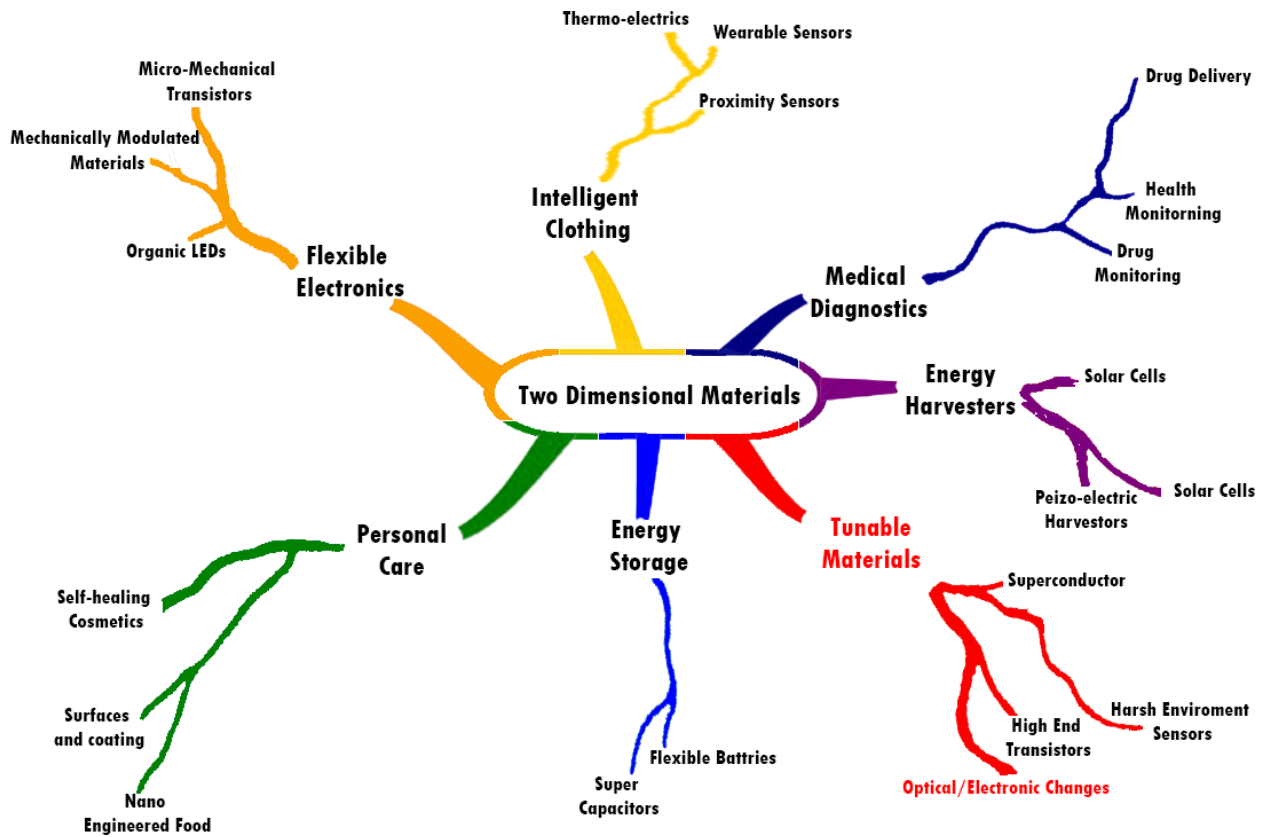


Figure 1. Impact of 2D materials. Mind map of two-dimensional materials affecting different regions of commerce and technology. The red text indicates which sector this dissertation addresses.

History of Two Dimensional Materials

The story of isolating a single atomic layer of any material has been an improbable one. For a long time, the research community thought that stable monolayer two-dimensional materials may not exist.⁶ Theorists predicted that an atomically thick material would most likely disintegrate at any finite temperature due to sources of thermal fluctuations. The basis for this expectation of instability is the Mermin-Wagner theorem,¹¹ which states that crystalline order is impossible in two-dimensional structures. This has been interpreted as saying that a free-standing, two-dimensional material would be disrupted by thermodynamic forces and therefore stable 2D materials could not exist.^{11,12} Moreover, experimentally, it was also found that the melting points of thin film materials rapidly reduced with decreasing film thickness^{13,14} which made it improbable for a truly 2D material to exist at room temperature.

Thought to be an impossible goal for many decades, the isolation of a single layer of carbon, called graphene, was successfully performed in 2004 by Nobel laureates Geim and Novoselov¹⁵. The clear evidence of finite sized free-standing graphene has been explained by arguing that small ripples (therefore, not truly flat) protect graphene from disruption, thereby making the Mermin-Wagner theory inapt. Examining this first 2D isolated material, graphene, has shown exceptional charge transport, thermal, mechanical, and optical properties.^{4,12} It was found that these astounding properties were not limited to graphene and could be extended to other 2D materials.

One such material is hexagonal boron nitride (h-BN), composed of boron and nitrogen atoms in a hexagonal lattice exhibit excellent dielectric and optical properties.^{16,17} Along with h-BN, various other layered transition metal dichalcogenides (TMDs), demonstrate intriguing physical and chemical properties.^{18,19} These TMDs are comprised of stacked quasi-two-dimensional

sheets of metal atoms covalently bonded with two sheets of chalcogen atoms above and below them. Along with these examples, a whole host of 2D materials (**Figure 2**) with interesting and special properties allow for exciting properties to be investigated. Of these 2D materials, this dissertation focuses on the tunability of the optical and electronic properties of h-BN, MoS₂, and WS₂.

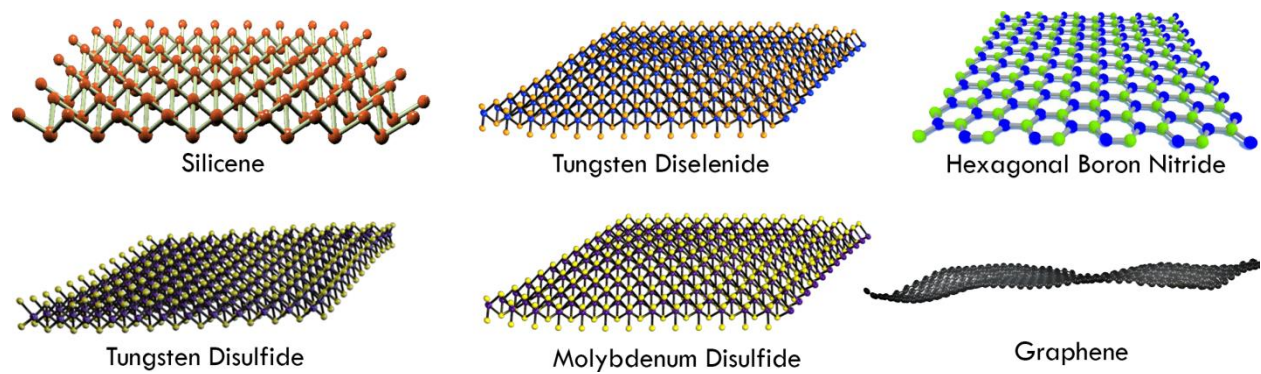


Figure 2. Atomically thin materials. A few of the popular members who belong to the two dimensional family.

Tunable Properties of Two Dimensional Materials

Attributed to the high anisotropy and crystal structure, the optical and electronic properties of TMDs can be tuned by reducing its dimensions (vertical confinement, i.e. few layers to monolayer, and lateral confinement i.e. nanoribbons), intercalations (to augment interlayer interactions, or to separate layers), creating heterostructures (vertically or laterally stacked), alloys, applying a gate bias, altering temperature, or by applying strain or pressure onto the material (**Figure 3**). Using hydrostatic pressure, the vdW can be varied so that the interactions between the 2D layers allows for changes in its electronic and structural properties.

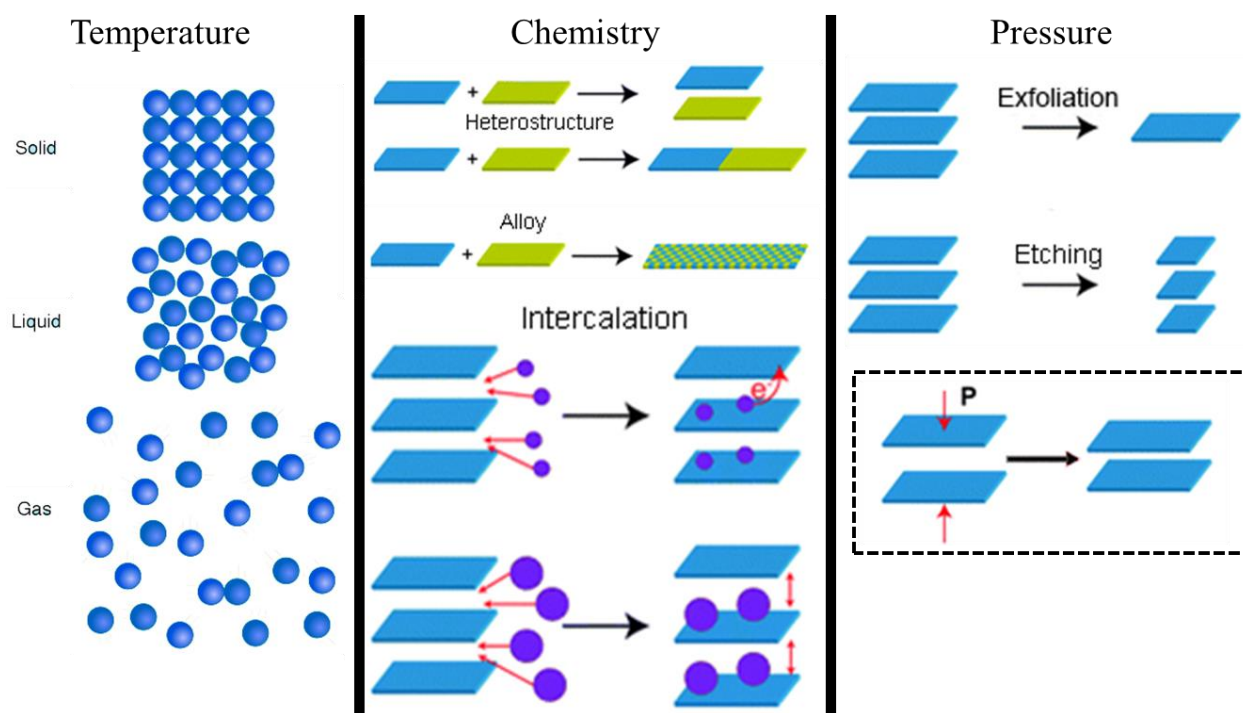


Figure 3. Variables for tuning material properties. There are three primary ways of tuning material properties – temperature, chemistry, and pressure.¹ Of these three variables, we use hydrostatic pressure (boxed) to tune properties of 2D materials by controlling the vdW interlayer distance.

Unlike graphene which has an sp^2 hybridization, multilayered TMDs are coupled with d-orbital electronic states and due to the small vdW gap. This allows for strong chalcogen- chalcogen

atom interlayer interactions under axial compression which allow for modulation of its structural and electronic properties. There are three prominent ways to induce pressure onto 2D materials – transferring 2D materials onto a flexible substrate, applying local strain by intercalating and functionalization, and applying hydrostatic pressure. The majority of the theoretical studies however, have concentrated their efforts on strain (i.e. uniaxial or biaxial strain) engineering electronic properties of TMDs,²⁰⁻²² allowing for better understanding on the strain-induced direct-to-indirect band gap (D-to-I) transition²³ as well as a semiconductor-to-metal (S-M) transition.^{21,24} Compared to these methods, applying hydrostatic pressure allows for dramatic changes in the structural and electronic properties.

High Frequency Ultrasonication

Ultrasound refers to inaudible sound waves with frequencies that range in 16KHz-500MHz, which is above the upper limit of human hearing. This frequency can be transmitted through any elastic medium including solids and liquids. In fact, it is a common technique which is used to mix immiscible liquids. Here, we focus our efforts on low frequency ultrasound (20kHz) which deliver high power onto the medium (**Figure 4**). This frequency generates cavitation bubbles in the liquid. During the cavitation phenomenon, local regions generate hotspots of high temperature (~5000 K) and high pressure (~0.18 GPa) with extremely high cooling rates (>1010K/s) in liquid solution²⁵.

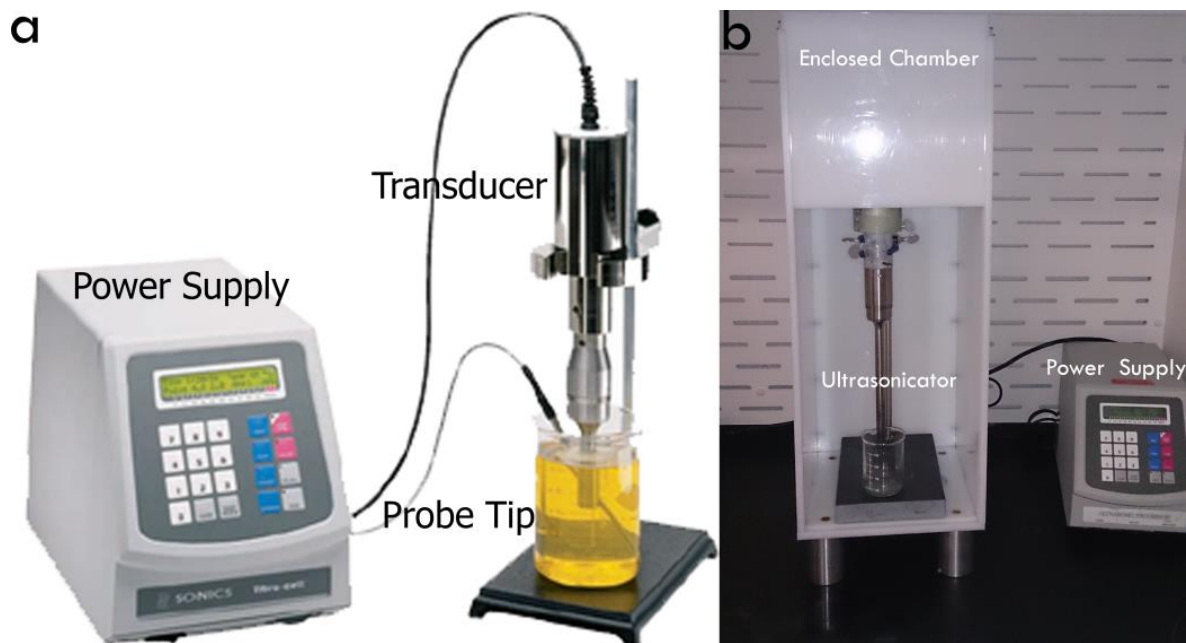


Figure 4. Ultrasonicator setup. (a) The power is supplied to the transducer which generates high frequency acoustic waves that irradiate the sample and solution at the probe tip. (b) Experimental setup used to produce cavitation during ultrasound irradiation.

This ultrasonication technique has two significant challenges. The first is that for the material to be exposed to high pressure and temperature conditions, the material needs to be immersed in a liquid which could functionalize the material while undergoing ultrasonication. The second is that the pressure and temperature conditions cannot be controlled and is intense at the cusp of the ultrasonication probe horn and sporadic past this vicinity.

Diamond Anvil Cell (DAC)

To controllably induce hydrostatic pressure onto materials, National Bureau of Standards discovered the DAC in 1959. In 56 years, spectroscopic research using the DAC has allowed for diverse materials (inorganic, organic, biological, and polymeric compounds) to be studied.²⁶ Since the diamond windows and certain metal gaskets are transparent to a wide range of the electromagnetic spectrum in comparison to other materials (**Figure 5a**), many optical and x-ray probes can be implemented. Due to the hardness of diamond (Mohs hardness of 10), high

pressures can be generated by a diamond anvil cell (DAC), which allows for the optical probing of materials at extreme environments (**Figure 5b**). As a calibrant of pressure, the red shift in ruby fluorescence is used to examine the pressure experienced at different pressures (**Figure 5c**). The DAC, a relatively small apparatus, (**Figure 5d-f**) allows us to study materials under extreme pressures up to 50GPa.

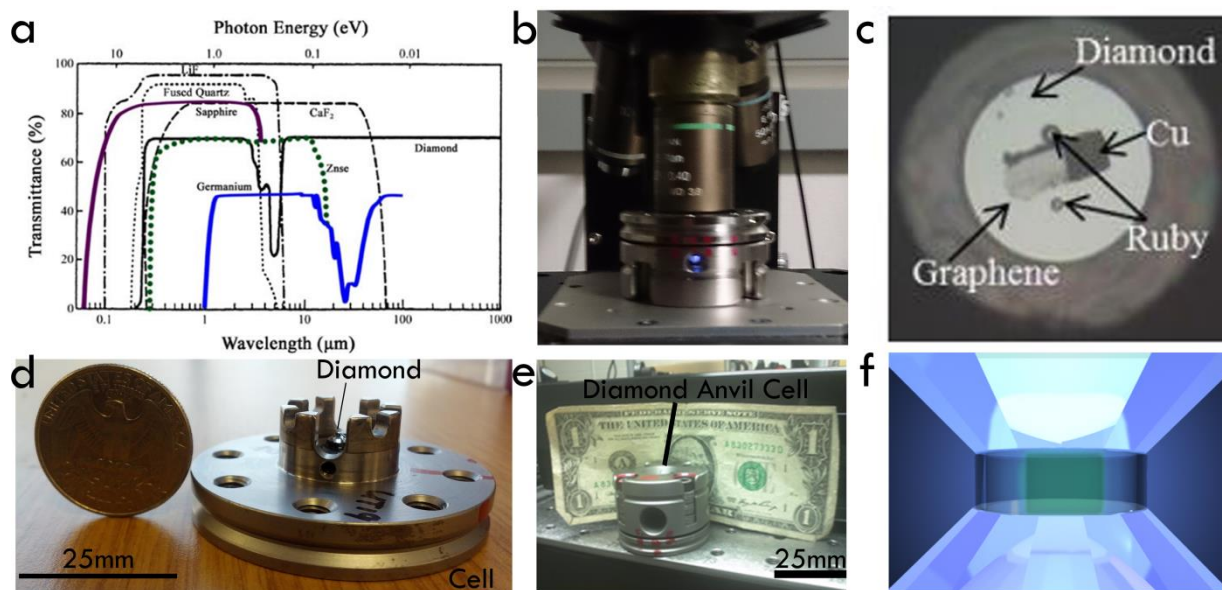


Figure 5. Diamond Anvil Cell Setup. (a) Diamond has a transmission spectrum ranging from the UV up to the IR range which makes it optimal for studying materials under high pressure. (b) The DAC under a 488nm wavelength laser to examine the Raman and PL properties of the material under high pressure (c) An optical image of the diamond anvil cell which has the sample placed onto it. The ruby is used as a pressure calibrant. (d) One of the two components of the DAC shows the diamond and the cell. (e) The complete DAC shown to scale. (f) A rendition of the DAC setup showing the two diamonds in contact with a metal gasket, and a green laser shined onto it.

The way the DAC generates high pressure is implicit by the definition of pressure: $P=F/A$, where P is the pressure, F is the force, and A is the cross-sectional area that the force exerts upon.

Applying small force upon a very small area, allows for pressure to be generated up to 300 GPa.

To understand how high pressure the DAC can reach, it's imperative to have a frame of

reference (**Figure 6**). Ambient pressure is 1.01×10^{-4} GPa (101.325 kPa) while the center of the earth is 600 GPa.²⁷

Blood Pressure	~2.1E-7 GPa
Atmospheric Pressure	~4.0E-4 GPa
PDMS Ultimate Strength	~2.2E-3 GPa
Elephants Foot	~5.4E-5 GPa
Girls' Stiletto Heels	~4.3E-3 GPa
TauTona Mine	~9.8E-2 GPa
Deepest Point of The Ocean	~0.1 GPa
Water Solidifies at 300K	~1 GPa
Center of the Earth	~360 GPa

Figure 6. Pressure range frame of reference. A notion of the various pressures exerted in different environments.

The ability of hydrostatic pressure to induce these effects, allows for the elemental material properties to change. Variation in bond length, angles, and electric energies can be varied with pressure further allows for the exploration of material properties to change by varying pressure (**Figure 7**). Considering these hydrostatic high pressure effects on materials, several consequences can result. Some of these are pressure induced phase transitions, large frequency shifts induced by pressure (i.e. change in ω -k profiles), energy and k-vector relation (i.e. change in E-k profiles), splitting of degenerate vibrations (i.e. deconvolution of phonon modes), bandgap opening and closing²⁸, superconductivity²⁹, and structural changes³⁰.

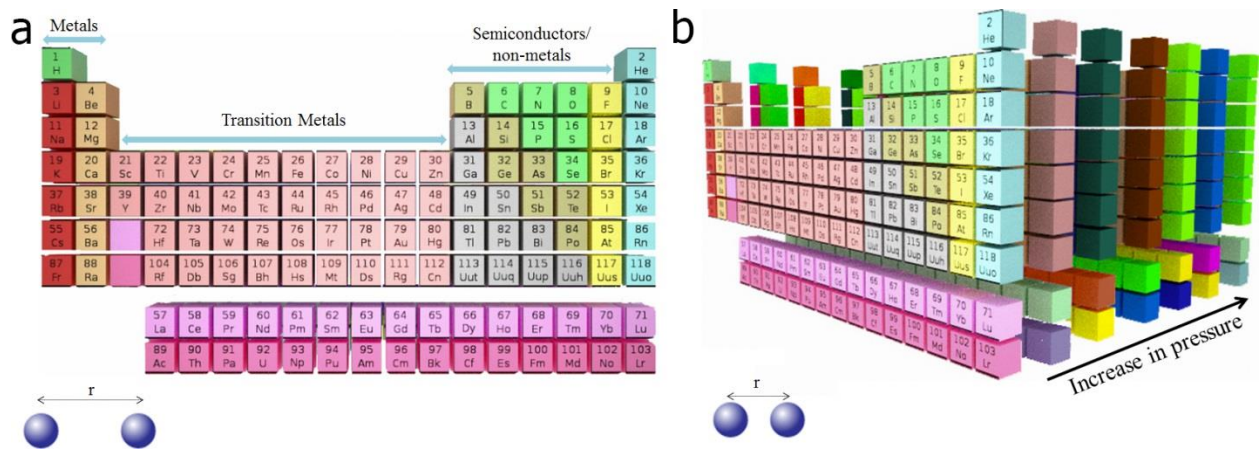


Figure 7. Material properties at ambient pressure differ in comparison to high pressure. (a) Periodic table of elements separated by their ambient pressure properties. **(b)** The elemental material properties change with increase in hydrostatic pressure. The inset shows the atomic radii between two atoms being more confined.

Due to these advances in high-pressure research, DAC is the most powerful ultra-high-pressure device, helping physicists and chemists discover new electronic and structural states of matter and further understand the basic physics underlying ultra-high-pressure phenomena. This dissertation focuses on hydrostatic pressure effects on h-BN, MoS₂, and WS₂.

Hexagonal Boron Nitride

Since several 2D layered materials promise great potential for the development of future advanced material systems and nano-devices.¹⁻⁶ h-BN in particular has stimulated extensive interest both theoretically⁷⁻¹¹ and experimentally.^{3, 12, 13} This insulating, wide-band-gap (~ 6 eV) material is sometimes referred to as “white graphene” due to its white appearance in powder form and its hexagonal lattice structure (**Figure 8**). In particular, h-BN has been recently investigated for its dielectric properties,¹⁴ integration with graphene,¹⁵ ultra-violet (UV) lasing,¹⁶ and high thermal conductivity for heat management applications.⁴

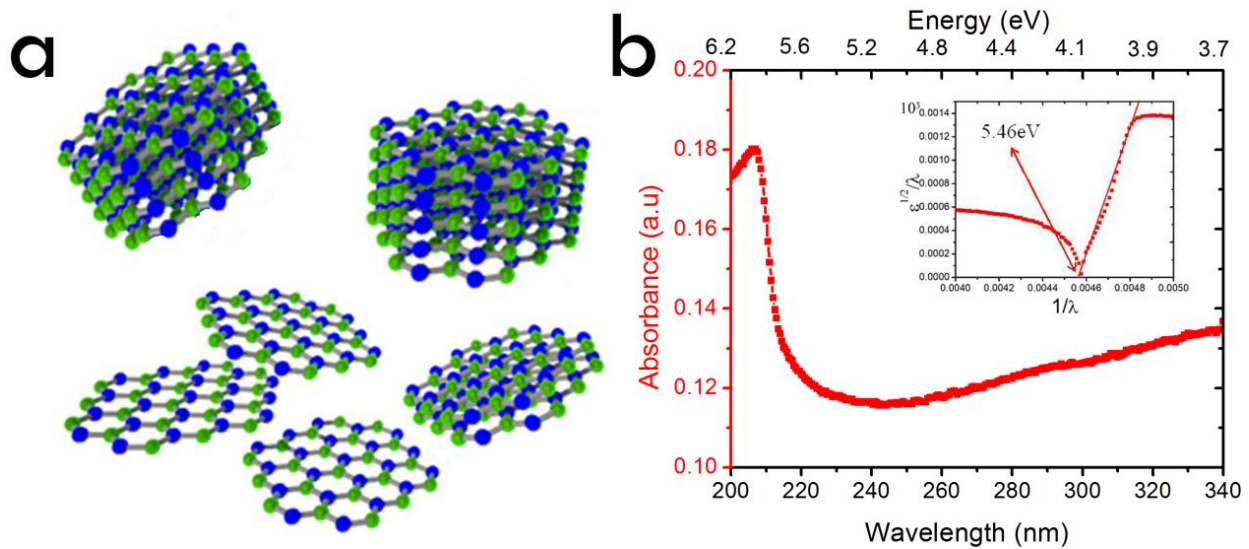


Figure 8. Optical properties of h-BN. (a) Crystal structure of h-BN where boron (green) is connected to nitrogen (blue) in a hexagonal lattice structure. (b) Deep UV absorption from h-BN. Inset: Tuac's plot showing the E_g of pristine h-BN to be 5.5 eV.

This dissertation reports new findings in partially oxidized h-BN (PO-hBN) that reveal noticeable differences between pristine, white, electrically insulating h-BN platelets and acoustically irradiated dark, electrically conductive h-BN platelets. We focus on the analytical characterization of the material properties before and after the acoustic irradiation. The wide

range of acoustic power leading to measurable changes in optical properties indicates that solution-dispersed h-BN can be used for detecting high power acoustic events such as blasts and vibrational shocks. Based on the analytical differences between pristine and irradiated h-BN we suggest that the material inversion originates from the partial surface or edge oxidation of the initial h-BN platelets during the irradiation process. Albeit demanding continued research studies, this work presents a facile route for preparing modified h-BN nanomaterials with tunable properties for a variety of suitable applications including enhanced passive chemical sensing and blast/shock dosimeters or detectors.

A variety of approaches have been explored to customize h-BN by engineering their band-structures,³¹ functionalizing their edges,³² doping,³³ or chemically altering the material.³⁴ These methods include mechanical exfoliation,³⁵ chemical vapor deposition (CVD) growth,^{16,17} and solvent induced exfoliation.³⁶ Mechanical exfoliation is primarily used to study single or multiple layers, but does not allow for large areas to be fabricated. In comparison, CVD allows for large area growth of graphene,^{9,17} h-BN,¹⁶ and even hybrids such as h-BNC,³¹ this growth technique however is generally understood to be limited to certain substrates such as nickel or copper and requires high temperature. To chemically exfoliate h-BN, traditionally, N,N'-dimethylformamide (DMF)³⁷ and other reactive agents³⁸ have been used as a solvent. Recently, it was found that just water can be used to exfoliate h-BN^{39,40} down to a few layers and is considered to be a “clean” exfoliation solvent since the h-BN material is free of surfactants or organic functionalization from foreign materials.

Molybdenum Disulfide

Monolayer TMDs are direct band-gap semiconductors which have tunable band structures by strain, functionalization, or applying external fields. The properties and structure of 2D materials implore further research. The recent advances in the preparation of atomically thin layers of van der Waals (vdW) bonded crystalline solids by mechanical exfoliation or chemical synthesis have allowed for renewed investigations of 2D materials beyond graphene but with a similar layered hexagonal structure⁴¹⁻⁴⁵. Within this class of 2D materials are TMDs, such as MoS₂, have been increasingly explored to access a wealth of phenomena including opto-electronics⁴⁵, valleytronics⁴⁶, spintronics⁴⁷ and coupled electro-mechanics⁴⁸. All of these phenomena arise from the complex thickness-dependent physical and electronic structures of the multilayered materials, in which the coupled electro-mechanics can be regarded as straintronics. As a case study, we can consider an atomically thin layer of MoS₂ which deviate from their bulk counterpart because it exhibits a direct band gap at the K point (**Figure 9a**). Due to the direct band gap in monolayer MoS₂, better photo-response is observed compared to the graphene-based systems. Multilayered MoS₂, having a band gap (E_g) of approximately 1.2eV,⁴⁹ is composed of stacked tri-atomic sheets where each tri-atomic monolayer exhibits a sandwiched structure with a plane of transition metal molybdenum atoms covalently bonded to, and sandwiched between, two planes of chalcogen sulfur atoms (**Figure 9b**). Unlike monoatomic multilayered graphene with sp^2 hybridization, the diatomic composition of multilayered MoS₂ coupled with its d-orbital electronic states⁵⁰ and the small 6.5Å vdW interlayer gap raises the prospects of strong sulfur-sulfur interlayer interactions under axial compression that might lead to an electronic phase transition.

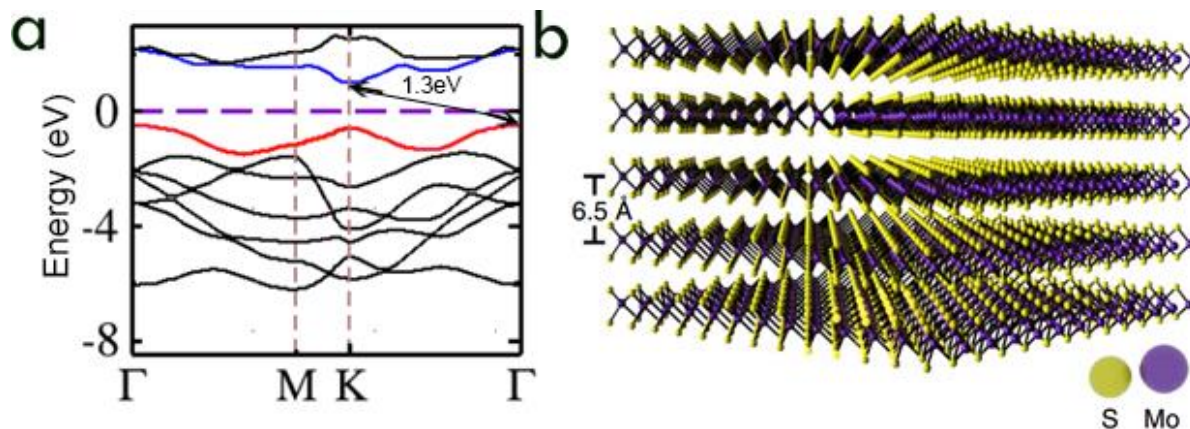


Figure 9. Properties of multilayered MoS₂. (a) Electronic band structure of MoS₂ shows the indirect band gap of 1.3eV. The lowest conduction band and the highest valence band is shown in blue and red respectively. (b) A cartoon rendition of multilayered MoS₂.

Previously, several approaches have been undertaken to alter the solid-state properties of MoS₂, including chemical doping,^{19,43,51,52} intercalation,^{53,54} surface functionalization,⁵⁵ and defect engineering.^{52,56,57} Furthermore, previous theoretical studies have suggested that an isostructural S-M transition in multilayered MoS₂ can be induced by pressure or strain.^{21,58,59} Despite the broad interest in this phenomenon in layered nanomaterials, however, previous experimental results only reported a limited reduction in the electrical resistance^{29,57,60,61} with no clear evidence for the pressure-induced S-M transition.

To advance our knowledge in understanding the properties of 2D materials in extreme environments, we have investigated high-purity exfoliated single crystalline MoS₂ with a stoichiometric chemical composition to evaluate the structural, vibrational, electrical and optical dependence at pressures up to 35 GPa. These results show a lattice distortion involving anisotropic *c/a* axial compression beginning at approximately 10 GPa in multilayered MoS₂ leading to an intermediate state (IS) followed by a pressure-induced S-M transition at approximately 19 GPa. First-principles theoretical calculations, which are performed to shed light on the underlying physics responsible for the S-M transition, attribute the origin of the

metallic electronic states to sulfur-sulfur interactions as the vdW gap closes at high pressures. Our combined experimental and theoretical results here open a new window of opportunity for the development of nanoscale pressure switches, sensors, and multi-physics devices with coupled electrical, vibrational, optical and structural properties using multi-layered MoS₂ and semiconducting TMDs.

Tungsten Disulfide

Due to the pronounced two-dimensional (2D) character of the transition-metal dichalcogenides (TMDs), interest in both the electronic and structural aspects of these materials have been garnered. These classes of TMDs are materials that possess a variety of electronic ground states, such as superconductivity,⁶² lattice deformation,⁶³ Mott transition,⁶⁴ and Anderson localization.⁶⁵ Of these TMD materials, tungsten disulfide (WS₂) has attracted significant interest due to its unique structural,²⁰ optical,^{66,67} thermal⁶⁸ and electronic⁶⁹ properties. Unlike monolayer graphene which has sp² hybridization, multilayered semiconducting multilayered WS₂ has an indirect bandgap E_g of ~1.3eV. Similar to other TMDs, WS₂ is a layered TMD in the hexagonal crystal structure, in which tungsten has a trigonal prismatic coordination to sulfur and that strong in-plane covalent bonds exist between the transition metal (W) and two chalcogen (S) atoms while weak out-of-plane van der Waals forces (vdW) exists interstitially between layers. Since the out of plane atoms along the c-axis is interacting via weak vdW forces, shearing and compression is easier along this axis in comparison to the covalently bonded in-plane a-axis. This has therefore allowed for researchers to investigate this material by means of mechanical exfoliation. Applying hydrostatic pressure allows for control over the vdW interlayer spacing and therefore allows for the modulation of electronic properties.

Chapter 2. Effects of pressure on 2D materials¹

Partially Oxidized Hexagonal Boron Nitride

Introduction

By acoustically irradiating pristine, white, electrically insulating h-BN in aqueous environment we were able to invert its material properties. The resulting dark, electrically conductive h-BN (referred to as partially oxidized h-BN or PO-hBN) shows a significant decrease in optical transmission (> 60%) and band-gap (from 5.46eV to 3.97eV). Besides employing a wide variety of analytical techniques (optical and electrical measurements, Raman spectroscopy, SEM imaging, EDS, X-Ray diffraction, XPS and TOF-SIMS) to study the material properties of pristine and irradiated h-BN, our investigation suggests the basic mechanism leading to the dramatic optical and electronic changes following the acoustic treatment. We find that the degree of inversion arises from the degree of h-BN surface or edge oxidation which heavily depends on the acoustic energy density provided to the pristine h-BN platelets during the solution based process. This provides a facile avenue for the realization of materials with tuned physical and chemical properties that depart from the intrinsic behavior of pristine h-BN.

Color change and optical properties

Acoustic irradiation involves the formation and growth of micro-bubbles driven by acoustic energy in the liquid used as a medium for acoustic wave propagation.¹⁷⁻¹⁹ The implosion of such micro-bubbles can lead to the generation of very high local temperature (>5000K) and pressure

¹ Nature communications | 5:3731 | DOI: 10.1038/ncomms4731. A.P.N. initiated this collaborative research project. J.Z., J.L., X.W. and J.-F.L. designed the experiment. A.P.N, D.A, J.Z., J.L. and X.W developed the measurement setup and performed the measurements. D.A., S.B., T.P. and A.K.S. conducted the theoretical modelling and correlation with experimental data. D.A. led the writing of the paper. All the authors participated in the discussion of the results and the whole project was supervised by A.K.S., D.A. and J.-F.L.

(>1GPa) conditions in very short periods of time ($\sim 2\mu\text{sec}$).¹⁷ This can, in some cases, alter the molecular structure and composition of the solid matter dispersed in liquid.^{17, 19} We subject crystalline h-BN platelets to an hour of acoustic irradiation in aqueous environment which generates h-BN platelets of thinner lateral sizes and thicknesses of platelets ranging from 5nm to 8nm. A schematic of this irradiation process is illustrated in **Figure 10a**. After the acoustic treatment a change in the appearance of the platelet powder from white to dark (**Figure 10b, inset**) and a $\sim 60\%$ decrease in transmission (**Figure 10b**) are observed. We find the transmission is heavily dependent on the ultrasonication time or acoustic energy density (**Figure 10c**). The rate of change in transmission is significantly higher ($0.35 \Delta T/\text{KJcm}^{-2}$) within the first fifteen minutes in comparison to the next 45 minutes of acoustic irradiation ($0.08 \Delta T/\text{KJcm}^{-2}$), which we attribute to a higher initial oxidation rate. This dependence can be useful for a range of applications including passive acoustic sensors and blast dosimeters. For instance, close-proximity blast injuries are believed to be the result from exposure to over pressurization wave generated by the blast itself.²⁰ If the blast pressure is severe enough, fluid-filled cavities such as the brain are especially susceptible to injury. Currently, photonic-nanocrystal based blast sensors exhibit complete color loss and defragmentation when exposed to 320kW/m^2 .²¹ We find that PO-hBN platelets gradually change color up to an exposure of 830kW/m^2 . This gradual color change with larger applied power density could afford for a wider range of detection for higher intensity blasts. This dependence on irradiation energy and the change in appearance suggests that solution-dispersed h-BN or an h-BN microfluidic device might be suitable as a blast dosimeter or detector.

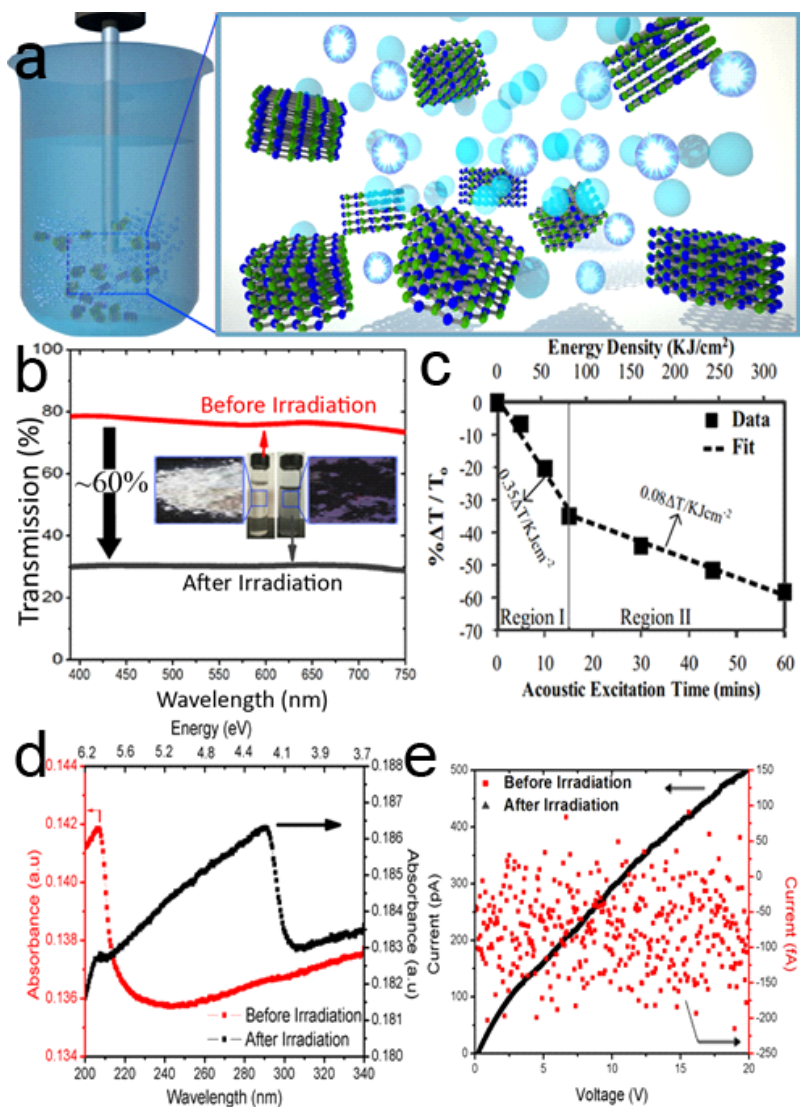


Figure 10. (a) An illustration of the growth and implosion of acoustically formed bubbles which lead to the inversion of the optical and electrical properties of h-BN flakes. (b) A large decrease in transmission is observed after 60 minutes of acoustic irradiation. The inset shows the optical images of h-BN, before and after irradiation. (c) The normalized change in the h-BN optical transmission at 500nm wavelength reveal two regions of linear dependence. To is the pristine h-BN optical transmission. (d) The ultraviolet-visible (uv-vis) absorbance spectra of pristine h-BN (red) and after 60 minutes of acoustic irradiation (black). A decrease from 5.46eV to 3.97eV (27% decrease) in the optical band-gap is observed. (e) Upon irradiation the h-BN platelets undergo a transition from an insulating to a conductive phase.

Recent theoretical and experimental studies have shown that intercalating and chemically modifying h-BN can lead to changes in appearance and conductance.^{7, 9, 22, 23} Based on the optically induced band-transition, the optical energy gap can be investigated. **Figure 10d** shows

the uv-visible absorption spectrum for pristine and irradiated h-BN. We observe a substantial (~27%) decrease (from 5.46eV to 3.97eV) in the optical band-gap after irradiation due to hydroxyl (OH) ions attaching onto the irradiated h-BN platelets.²³ The optical band-gap energy was determined using Tauc's plot. The finite conductance of PO-hBN is shown in **Figure 10e** and reflects a transition from an insulating to a conducting phase. The presence of OH ions, and the formation of β -B₂O₃ during the high temperature and pressure cavitation conditions has been previously studied.^{23, 24}

Hydrophobicity of PO-h-BN

We associate the conductance of PO-hBN to the OH ions attaching onto the irradiated h-BN platelets. Although h-BN is considered an insulating material (E_g of 6eV), altering the conductance of h-BN allows for the material to behave as a near-visible large band-gap semiconductor (E_g of 3.97eV). In addition, pristine h-BN platelets are known to be hydrophobic before irradiation.²⁵

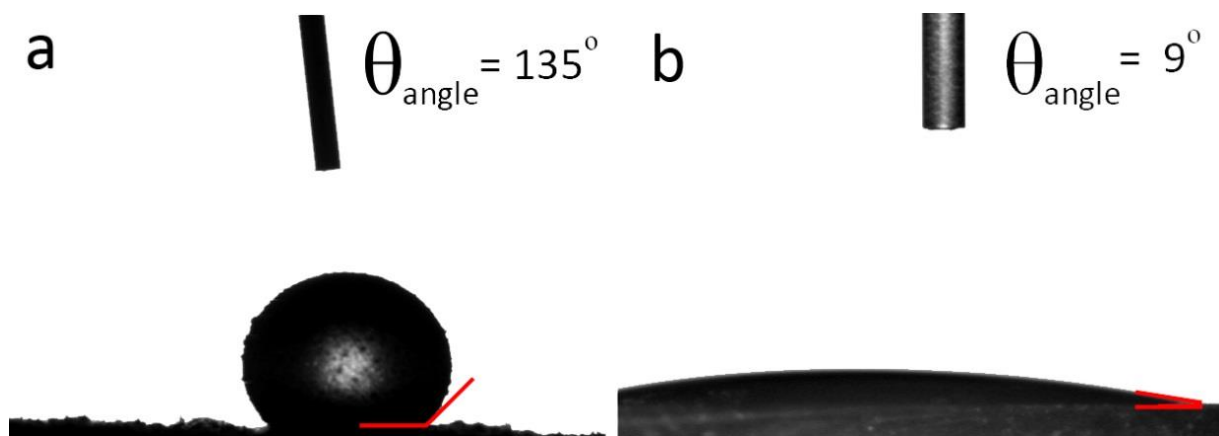


Figure 11. (a) Pristine h-BN platelets are observed to have a contact angle of 135° while the (b) contact angle for PO-hBN is 9° . This reduction of hydrophobicity is attributed to hydroxyl ions on the surface of the irradiated h-BN. This suggests that OH ions would likely promote the hydrophilicity to h-BN after irradiation.

We find that the PO-hBN platelets are hydrophilic (contact angle of 9°) (**Figure 11**). This is additional evidence of the OH ions attaching onto the h-BN platelets. Previous studies reported in the literature have also observed this hydrophilicity after altering h-BN with OH groups.²⁶ To understand how h-BN converts to PO-hBN, we investigated its physical and chemical structure before and after acoustic irradiation. Recent literature has reported that OH ions and H₂O₂ are formed in water while under high intensity acoustic irradiation.^{18, 26} We suggest that the H₂O₂ initiates the thinning of the h-BN platelets while the OH ions attach onto the edges and surface of the PO-hBN platelets. To examine if OH ions are attached to the surface, we employ Fourier transform infrared (FTIR) spectroscopy to observe the O-H vibration mode at 3435 cm^{-1} . To find the difference in percentage composition of oxygen and to determine the elemental bonding to the oxygen species, we employed x-ray photoelectron spectroscopy (XPS).

Characterization of PO-h-BN

As shown in **Figure 12a**, we find that the surface coverage with oxygen species increases from 2% to 41% (based on the O1s peaks) signifying a substantial increase upon acoustic irradiation.

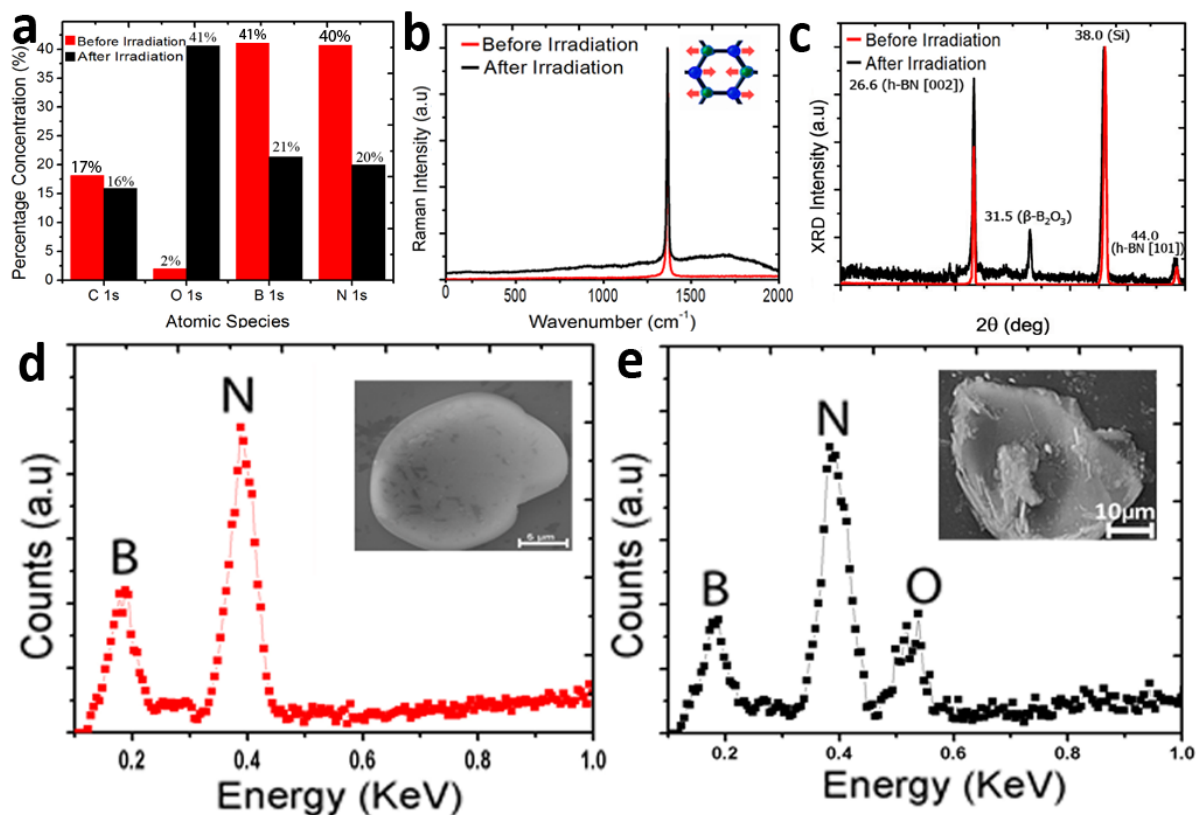


Figure 12. (a) XPS elemental percentage concentration of various atomic species. The oxygen surface concentration increases from 2% to 41% after irradiation. (b) The Raman peak at 1367cm⁻¹ is observed before and after acoustic irradiation indicating that the crystallinity remains hexagonal. The inset depicts the E_{2g} phonon mode responsible for the Raman peak. (c) XRD shows the β-B₂O₃ peak for the irradiated h-BN which likely arises from the oxidation of h-BN during the high temperature/pressure cavitation conditions. SEM image and SEM-EDS spectra of (d) individual pristine h-BN platelet and (e) PO-hBN platelet after acoustic irradiation. The energy peaks for N (at 0.2KeV) and B (at 0.4KeV) are observed both before and after h-BN irradiation, but O (at 0.55KeV) is detected only in PO-hBN.

As suggested by the BN phase diagram,²⁷ synthesis at different pressures and temperatures can lead to w-BN (wurtzite boron nitride), c-BN (cubic boron nitride), r-BN (rhombohedral boron

nitride) or h-BN. To elucidate any changes to the crystal structure, we examine the pristine and irradiated platelets using Raman and XRD spectroscopy (**Figure 12b** and **12c** respectively). We find that the intrinsic h-BN E_{2g} vibrational mode (at 1367cm^{-1}) did not change after irradiation (**Figure 12b**). The XRD however, indicates the presence of $\beta\text{-B}_2\text{O}_3$ (boron trioxide)²⁸ crystalline phase in the PO-hBN (**Figure 12c**), which is not surprising since sintering boron nitride in water leads to the formation of B_2O_3 and NH_3 .^{24, 29, 30} In order to confirm the presence of ammonia, we use Nessler's reagent (a $\text{K}_2\text{HgI}_4/\text{KOH}$ solution) and observe a yellow coloration which is an indicator of the presence of NH_3 .²⁶ It has been reported by Shen *et al.*²² that intercalation of h-BN by SO_3F not only alters the color (from white to deep blue) of the material, but also changes the electrical conductivity (from $1.5\text{ S}\cdot\text{cm}^{-1}$ to $1.1\times 10^5\text{ S}\cdot\text{cm}^{-1}$). We attribute the change in color observed in our results to the partial oxidization of h-BN caused by the acoustic energy density provided to the solution. In evidence of this EDS was employed to detect the presence of oxygen in the irradiated h-BN (**Figure 12e**).

EDS-mapping of oxygen, boron, and nitrogen species were done on both pristine and irradiated samples showing that oxygen species is prevalent after irradiation (**Figure 13**). In order to locate and identify qualitatively and quantitatively the species of interest (OH, BO) on both pristine and irradiated h-BN platelets, we employ TOF-SIMS, a highly surface-sensitive (sensitivity in the parts-per-billion range) analytical technique.³¹ TOF-SIMS is employed with the purpose of (i) detecting changes in chemical composition, and (ii) relative quantification of species of interest between the pristine h-BN and PO-hBN.

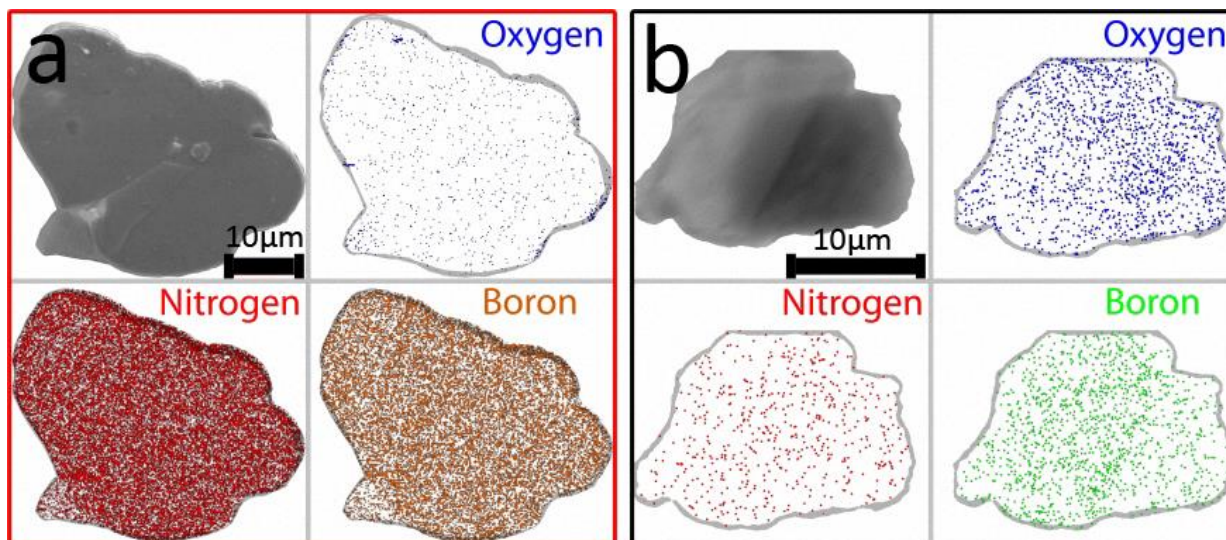


Figure 13. SEM EDS mapping of oxygen, nitrogen, and boron in (a) pristine h-BN and (b) PO-hBN after 60 minutes of irradiation. The presence of oxygen species is evident in the EDS mapping of POh-BN.

We first focus on identifying the chemical changes that occur at the very surface of the irradiated h-BN. For PO-hBN (**Figure 14a**) a consistent increase in the OH amount,

$$\frac{[(\sum_m I_{OH})/(\sum_m I_B)]_{\text{irradiated}}}{[(\sum_m I_{OH})/(\sum_m I_B)]_{\text{pristine}}} \cong 4, \text{ where } I_M \text{ defines the secondary ion (SI) intensity of the detected}$$

species M while $\sum_m I_M$ indicates the total SI count of species M spanning a mass range m (i.e., the total count of the SI peak), was observed together with an even larger increase in BO amount,

$$\frac{[(\sum_m I_{BO})/(\sum_m I_B)]_{\text{irradiated}}}{[(\sum_m I_{BO})/(\sum_m I_B)]_{\text{pristine}}} \cong 10. \text{ These ratios (normalized to boron to account for surface area and}$$

matrix changes) imply that the surface of the h-BN platelets is oxidizing upon ultrasound irradiation in aqueous solution. To further localize the extent of the surface oxidation we make use of the TOF-SIMS' BA mode (high spatial resolution, ~ 200 nm). **Figure 14b** and **14c** present the actual surface distribution of B, BO and OH. While the high resolution map of the pristine h-BN shows the OH and BO species located mostly at the platelets' boundaries, the map of the PO-hBN indicates that the OH and BO species are essentially covering most of the platelets'

surfaces. Associated with the high concentration increase in OH and BO species upon irradiation, the reduction of the platelets size implies that during the acoustic irradiation process the h-BN platelets experience simultaneous fragmentation and oxidation. Furthermore, due to the B₂O₃ signal present in the PO-hBN TOF-SIMS spectra, combined with XRD measurements shown in **Figure 12c**, we summarize that the detected BO signal is, in fact, a marker for the parent B₂O₃ molecule.

Figure 14a, b and c, are taken in Static SIMS mode where only a few of the outermost layers are probed. It is of interest, however, to know the chemical differences as function of surface depth by looking at the species of interest (OH and BO) as function of sputtering time (i.e. depth profiling). First, the OH and BO depth profiles for the irradiated sample should indicate both the mechanism and penetration depth of oxidation in the PO-hBN flakes. Second, the ratio between the depth profile of OH (or BO) species for the irradiated sample and the corresponding depth profile of OH (or BO) species for the pristine sample should indicate the relative increase in OH (or BO) amount as function of depth as a result of the acoustic treatment.

In **Figure 14d** we present the Dynamic SIMS depth profiles of boron, $\sum_m I_B(t)$, where t is the Bi₁⁺ sputtering time, normalized to their region of interest areas, for both pristine and irradiated samples. These depth profiles are used as reference curves for the other species of interest to account for surface area and matrix changes, as shown in **Figure 14e** and **14f** where the OH and BO depth profiles, respectively, are normalized to their corresponding B depth profile (black and red curves). First, we observe that the actual BO signal (referenced to boron) reaches saturation after 40 to 50 minutes of sputtering (**Figure 14f**, black curve) while the corresponding OH signal

(**Figure 14e**, black curve) starts decaying almost immediately from the surface. This suggests the OH radicals penetrate the surface during the irradiation process and start generating B_2O_3 at a rate that depends on depth. We think that as the pressure exerted between atomic layers is increasing with depth the OH radicals convert more into β - B_2O_3 packing thus the inverse proportionality between the OH and BO depth profiles (black curves in **Figure 10e** and **Figure 10f**, respectively).

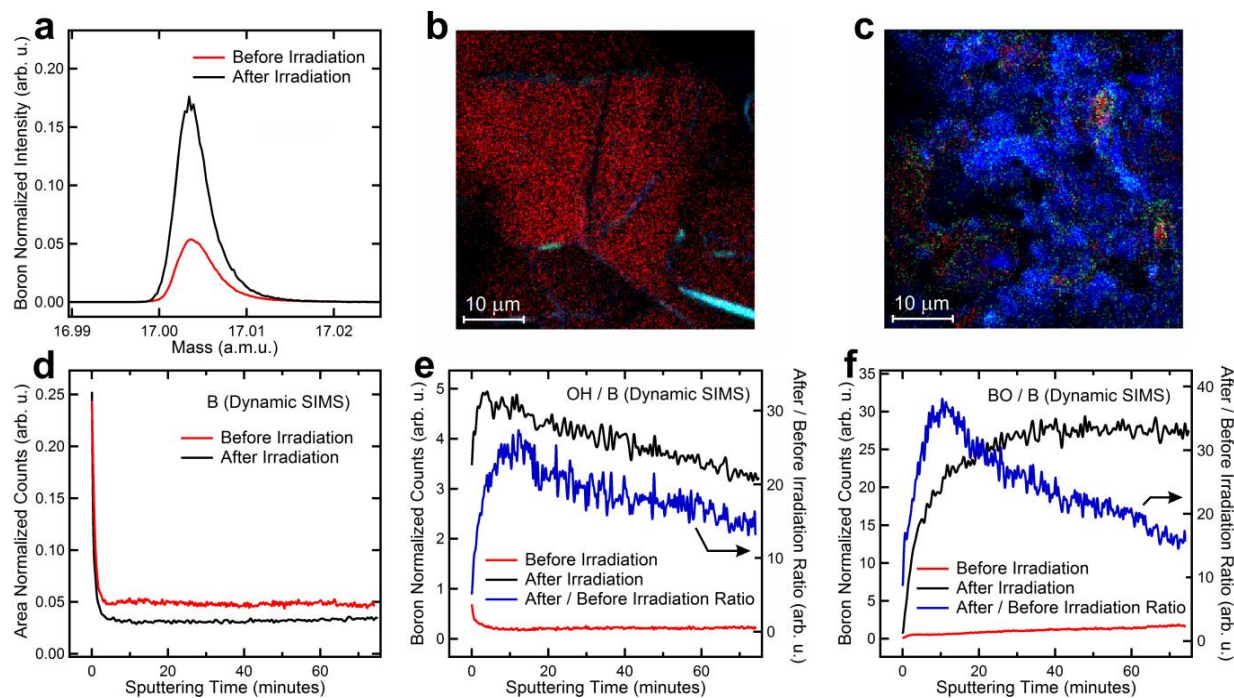


Figure 14. (a) Comparison of the OH signal normalized to the total boron count for pristine and irradiated h-BN samples. (b) Overlay of B (red), BO (green) and OH (blue) signals for the pristine and (c) irradiated h-BN sample. The irradiated h-BN platelets reveal coverage by OH species. (d) Dynamic SIMS depth profiles of the boron signal normalized to its coverage area for the pristine (red curve) and irradiated (black curve) h-BN. A steady state is reached after 5 – 10 minutes of sputtering. Dynamic SIMS depth profiles of the (e) OH and (f) BO signals normalized to their corresponding B signals for pristine (red curve) and irradiated (black curve) h-BN. The ratios of the irradiated and pristine curves in each plot are shown in blue.

Second, the relative ratios (irradiated vs. pristine) of both OH and BO profiles (blue curves in **Figure 14e** and **14f**, respectively) indicate that the relative amount increase in OH and BO species is a function of depth which reaches a maximum after about 10 minutes of sputtering.

We find that, for both species, the increase factor maximum is about 5 times larger than its value at the very surface, suggesting that the main chemical differences between PO-hBN and pristine h-BN samples are located in the first few nm of the surface. Since the OH and BO relative depth profiles (blue curves in **Figure 14e** and **14f**, respectively) are very similar we consider that these curves are most indicative of the actual chemistry responsible for the dramatic changes in physical properties following the acoustic treatment.

Conclusion

Our investigation demonstrates that the observed properties of PO-hBN material are caused by both the presence of OH ions and boron oxidation of the surface. EDS, XPS and TOF-SIMS coherently show a magnitude increase in the amount of oxygen per detected boron signal.

Although the crystal structure remains virtually the same for both h-BN and PO-hBN flakes, a significant 27% decrease in the optical band-gap and a significant increase in conductance are observed in the acoustically irradiated h-BN flake. Having precise control over the band-gap and altering surface conduction warrants more investigations on PO-hBN. Future systematic studies on enhancing the material properties of h-BN are expected to enable further understanding and material control leading toward advanced tunable nanomaterials and enhanced sensors.

Pressure-Induced Semiconducting to Metallic Transition in Multilayered MoS₂

Introduction

Although, these 2D materials already exhibit unique properties that deviate from their bulk counterparts in ambient conditions, pushing these materials properties to their extreme limits will allow us to further characterize their material properties.

The diamond anvil cell has been used to generate extremely high pressures especially in studying the earth interior. Applying this technique to study 2D materials has seldom been studied. Here, we study the optical and electrical characteristics of 2D materials at pressures up to 50 GPa. MoS₂ is a layered TMD material that has recently raised considerable interest due to its unique semiconducting and opto-electronic properties. Although several theoretical studies^{5,18,21,70} have suggested an electronic phase transition in MoS₂, there has been a lack of experimental evidence for such a transition. Here, we report comprehensive and conclusive combined experimental and theoretical studies on the pressure-dependent electronic, vibrational, optical, and structural properties of multilayered MoS₂ up to 35 GPa. Our experimental results reveal a structural lattice distortion followed by an electronic transition from a semiconducting-to-metallic (S-M) state at approximately 19 GPa, which is confirmed by theoretical *ab-initio* calculations based on first-principles density functional theory. The metallization arises from the overlap of the valance band maxima and the conduction band minima at the Fermi level owing to sulfur-sulfur interactions as the interlayer spacing reduces. The critical pressure for metallization is predicted to scale proportionally with film thickness in the few layer limit. The electronic phase transition allows for the modulation of the opto-electronic gain for the multilayered MoS₂. This pressure-tuned electronic behavior of MoS₂ can open a new window for the development of novel devices with multiple physical phenomena involving the strong coupling of the mechanical, electrical, and optical properties of layered nanomaterials.

We have explored applied pressure effects via a high-pressure diamond anvil cell (DAC), as a controllable and reversible degree of freedom to modulate the properties of multilayered single-crystal MoS₂. The DAC technique coupled with a hydrostatic pressure medium (**Figure 15b**) has been shown to be effective in elucidating the electrical, vibrational, optical and structural

properties of a plethora of materials^{29,60,71,72}. The optically transparent window of the diamond allows us to conduct a series of *in-situ* high-pressure experiments including accurate pressure calibration from ruby fluorescence, electrical transport measurements, and optical Raman and synchrotron x-ray diffraction (XRD) spectroscopy⁷³ leading to the observation of S-M transition in multilayered MoS₂ at high pressures. Pristine multilayered crystalline MoS₂ was transferred onto the DAC using micron-edged tweezers for investigations of the electronic, phononic, and structural behaviors at pressures up to 35 GPa (see **Experimental Procedures and Setup** for details). In addition, first-principle theoretical calculations were performed to elucidate the underlying material physics of the transition.

Electrical Conductivity and Electronic Structures

In-situ electrical conductivity measurements at room temperature using standard four-point metallic contacts reveal a gradual decrease in resistivity (ρ) with pressure up to 10 GPa, which can be understood in the context of a pressure activated carrier transport model in good agreement with the experimental data. Between 10–19 GPa an abrupt decrease of about three orders of magnitude (**Figure 15c**) is observed. Theoretical *ab-initio* band structure calculations of the multilayer MoS₂ corroborates the experimental result with a predicted transition at approximately 20 GPa (**Figure 15c, inset**), which was theoretically found to correspond to a vanishing band gap owing to a S-M electronic transition.

In addition, *in-situ* temperature-dependent resistivity measurements were performed in the DAC in order to determine the resistivity profiles before and after the transition. It is well known from classical solid-state physics that resistivity decreases with temperature for semiconductors owing to thermally activated carriers, in contrast to increasing resistivity for metallic conductors due to

increased electron-phonon scattering⁷⁴. Our resistivity measurements for multilayered MoS₂ reflect the aforementioned classical semiconducting behavior as indicated by the negative temperature coefficient of resistivity at 10 GPa (**Figure 15d, inset**) for the semiconducting state, whereas a positive temperature coefficient of ρ is observed at 34 GPa for the metallic state (**Figure 15d**). Calculations using Boltzmann transport theory (BTT) for the temperature-dependent resistivity at approximately 10 GPa and 35 GPa support these experimental findings.

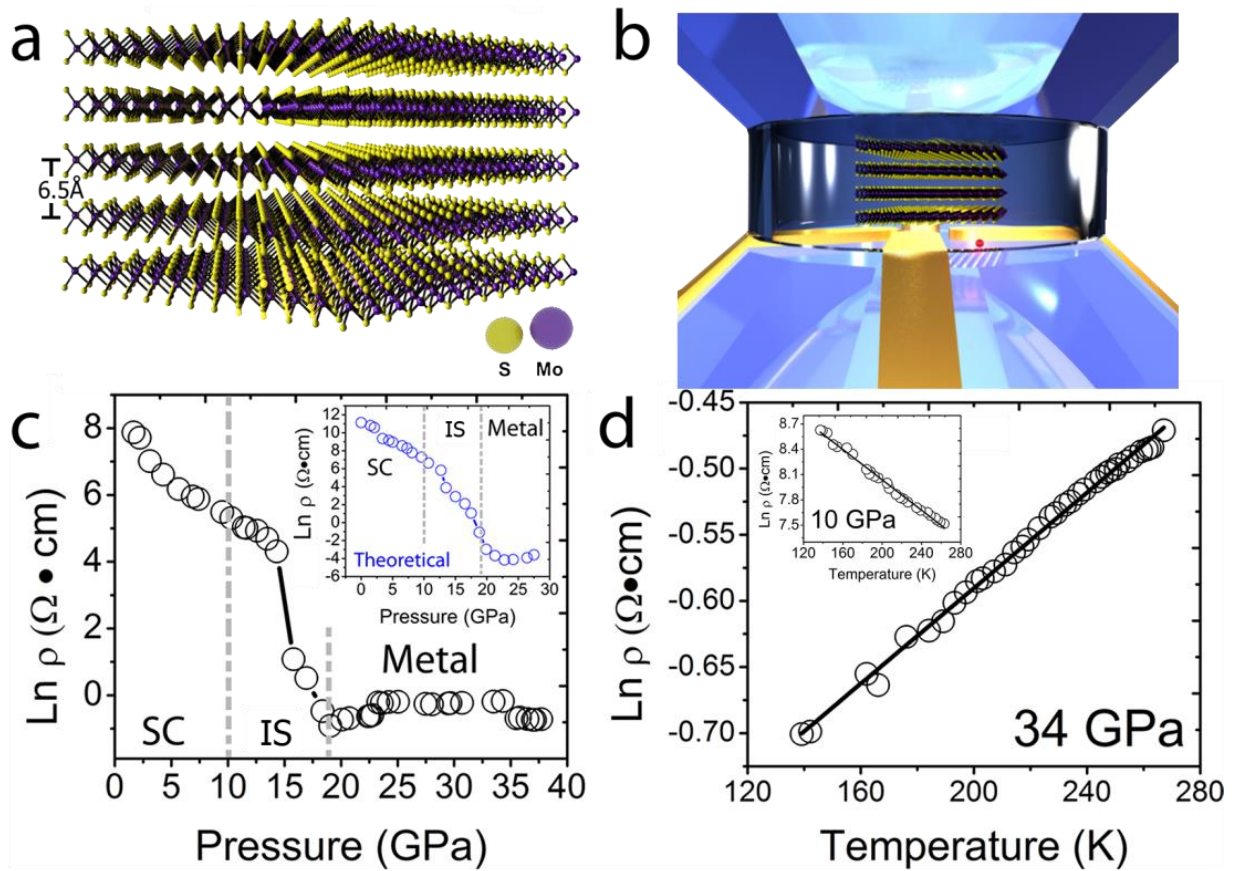


Figure 15. Experimental setup and the electronic properties of multilayered MoS₂ as a function of pressure and temperature. (a) The cross-section illustration of multilayered MoS₂ with an interlayer (*c*-axis) spacing of approximately 6.5 Å. (b) A 3D illustration of multilayered MoS₂ in a DAC pressure medium for compression experiments. (c) Pressure-dependent electrical resistivity of MoS₂. Three characteristic regions have been identified: semiconducting (SC), intermediate state (IS), and metallic regions. Inset: theoretically calculated pressure-dependent electrical resistivity. (d) Temperature-dependent resistivity of MoS₂ in the metallic state. Inset: The experimental temperature-dependent semiconducting behavior of MoS₂. The solid lines serve as visual guides.

Furthermore, theoretical calculations determine that the semiconducting nature of MoS₂ originates from the fact that within a layer, Mo and S atoms are bound by mixed ionic and covalent bonding⁷⁵. Under the application of pressure, the interlayer distance between the atomic planes decreases and the intra- as well as inter-layer interactions are expected to alter the electronic properties of MoS₂. Along the [0001] direction, MoS₂ with anisotropic linear incompressibilities, will experience maximum compression, *i.e.*, the interlayer distance (*c* axis) decreases more significantly than the intra-layer distance (*a* axis). The hydrostatic pressure causes in- and out of plane strain. In order to analyze the effect of in-plane strain in achieving the S-M transition, we calculate the charge density redistribution keeping the in-plane strain constant, while varying the out-of-plane strain. **Figure 16a** and **Figure 16d** show the charge redistribution for a constant out-of-plane strain (6.9%) but at a different in-plane strain of 2.2 and 5.2%, respectively. **Figure 16b** and **Figure 16c** show the same but at a higher out-of-plane strain (11%). It can be seen that the interlayer interaction is enhanced with the increasing in-plane strain. Although, the S-M transition is caused by interlayer interaction due to the normal or out-of-plane strain, however, the in-plane strain helps to achieve this transition at a lower pressure.

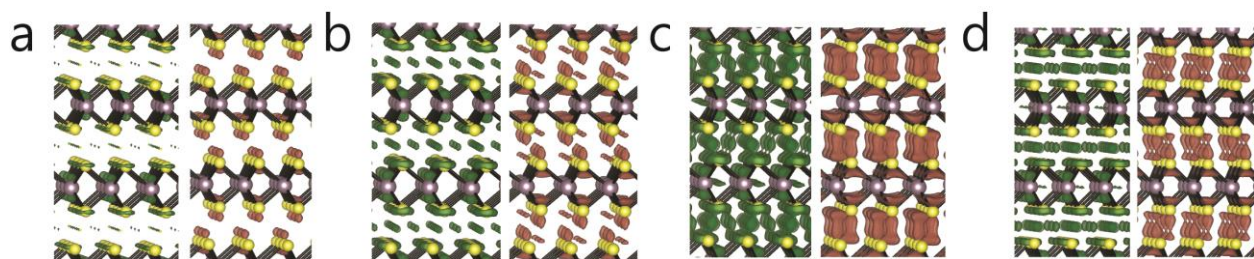


Figure 16. Theoretical charge density isosurfaces of multilayered MoS₂ at different in-plane and out-of-plane strain. Charge accumulation (green) and depletion (orange) at the (a) in-plane and out-of-plane strains of 2.2 and 6.9% respectively, (b) in-plane and out-of-plane strains of 2.2 and 11% respectively, and (c) in-plane and out-of-plane strains of 5.2 and 11% respectively. (d) Same in-plane strain as in (c) but with 6.9 % out-of-plane strain.

With increasing pressure, our theoretical calculations show that the electronic charge moves away from the S atoms and accumulates onto the Mo atoms. Near the critical transition pressure, the maximum charge redistribution is predicted to occur in between the MoS₂ layers across the vdW gap, indicating enhanced S-S interaction. The change in the interlayer interaction from a weak vdW to a stronger interaction near the critical pressure is also supported by the derived lattice parameters using XRD spectra.

Optical Raman Vibrational Spectroscopy

Raman spectroscopy is considered to be a very accurate tool for gaining insight on the lattice vibrations of crystalline materials and has been commonly used to characterize the two prominent vibrational modes (E_{2g} and A_{1g}) that are accessible in MoS₂⁷⁶⁻⁷⁸. In order to elucidate the S-M electronic transition, Raman measurements were conducted *in-situ* to probe vibrational changes in the multilayered MoS₂ under high pressure. It is well known that inducing pressure in MoS₂ results in an increase in the Raman shift (**Figure 17a**) similar to other layered materials^{79,80}. Analyses of the high-pressure Raman spectra reveal that the A_{1g} mode shows three distinct regions (**Figure 17b**): i) significantly increasing Raman shift up to about 10 GPa, ii) nearly invariant shift with pressure between 10 GPa and 19 GPa, and iii) pressure-dependent Raman shift above 19 GPa. An evaluation of the Raman intensity ratio (between the E_{2g} and A_{1g}) also reveals three distinct regions with the maximum intensity ratio observed in the metallic region. We label these regions starting from low to high pressures as the semiconducting (SC), intermediate state (IS), and metallic regions respectively. In light of these observations, the out-of-plane vibrational mode (A_{1g}) can be considered the more prominent Raman mode that is correlated with the semiconducting to metallic transition in MoS₂, in contrast to the in-plane mode (E_{2g} mode) which shows a less distinct character across the transition. The IS can be

understood within the context of phonon softening (PS), which describes the electron and A_{1g} phonon interaction where inter-valence charge transfer between the MoS_2 layers plays an important role in the structural distortion of the crystal symmetry⁸¹. Several materials have been previously reported to exhibit an intermediate state with soften phonon behavior while undergoing a transition from a semiconductor to a metallic state^{82,83} or when stress or strain is applied^{84,85}. In fact, materials that exhibit superconductivity at high transition temperatures (T_c) are often associated with structural distortions that are characterized by phonon softening subsequently resulting in either a structural or electronic phase transition⁸⁶. In our study here, the intermediate state ranges from approximately 10 GPa to 19 GPa where both the Raman shift for the A_{1g} mode (**Figure 17b**) and the spacing between the two modes (**Figure 17c**) show little dependence on pressure suggesting that the lattice structure is distorted. Moreover, the full-width at half-maximum (FWHM) of the two modes initially increases with pressure followed by a subsequent sharp drop around 19 GPa (**Figure 17d**). It should be noted that in a recent report, a drop in the FWHM was also observed during a phase transition in Sb_2Se_3 , a topological insulator which exhibits a metallic state at the surface⁸⁷.

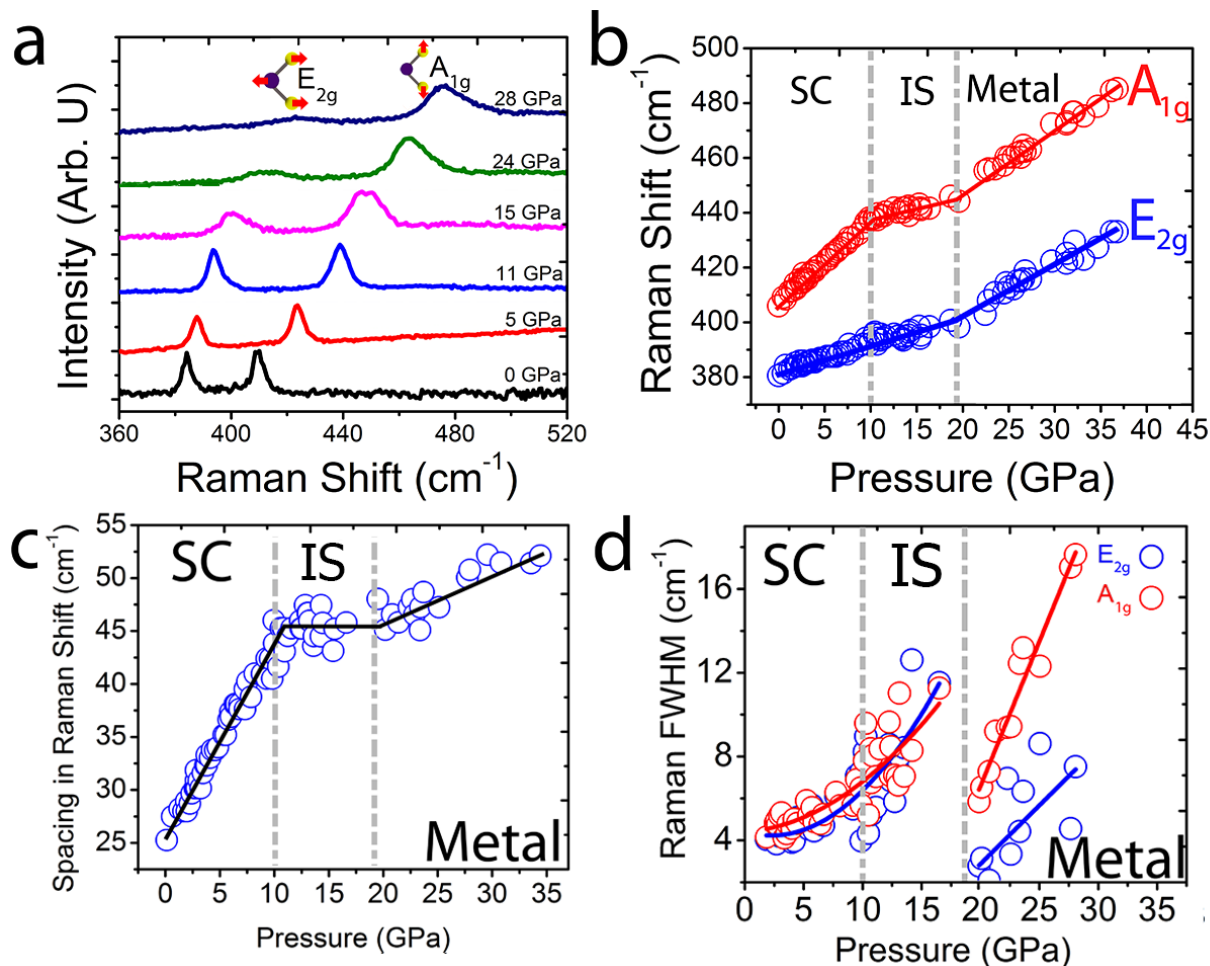


Figure 17. Raman spectroscopic results of MoS₂ at high pressures. (a) Raman spectra at representative pressure points. The inset is an illustration of the in-plane and out-of-plane vibrations of the two key modes E_{2g} and A_{1g}, respectively. (b) The Raman shifts of the two modes with increasing pressures. The solid red and blue lines serve as visual guides. (c) The difference in Raman frequencies between the A_{1g} and E_{2g} modes as a function of pressure flattens out in the IS state and rises at a smaller slope in the metallic region. The solid black line is a visual guide. (d) The FWHM for the A_{1g} and E_{2g} Raman modes across the electronic transition. A sharp drop is observed at approximately 19 GPa where MoS₂ transitions from the IS to a metallic phase. The solid red and blue lines serve as visual guides for the A_{1g} and E_{2g} mode respectively.

Analysis of the A_{1g} and E_{2g} modes as a function of pressure reveal that the splitting in the bands increases with applied pressure resulting in significant changes in the Raman frequencies of the two modes (**Figure 17b**).

Opto-Electronic Properties

Photoconductivity measurements have also been performed as a complementary means for understanding the opto-electronic properties of materials which is dependent on the material's band gap. To provide perspective, the pressure-dependent band gap for multilayered MoS₂ (**Figure 18a**) can be understood from theoretical analysis using the PBE functional under the generalized gradient approximation (GGA). We note that the calculated unstrained E_g of 1.03 eV is approximately 16% less than the experimental value⁸⁸. This underestimation of the bandgap is a well-known problem due to the presence of artificial self-interaction and the absence of the derivative discontinuity in the exchange-correlation potential with the PBE/GGA methods⁸⁹. Hybrid Heyd-Scuseria-Ernzerhof (HSE)⁹⁰ functional and DFT with many-body perturbation theory in the GW approximation⁹¹ are among the few methods to correctly predict the band gap of TMDs; however, these methods are computationally very expensive. Nevertheless, our previous study for bilayer MoS₂ has shown that the overall nature of the variation in the E_g and the band structure with pressure are independent of the functional used²¹ and that the PBE functional gives reasonably accurate results, justifying the use of the PBE/GGA methods for this work. With the increase in pressure, the degeneracy in the bands of the unstrained structure is lifted due to the enhanced interlayer interaction. The split bands in the valence band maxima (VBM) at the Γ point and the conduction band minima (CBM) between the K and Γ point start to move toward the Fermi level. The E_g reduces consequently and becomes metallic when the CBM crosses the Fermi level at a pressure of 23.8 GPa (**Figure 18a**), which correlates well with the transition pressures of approximately 19 GPa in the experimental resistivity measurements and Raman spectra. Analyses of the band structure in the metallic state indicate the overlap of the

conduction and valance bands at the Fermi level (**Figure 18b**). Although we observe a metallization, we do not observe superconductivity (**Figure S8**)

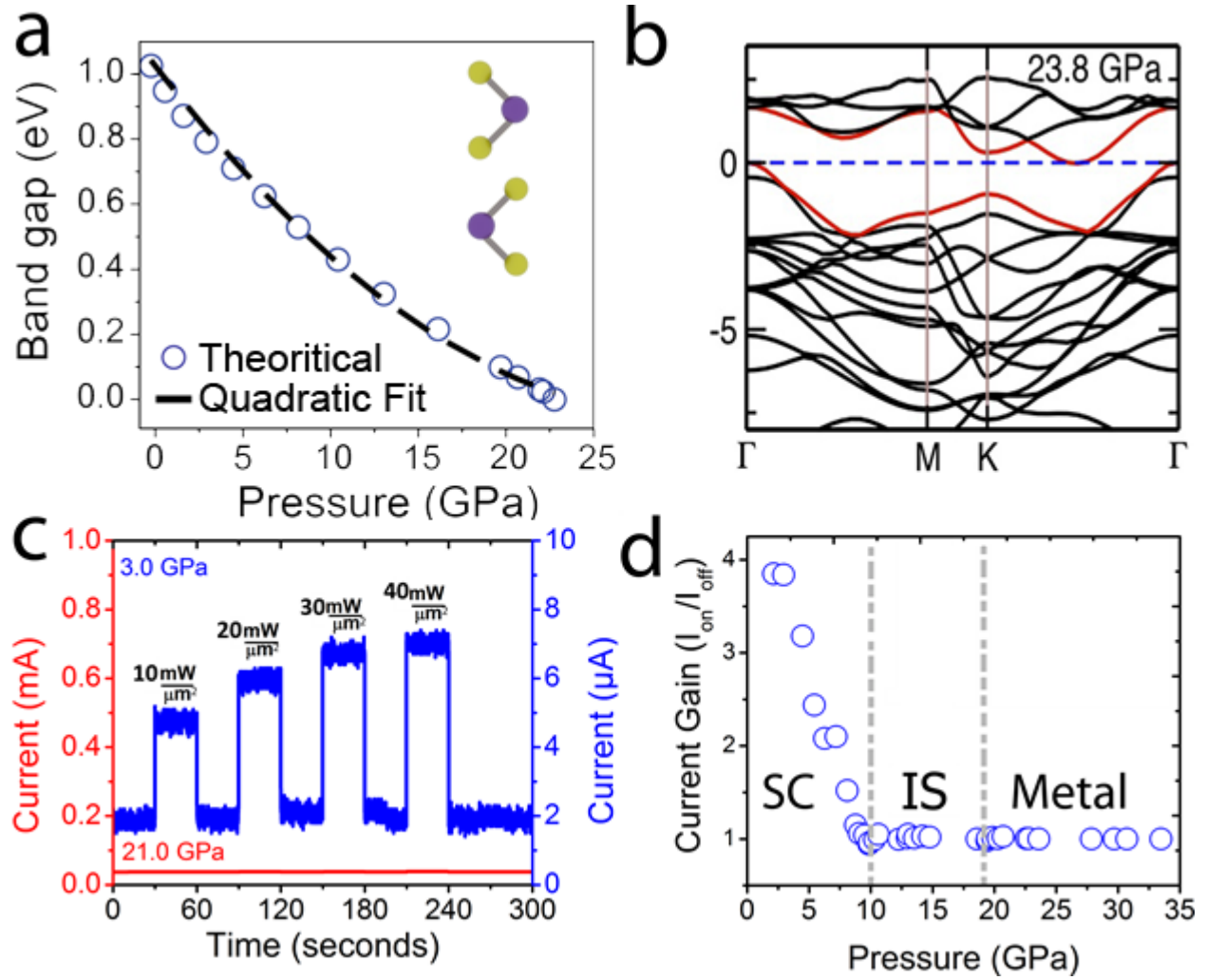


Figure 18. Theoretical electronic structure and experimental pressure-dependent optoelectronic properties of MoS₂. (a) Theoretical calculation of the pressure-dependent band gap of multilayered MoS₂. The bandgap–pressure dependence can be modeled as a quadratic function, $E_g = E_{g0} + aP + bP^2$ was used, where $a = -70$ meV/GPa and $b = 1.13$ meV/GPa². Inset: the unit cell of MoS₂. (b) Theoretical band structure of multilayered MoS₂ under hydrostatic pressure of 23.8 GPa. Valence band maxima and conduction band minima are shown by red lines. (c) Optical switch behavior before (blue lines at 3.0 GPa) and after (red line at 21.0 GPa) the S-M transition with various laser intensities. (d) Current gain (defined as $I_{\text{on}}/I_{\text{off}}$ ratio) as a function of pressure when exposed to a 532 nm (2.3eV) laser light with an intensity of 40 W/m².

Unlike metals, semiconductors show an increase in the electrical conductivity when illuminated by light, and are therefore considered photoconductive. In particular, semiconducting MoS₂ has been found to offer sufficient photo-response that is suitable for practical photoconductive applications^{8,43-45}. Opto-electronics require electron-hole generation/recombination, whereas the opto-electronic response of MoS₂ under green laser illumination (2.3eV) in the event of a semiconducting to metallic transition in MoS₂ is expected to be significantly diminished in the metallic state (**Figure 18c**). As a result, the photocurrent gain (ratio of current under illumination to dark current) was found to decrease with pressure as shown in **Figure 18d**. The current gain decreases at a linear rate ($\Delta I_{\text{gain}}/\Delta \text{GPa} = -7.5\%/\text{GPa}$) until approximately 10 GPa where the current gain saturates to unity, indicating that photoresponse is vanishing as the band gap begins to close.

XRD and HR-TEM Studies

Electronic phase transitions can be accompanied by a structural or iso-structural phase transition. In order to clarify potential structural changes at high pressure, *in-situ* high-pressure synchrotron X-ray diffraction experiments were conducted to probe the perturbation of the crystal structure of multilayered MoS₂ under hydrostatic pressure. Two independent *in-situ* high-pressure angle-dispersive X-ray diffraction (ADXRD) experimental runs were carried out at room temperature using a symmetric diamond anvil cell. For the entire experimental pressure range, all the diffraction peaks can be refined to the hexagonal $P6_3/mmc$ structure using the Rietveld refinement⁹². On the basis of the hexagonal structure model, the crystal lattice parameters for MoS₂ from 0 GPa to 28 GPa were calculated (**Figure 19a**). The structure of the bulk unstrained MoS₂ can be viewed as ABAB stacked single layers of the material⁶¹. Though we did not observe any new peak(s) for multilayered MoS₂ up to 24 GPa in the XRD, a change along the *c*-

axis is observed at approximately 19 GPa, which suggests that the ambient lattice structure of MoS₂ is only weakly distorted. On the other hand, theoretical calculations were performed using the experimental lattice parameters as the reference, which are in close agreement with the GGA values.

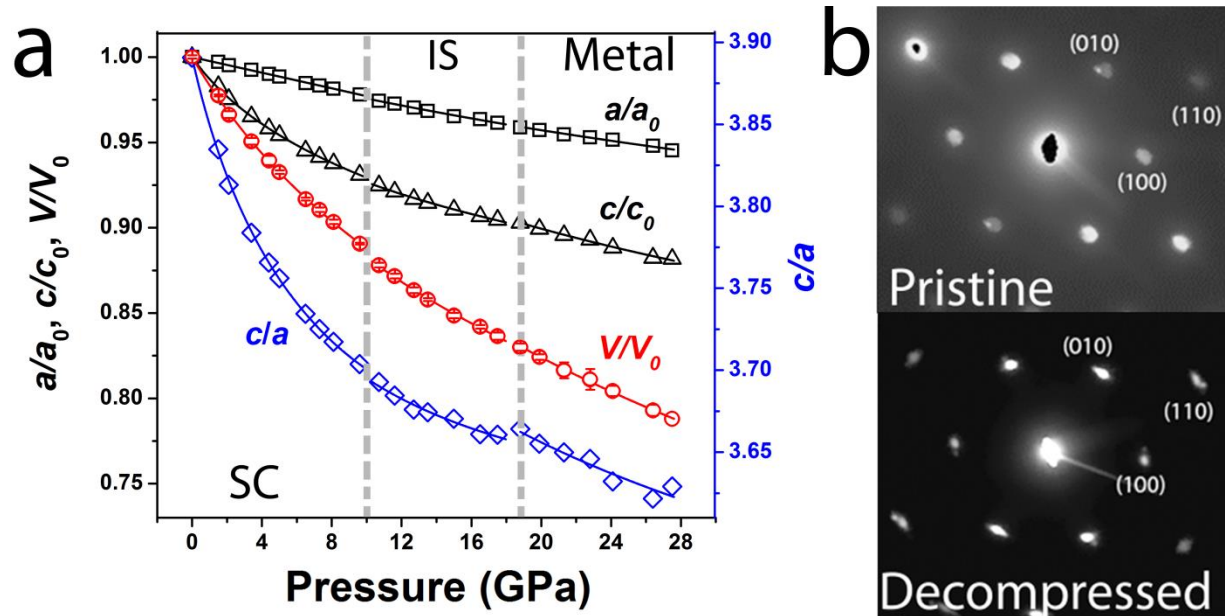


Figure 19. Structural deformation in multilayered MoS₂. (a) Experimental pressure dependence of the lattice parameters of MoS₂. The volume uncertainty bars are within 1% of the data. (b) The experimental SAED patterns of both pristine and decompressed MoS₂. The patterns show that the single crystal structure with the hexagonal symmetry was not significantly affected by high pressures and can be recovered back to its original crystal structure.

Characterizing the atomic structure and quality of MoS₂ is critical for further understanding of the lattice distortion and electronic phase transition under pressure, and for ruling out the effects of lattice defects (*i.e.* point defects, dislocations, grain boundaries, and edges) that could play a role in influencing the experimental results^{52,56,57}. For this purpose, high-resolution transmission electron microscopy (HR-TEM) and electron diffraction techniques were employed to evaluate the crystal structure of the same multilayered MoS₂ before and after the pressure loading experiments. The morphology of the starting sample in HR-TEM shows an atomic MoS₂ lattice

having high crystallinity and the expected hexagonal lattice structure with a lattice spacing of 2.7\AA corresponding to the [100] direction. The cross section HR-TEM analysis shows the layered structure of MoS_2 having an interatomic c -axis spacing of approximately 6.5\AA . Transmission electron microscopy energy-dispersive x-ray spectroscopy (TEM-EDX) analyses were performed on both the pristine and decompressed MoS_2 to determine the stoichiometry which was found to be a 1:2.07 ratio, very close to the ideal 1:2 Mo:S ratio. Scanning electron microscopy (SEM) and scanning electron energy-dispersive x-ray spectroscopy (SEM-EDX) for both pristine and decompressed samples also show negligible difference. The fast Fourier transformation (FFT) of the HR-TEM image shows the reflection spots from (100), (010), and (110), while the selected area electron diffraction (SAED) patterns for both the pristine and decompressed sample indicate the crystallinity and hexagonal symmetry were also unaffected by the applied pressures (**Figure 19b**). The crystallographic results indicate that the starting sample was basically recoverable back to its original crystal structure. Collectively, the HR-TEM, TEM-EDX, FFT, SEM-EDX and SAED results indicate that the sample was of high crystalline quality and purity, and maintained its original chemical composition and lattice structure after the pressure loading experiments.

Discussion

Previous studies have shown that loading of a crystal lattice via strain or hydrostatic pressure can cause a sharp reduction in resistivity, which is a precursor for a S-M transition⁶⁰. In agreement with prior theoretical studies^{18,21,58}, our theoretically-predicted band gap is found to depend inversely on pressure and that the critical pressure for the electronic phase transition is predicted to scale down for multilayered films from approximately 16% normal compressive strain to approximately 11% for bilayer MoS_2 . For monolayer MoS_2 this transition is predicted to occur at

approximately 10% bi-axial strain⁵⁸. Reported studies on other materials such as Sb₂Te₃²⁹, WSe₂⁷¹, BaNi₂As₂⁸⁶, FeS⁹³, V₂O₃⁹⁴, VO₂⁹⁵ and have also shown a drop in resistivity before an electronic or structural phase transition in the material. These results have indicated that applying extremely high pressures onto such materials can even lead to a superconducting state. In MoS₂, this drop in resistivity is correlated with the characteristic phonon modes (E_{2g} and A_{1g}), and concurrent with phonon softening in the intermediate state, which has been observed as a precursor for resistivity transition in other materials^{83-85,96}. We find that both the valence band (VB) and the conduction band (CB) originate from the Mo-d and S-p orbitals with the VB having minor contributions from the Mo-p orbital at zero pressure. With increasing pressure, the contribution from the S-*p_z* and Mo-*d_{z²}* orbitals increases in both VB and CB, indicating a strong interlayer interaction. This analysis is in agreement with the charge redistribution. Experimentally, the bandgap can be extracted from temperature dependent resistivity for intrinsic semiconductors, however, for the case of contemporary MoS₂ materials, the prevailing n-type character prevents bandgap extraction directly from resistivity data.

We note that the A_{1g} mode arises from the out-of-plane vibration of the S atoms with enhanced S-S interactions as the vdW gap closes resulting in the observed metallization. In the intermediate state, vibrational phonon softening phenomenon in the Raman spectra has been studied extensively for other layered materials⁹⁷, suggesting that it can be used as a clear signature for the electronic phase transition in the multilayered MoS₂. The pressure-dependent Raman frequency increase was observed to be higher for the out-of-plane A_{1g} mode than that of the in-plane E_{2g} mode. This clearly indicates an enhancement of interlayer interactions with pressure. The multitude of pressure-dependent Raman spectra characteristics (FWHM, intensity

ratio, peak spacing) are well correlated with the pressure-dependent resistivity, all showing an abrupt or particular response in the IS region. These strong correlations provide unambiguous experimental and theoretical support for the semiconducting to metallic phase transition in multilayered MoS₂.

Since the neighboring planes of the sulfur atoms along the *c*-axis are bonded by weak vdW forces, the *c* axis contracts two times more than the *a* axis below 28 GPa, exhibiting strong anisotropic compressional properties. The *c/a* lattice-parameter ratio decreases monotonically with pressure up to 19 GPa, which indicates that the interactions between the adjacent planes of sulfur atoms become stronger under pressure. We note that the *c/a* curve profile shows discontinuity at approximately 19 GPa. Similar behavior was also reported by Aksoy *et al.*⁹⁸ and can be attributed to a pressure-induced structural distortion in which MoS₂ layers slide from the original 2H_c-MoS₂ to the 2H_a-MoS₂ structure²⁴. Based on theoretical studies by Hromadová *et al.*, the peak positions in Raman measurements under high pressure coincide with the electronic properties of the emergent 2H_a-MoS₂ phase. We thus conclude that the observed changes in the electrical and vibrational response can be solely attributed to an iso-structural electronic phase transition.

Conclusion

We have demonstrated for the first time that a drastic drop in resistivity can be attributed to an electronic phase transition from semiconducting to metallic in multilayered MoS₂, which is further corroborated by *in-situ* temperature-dependent resistivity measurement and Raman spectroscopy. Our results can be applied to novel MoS₂ devices, where pressure can be an external stimulus to dynamically control the band gap and tune the opto-electronic response or

photoconductive gain. The experimentally observed transition is in good agreement with *ab-initio* theoretical calculations, allowing one to predict the thickness dependence of the critical transition pressure. Based on the similarity in the crystal and band structure of the semiconducting transitional metal dichalcogenides, the observed electronic phase transition in MoS₂ is likely to be experimentally accessible in MoSe₂, WS₂, and WSe₂ as predicted in a previous work²¹. The combined experimental results and theoretical insights indicate a new opportunity for the development of multi-physics device concepts with coupled mechanical, electrical, and optical properties based on the tunable and unique material structure of the semiconducting transitional metal dichalcogenides.

Supplementary Figures

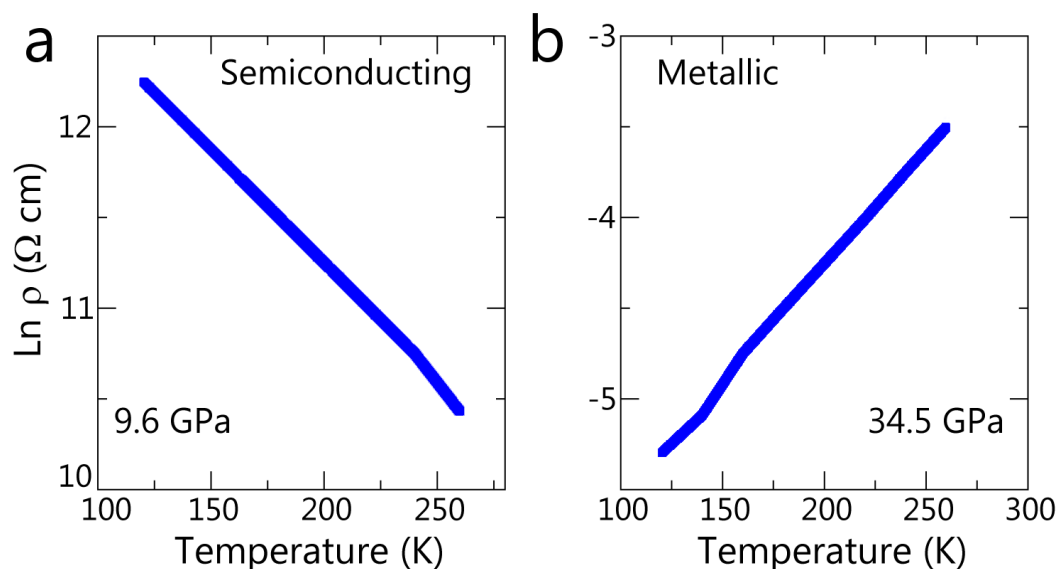


Figure 20. Theoretical temperature-dependent resistivity of MoS_2 at selected pressures. (a) Semiconducting state, and (b) metallic state.

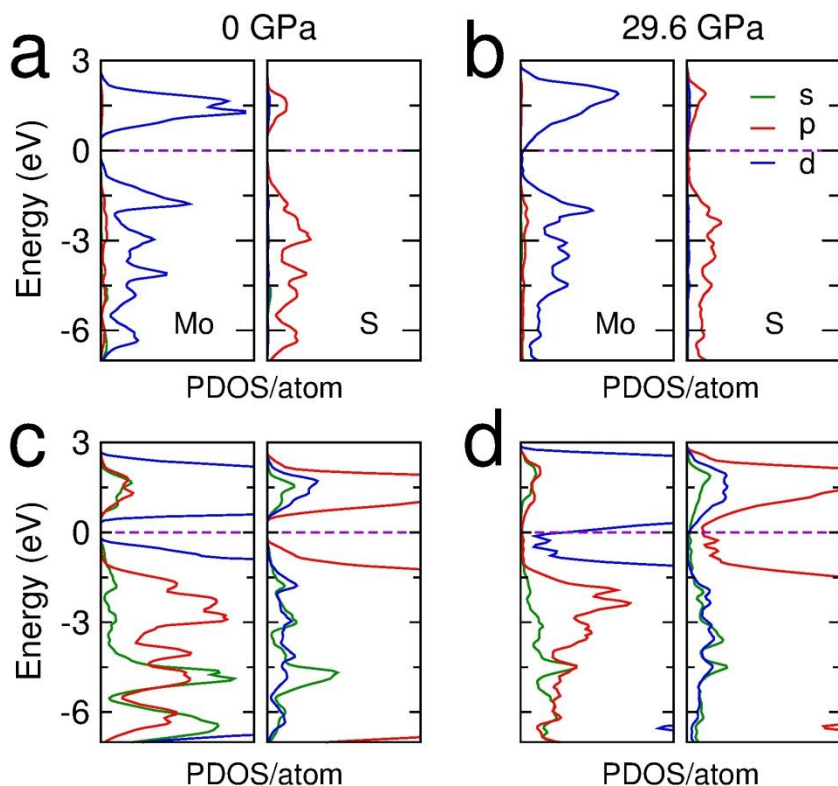


Figure 21. Partial density of states (PDOS) of Mo and S in multilayered MoS_2 at representative pressures. (a) PDOS at 0 GPa and (b) PDOS at 29.6 GPa. Zoom-in PDOS at (c) 0 GPa and (d) 29.6 GPa. The bands on each side of the band gap originate primarily from the d states of the transition metal for both 0 GPa and 29.6 GPa. For the unpressurized MoS_2 , the CBM

and the VBM are constituted by Mo-*d* and S-*p* orbitals while at higher pressures, contributions to CBM from Mo-*d* and S-*p* orbitals decrease, while contributions from S-*d* orbitals increase. The Fermi level is shown as the dotted line.

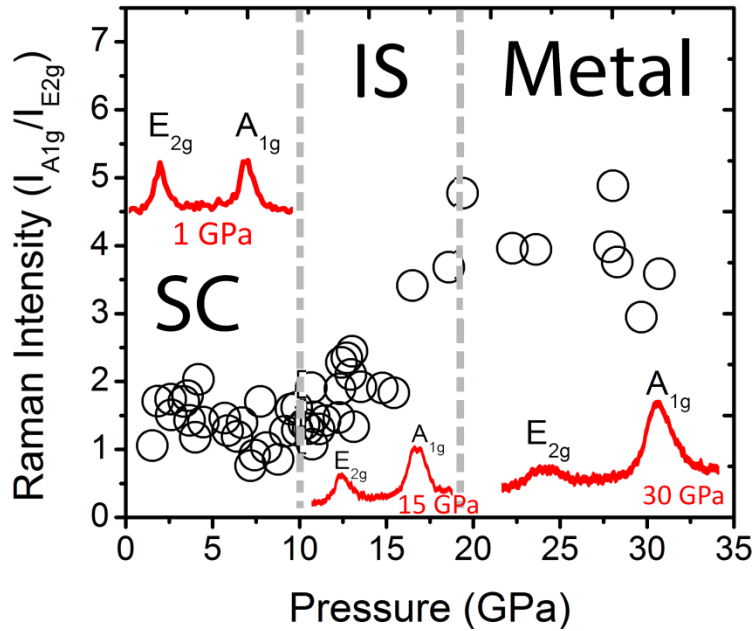


Figure 22. Raman intensity ratio. $I_{A_{1g}}/I_{E_{2g}}$ ratio as a function of pressure shows an increase in the IS region. The maximum intensity ratio is observed in the metallic state. The inset shows the relative intensities of the E_{2g} and A_{1g} peaks at selected pressures.

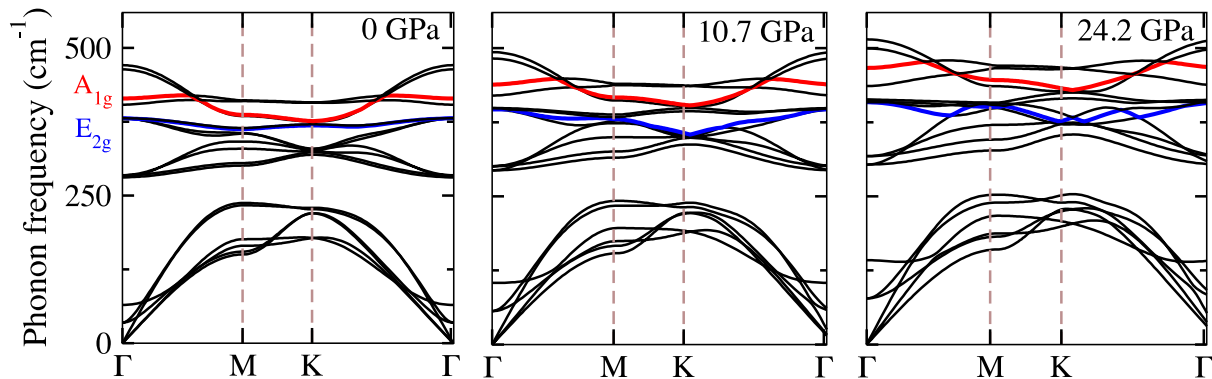


Figure 23. Theoretically predicted phonon bands at representative pressures. The results indicate that the splitting in the bands increases with increasing pressure. The E_{2g} (blue line) and A_{1g} (red line) modes are identified from the dispersion curves at the Γ point and their frequencies at ambient conditions are 375.5 cm^{-1} and 405.5 cm^{-1} , respectively.

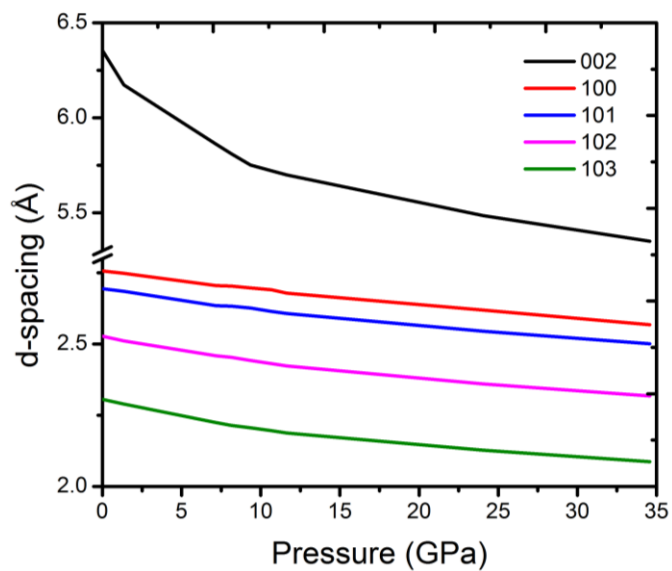


Figure 24. Theoretically-predicted XRD results for multilayered MoS₂ as a function of pressure. The *d*-spacings of representative lattice planes as a function of pressure. No new peaks are observed.

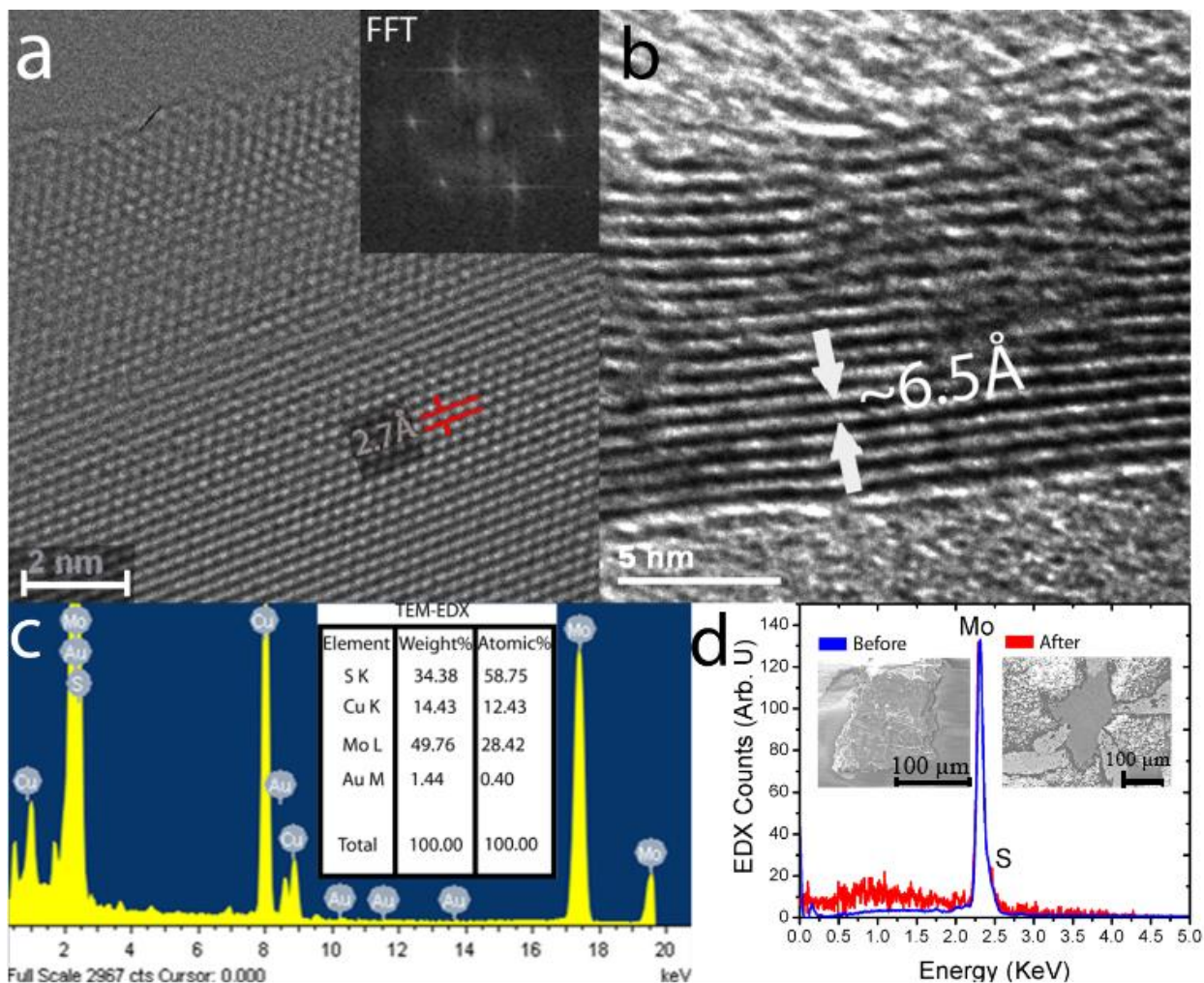


Figure 25. Electron microprobe analyses of the multilayered MoS₂ sample. (a) HR-TEM image of the honeycomb structural arrangement of the multilayered MoS₂. Inset: FFT image of the pristine multilayered MoS₂ sample. (b) Cross-sectional HR-TEM image of a multilayered MoS₂ before compression showing the interlayer distance to be approximately 6.5 Å. (c) TEM-EDX spectra of the multilayered crystalline MoS₂ after decompression. (d) SEM-EDX spectra for the multilayered MoS₂. Inset: SEM images are shown before loading and after decompression.

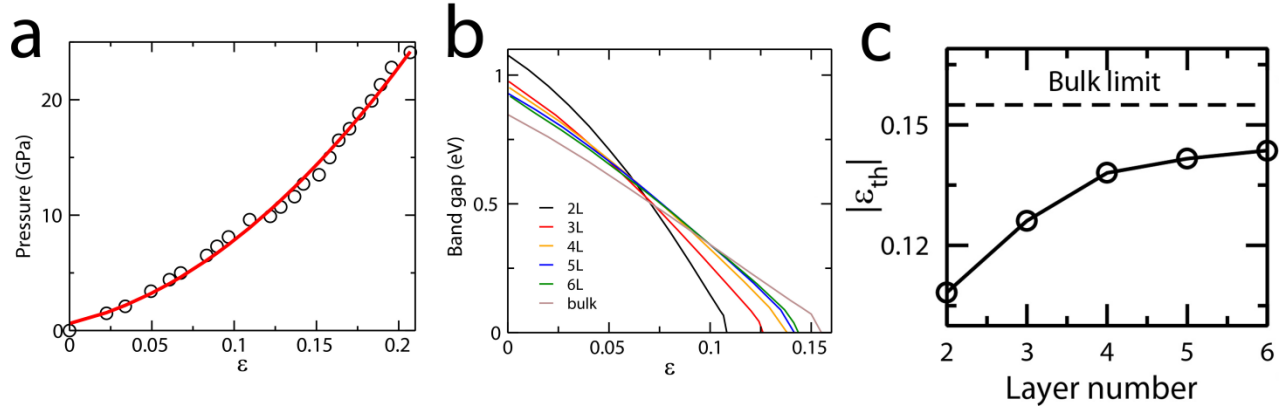


Figure 26. Pressure-strain relation and the theoretical band gap dependence on strain. (a) Pressure relationship to compressive strain, which allows correlation of the applied pressures in this work to strain. The red line is a quadratic fit to the data. (b) Band gap reduction with normal compressive strain applied to multilayered (bi-layer, tri-layer, four-layer, five-layer, six-layer and bulk) MoS₂. (c) Predicted critical strain threshold ($|\epsilon_{th}|$) as a function of the number of layers. The critical strain threshold is the strain corresponding to the closure of the band gap.

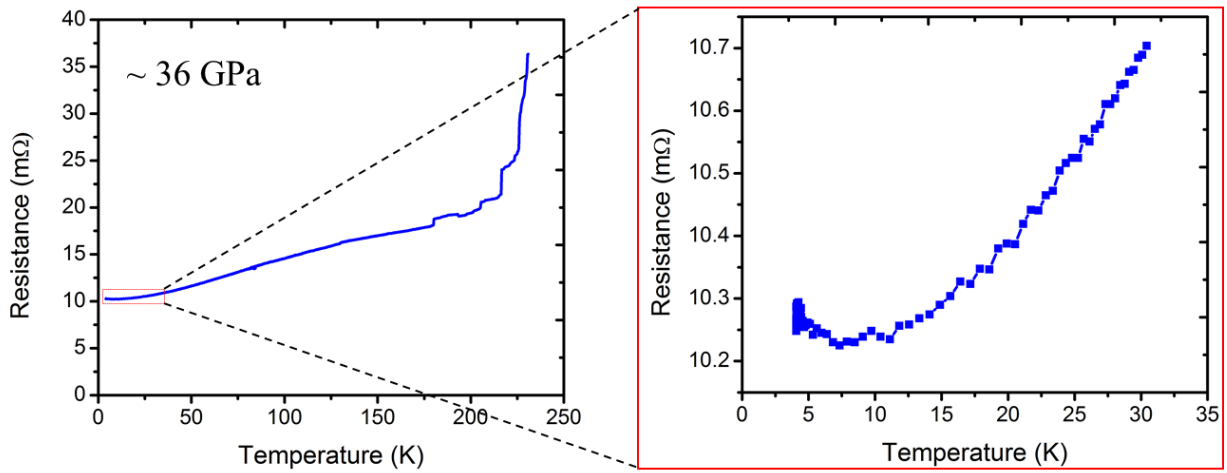


Figure 27. Electrical resistance behavior with temperature. No superconductivity of multilayered MoS₂ is observed at ~36 GPa.

Pressure-Dependent Optical and Vibrational Properties of Monolayer MoS₂

Introduction

Controlling the band gap by tuning the lattice structure through pressure engineering is a relatively new route for tailoring the optoelectronic properties of two dimensional (2D) materials. We investigate the electronic and lattice vibrational dynamics of the distorted monolayer 1T-MoS₂ (1T') and the monolayer 2H-MoS₂ *via* a diamond anvil cell (DAC) and density functional theory (DFT) calculations. The direct optical band gap of the monolayer 2H-MoS₂ increases by 11.7% from 1.85 eV to 2.08 eV, which is the highest, reported for a 2D transition metal dichalcogenide (TMD) material. DFT calculations reveal a subsequent decrease in the band gap with eventual metallization of the monolayer 2H-MoS₂, an overall complex structure-property relation due to the rich band structure of MoS₂. Remarkably, the metastable 1T'-MoS₂ metallic state remains invariant with pressure, with the J₂, A_{1g}, and E_{2g} modes becoming dominant at high pressures. This substantial reversible tunability of the electronic and vibrational property of the MoS₂ family can be extended to other 2D TMDs. These results present an important advance toward controlling the band structure and optoelectronic properties of monolayer MoS₂ via pressure, which has vital implications for enhanced device applications.

Results and discussion

Among the great variety of exfoliable materials, transition metal dichalcogenides (TMD) have demonstrated promising optoelectronic properties. Interestingly these properties can be largely tuned by varying the thickness,⁹⁹ by modifying the crystal structure¹⁰⁰ or by applying strain on the TMDs.⁸¹ Pressure engineering of the two-dimensional (2D) layered crystals is still a relatively new field with many possible routes for further investigations and optimization to fully realize their potential in materials engineering.^{72,101-104} Being able to reversibly tune the band gap and structure of 2D materials by inducing pressure allows for exploring changes in photonic¹⁰⁵, mechanical¹⁰⁶ and electronic¹⁰⁷ properties at different hydrostatic pressures. The effects of hydrostatic pressure on 2D materials are important to understand, particularly for applications such as flexible electronics.¹⁰²

The transition metal dichalcogenide family, which consists of 2D layered compounds, exhibits a similar laminar structure as graphene and has been investigated for several optoelectronic^{54,99,108,109} and flexible^{102,110} electronics. One representative TMD that has gained significant interest is molybdenum disulfide (MoS_2), which is composed of a single layer of Mo atoms covalently bonded between two laminar sheets of S atoms. The natural bulk 2H- MoS_2 is a semiconductor that has an indirect band gap of 1.3 eV while its monolayer form has a direct band gap of 1.85 eV due to the lack of interlayer interactions in thinner layers.⁹⁹ Furthermore, depending on the arrangements of sulfur atoms in the lattice, Mo can be coordinated either by six sulfur atoms in either an octahedral (1T), a distorted 1T (1T'), or a trigonal prismatic (2H) polytype⁵⁴ (**Figure 20a**). This different coordinated structure also changes the electronic structure of the material. The 1T'- MoS_2 is metallic while the 2H- MoS_2 is semiconducting.

The two main Raman modes in the monolayer 2H-MoS₂ are the A_{1g} and the E_{2g} mode. The out-of-plane A_{1g} mode occurs due to opposing vibrations of the two S atoms with respect to the Mo atom. The E_{2g} mode is associated with the in-plane vibration of the Mo and S atoms, in opposite directions to one another. For the 1T'-MoS₂, the experimentally observed J₁ mode involves two different types of vibrations: one at 152.68 cm⁻¹, which is an out-of-plane motion of each stripe of the Mo atoms inside the zig-zag chain, and the other mode at 157.64 cm⁻¹, which is an in-plane shearing vibration of one stripe of atoms with respect to the other atom in the chain. Both of these modes appear as a single peak at room temperature. The J₂ peaks at ~226 cm⁻¹ arises from the motion of two zig-zag chains relative to each other, while the mode 330.29 cm⁻¹, named as J₃, tends to break each zigzag chain in two stripes with a slight out-of-plane component (**Figure 20b**). Due to the atomic arrangements of the 1T'-MoS₂ and 2H-MoS₂ phases, these Raman modes with various magnitudes of activities can be used to decipher the lattice dynamics of the monolayer polytypes (**Figure 20c**).

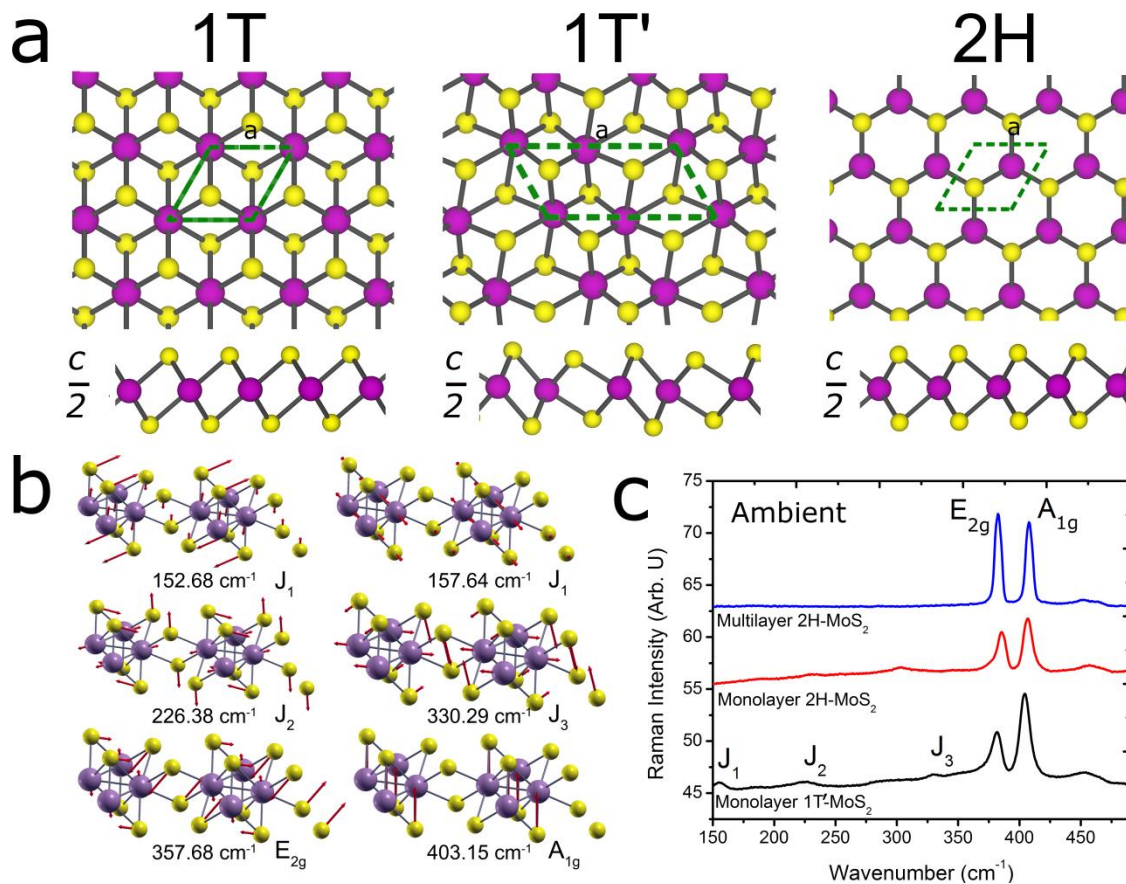


Figure 28. Structural and Vibrational Properties of Monolayer MoS₂ Polytypes. (a) Schematic atomic arrangements of the monolayer MoS₂ showing the a (in-plane direction) and the cross-section c (out-of-plane) view of the monolayer 1T-MoS₂, 1T'-MoS₂ and 2H-MoS₂. (b) Raman active modes of the MoS₂ family. For the 1T'-MoS₂, the J₁ mode is composed of two Raman active modes that are close to one another and appear as one peak at room temperature. (c) Raman active modes for the restacked monolayer 1T'-MoS₂ and monolayer and bulk 2H-MoS₂. The J₁, J₂, and J₃ modes are only prominent in the 1T'-MoS₂ phase.

It has been found experimentally that these two phases can transition to one another *via* interlayer atomic plane gliding, which displaces one of the S planes and changes its electronic state.^{54,100,111} Another way to controllably alter the electronic properties is to mechanically distort the lattice structure by applying uniaxial, biaxial, or hydrostatic strain.^{28,112,113} The majority of research in the field pertains to theoretical calculations on how the distortion of the 2H and 1T'-MoS₂ lattice can lead to changes in their photonic and electronic structure.^{21,70,113-115}

Experimentally, it has been a challenge to exert hydrostatic pressure homogeneously across a 2D

sample, and only a nominal compressive strain of 0.2% or a uniaxial strain of 10% can be exerted with elaborate setups.^{106,107}

In the present study, we have investigated the MoS₂ family (1T'-MoS₂ and both monolayer and bulk 2H-MoS₂) under extreme hydrostatic pressures of up to 30 GPa. A diamond anvil cell (DAC) with a soft neon pressure medium was used to apply a hydrostatic pressure uniformly across the sample. The DAC experiments allow fundamental studies of the effects of high strain levels on the properties of materials, MoS₂ in this case. This sort of study is important for probing the intrinsic response of the strain-property relations in a controlled environment. The insights provided by this study can guide practical realization of strained MoS₂ devices. The DAC methodology also permits us to investigate the modulation of the band gap, the shift from a direct to an indirect band gap, and the altered phononic properties of both the monolayer 2H-MoS₂ and 1T'-MoS₂ under applied hydrostatic pressures. These results show, that for the monolayer 2H-MoS₂ polytype a ~12% increase in band gap is observed. Although a higher pressure is not experimentally achievable for the time being, a metallization at 68 GPa is predicted by theoretical calculations. The semiconductor to metal transition occurs at a much higher pressure than that in the bulk counterpart which metalizes at ~19 GPa. For the 1T'-MoS₂ polytype, the out-of-plane vibrations are hindered by the hydrostatic pressure, allowing only the J₂, A_{1g}, and E_{2g} vibrational modes to become dominant at pressures past 27 GPa. Our combined experimental and theoretical results allow for a coherent understanding of the vibrational, optical, and electronic properties of TMD materials as a function of the number of layers and layer geometry under hydrostatic pressure.

Raman spectroscopy, being fast and non-destructive, is a powerful diagnostic tool to investigate the vibrational and physical properties of MoS₂. Raman spectroscopy has been used to study 2H-

MoS₂ to determine the number of layers,¹¹⁶ the effect of pressure on the 2H-MoS₂ lattice,¹¹⁷⁻¹¹⁹ and to determine the level of doping¹²⁰ and defects.^{121,122} To understand the electronic and mechanical stability of the MoS₂ polytypes, we have studied the monolayer and bulk 2H-MoS₂ as well as restacked monolayer 1T'-MoS₂ under hydrostatic pressure.

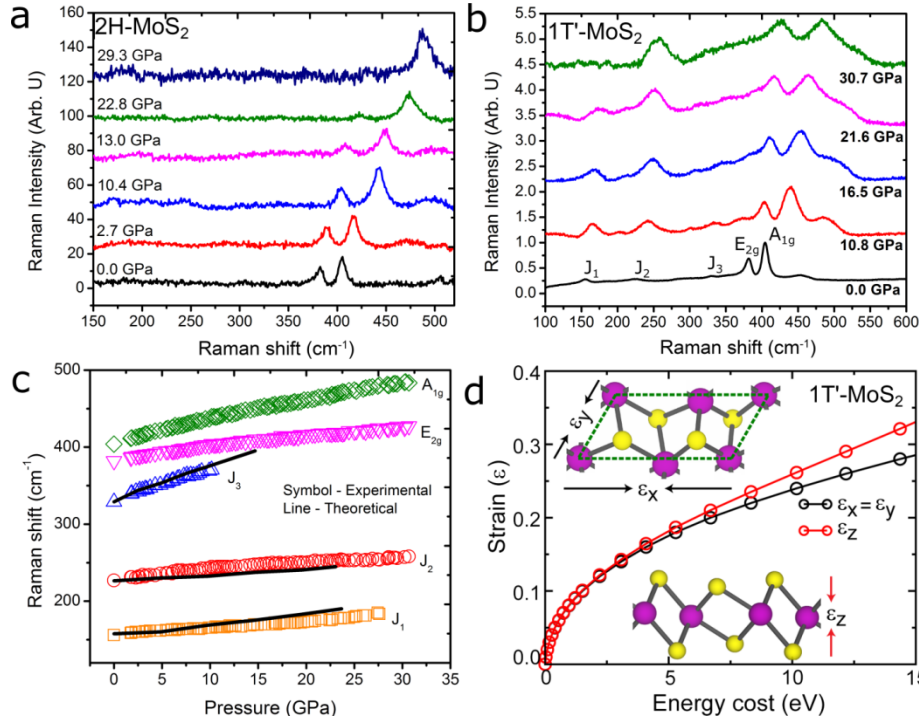


Figure 29. Pressure-Dependent Lattice Vibrational Properties of Monolayer 1T'- and 2H-MoS₂. Representative Raman spectra of the monolayer (a) 2H-MoS₂ and (b) 1T'-MoS₂ at high pressures. For the 2H-MoS₂ polytype, the E_{2g} mode diminishes, while the dominant Raman modes are J₂, E_{2g}, and A_{1g} for 1T'-MoS₂ at pressures above 27 GPa. (c) Pressure-dependent Raman frequencies with variation in pressure for the five Raman active modes. The J₃ merges with the E_{2g} mode at around 10 GPa while the J₁ diminishes at 27 GPa. The solid line indicates the theoretical agreement with the J₁, J₂, and J₃ modes and further supports the phonon merging of the J₃ and E_{2g} modes. (d) Applied strain is plotted with respect to the energy required to compress the in-plane and out-of-plane bonds, suggesting that the in-plane mode vibration is suppressed at higher pressures. Inset: Schematic representing the application of strain in the in-plane direction (ε_x, ε_y) (upper inset) and out-of-plane (ε_z) directions.

The lattice vibrations detected by Raman spectroscopy can reveal key changes occurring to the lattice at high pressures. In particular, hydrostatic pressure can induce a blue shift (phonon hardening) in MoS₂.²⁸ For the 2H-MoS₂ monolayer polytype, the intensity of in-plane Raman

mode (E_{2g}) starts to diminish at pressures above 16 GPa (**Figure 21a**). The intensity ratio of A_{1g}/E_{2g} also increases with pressure (**Figure S1a**) above 16 GPa. The diminishing intensity of the E_{2g} mode is attributed to the dominance of normal compressive strain on the monolayer 2H-MoS₂ under large hydrostatic pressures³⁰ which hinders the in-plane E_{2g} movement while the A_{1g} out-of-plane vibrational mode is still prominent at pressures up to 30 GPa.

Although the rate of increase is higher for A_{1g} mode (**Figure S1b**), the E_{2g} mode also increases linearly. This distinct rate of increase can be explained by analyzing the type of vibrations involved in A_{1g} and E_{2g} modes. The A_{1g} modes originate from transverse vibrations of S-S atom, however the E_{2g} mode emerges from longitudinal vibrations of Mo and S atoms in opposite directions. The change in Mo-S bond length (in-plane movement of atoms) plays a significant role in determining the behavior of E_{2g} mode. As the hydrostatic pressure increases, the out-of-plane (A_{1g}) compression becomes more favorable than the in-plane (E_{2g}) compression, indicating that at higher pressures the transverse moment of S-S atom is faster than the in-plane movement of Mo-S atom (**Figure S2a**). This results in a higher rate of increase of A_{1g} mode with increasing pressure in comparison to E_{2g} mode.

Although several studies have been done on the synthesis and characterization^{54,123} of the distorted octahedral 1T'-MoS₂ polytype, the lattice vibrations at extreme hydrostatic pressure conditions have not yet been studied under high pressure. Previous theoretical studies have shown the breaking of lattice symmetry in 1T'-MoS₂ when tensile and compressive strain are applied.¹¹⁴ The 1T'-MoS₂ phase shows three Raman active modes that are not present in the trigonal prismatic 2H-MoS₂ polytype. These three extra modes are the J_1 , J_2 , and J_3 which show up at 150 cm⁻¹, 225 cm⁻¹, and 325 cm⁻¹, respectively at ambient pressure. As the hydrostatic pressure increases, J_3 becomes indistinguishable from the E_{2g} mode at ~10 GPa while J_1 and J_2

are still prominent at higher pressures. The broadening of the J_3 mode with pressure further supports the merging phenomenon of the J_3 and E_{2g} modes (**Figure S3**). In order to confirm this phonon merging, theoretical calculations have been carried out to investigate the effect of pressure on the vibrational properties of the monolayer 1T'-MoS₂. The calculated phonon dispersion curves (**Figure S4**) at ambient pressure are consistent with the previously reported results¹²⁴ and were used to identify all the Raman active modes. The theoretically derived pressure-dependent Raman frequencies show good qualitative agreement with experimental observation. The Raman intensity increases for the J_1 , A_{1g} , and E_{2g} modes and shows the merging of the J_3 and E_{2g} modes (**Figure S5**). The J_1 Raman mode also diminishes at pressures above 22 GPa leaving just the J_2 , A_{1g} and the E_{2g} Raman modes dominant at pressures past 27 GPa (**Figure 21b**). To investigate the E_{2g} and J_3 merging in further detail, theoretical calculations were performed to find the dependence on pressure compared to the other modes (**Figure 21c**). As the hydrostatic pressure increases, the out-of-plane compression becomes favorable (0.08 Å/GPa) than the in-plane compression (0.03 Å/GPa), suggesting that at higher pressures the out-of-plane movement of the S-S atom is faster than the Mo-S movement leading to a smaller rate of increase of the E_{2g} mode (1.3 cm⁻¹/GPa) compared to the A_{1g} mode (2.5 cm⁻¹/GPa) (**Figure 21d**). The pressure dependent rate of increase for the J_1 and J_2 Raman mode is 0.9 cm⁻¹/GPa while the J_3 mode increases at 3.90 cm⁻¹/GPa. For the 2H-MoS₂ polytype, the pressure dependence on the Raman modes of the monolayer 2H-MoS₂, 1T'-MoS₂ and the bulk 2H-MoS₂ shows that the A_{1g} and E_{2g} modes for both the monolayer 2H-MoS₂ and 1T'-MoS₂ polytypes are similar (**Figure S6**). For the 2H-MoS₂ monolayer, the shift in Raman peak position increases linearly with applied pressure. The Raman shift with pressure for the A_{1g} mode is 2.6 cm⁻¹/GPa while the E_{2g} mode increases at a rate of 1.7 cm⁻¹/GPa (**Figure S1b**). The distance between A_{1g}

and E_{2g} Raman modes increases at a rate of $1.2 \text{ cm}^{-1}/\text{GPa}$ (**Figure S1c**). The A_{1g} shift for monolayer MoS_2 with pressure, in comparison to other 2D materials such as MoSe_2 , MoTe_2 , and ReS_2 , is higher, signifying that the monolayer MoS_2 has a strong dependence on pressure.¹²⁵ The deviation from the bulk MoS_2 is mainly attributed to the interlayer interactions along the out-of-plane axis, which is absent in the monolayer. Unlike the bulk 2H- MoS_2 , no intermediate phase region between the semiconducting and metallic region is observed, indicating that the monolayer MoS_2 does not undergo metallization or a structural transition at pressures up to 30 GPa. Theoretically, we predict the metallization of 2H- MoS_2 to be at ~ 68 GPa.

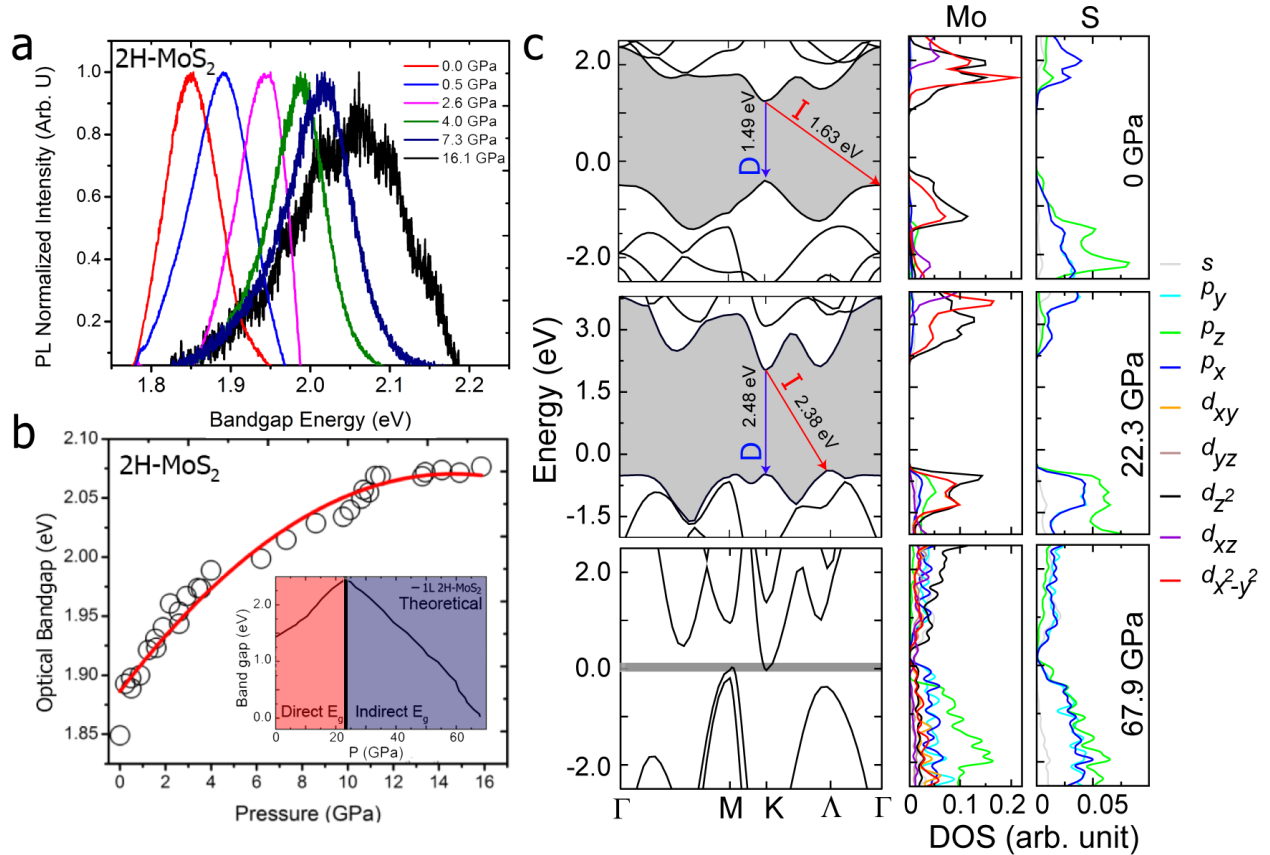


Figure 30. Pressure Modulated Photoluminescent Properties of Monolayer 2H-MoS₂. (a) Representative PL spectra as a function of pressure. An increase in the band gap with increasing pressure and then the diminishing of the PL signals at ~16 GPa indicates a direct-to-indirect band gap shift. (b) Derived band gap at high pressures. Extracted from the Lorentzian fit from the PL peaks, the band gap is shown to increase as a function of pressure. Red solid line: a polynomial fit to the experimental data described by $E_g = 1.88 + 0.03P - 8.59 \times 10^{-4}P^2$ where E_g is optical band gap and P is pressure. Inset: The theoretical prediction of the direct-to indirect band gap transition. (c) Band gap diagrams at K, Λ , and Γ point at two representative pressures of 0 GPa and 22.3 GPa depicting the direct to indirect transition. Here D and I indicate the direct and indirect band gaps respectively. The observed direct and indirect band gap values are also presented for clarity. At 0 GPa, the E-k diagram indicates a direct-band gap between the CBM and the VBM, while at 22.3 GPa, band gap shift form direct (from in between K-K' points) to indirect in between K- Λ points at 22.6 GPa that agrees with the experimental observations. At around 67.9 GPa the valence band maxima (VBM) and the conduction band minima (CBM) cross the Fermi level, leading to a semiconductor-to-metal transition.

Due to the inherent direct band gap (1.85 eV) of the monolayer 2H-MoS₂, the photonic and electronic band structure can be probed by the photoluminescence (PL) spectroscopy.¹²² This strong PL emission is only observed in the monolayer 2H-MoS₂ and is attributed to the slow

electronic relaxation that is unique to its electronic structure. The PL signal for the bilayer and trilayer are much weaker.¹²² Our PL spectral measurements on the monolayer 2H-MoS₂ show that the electronic band structure can be significantly modulated by hydrostatic pressure (**Figure 22a**) at a rate of 30 meV/GPa below 5 GPa. At higher pressures, the direct band gap gradually increases to 2.08 eV at ~12 GPa showing a significant 11.7% change in band gap (**Figure 22b**) while increasing the PL full width half maximum (FWHM) (**Figure S1d**). Although this increase in the direct band gap is reversible (**Figure S7**), the rate of increase can be altered depending on the pressure medium. This can significantly modify the photonic and electronic characteristics of 2D materials under high pressure.^{72,80,105} Since we have used an inert, soft Ne pressure medium in our experiments, our results therefore represent more intrinsic features of the system without dopant effects. The polynomial increase in the band energy is in agreement with theoretical DFT calculations, which show an increase in the direct band gap at the K-K' point. The theoretical band gap is underestimated because the presence of artificial self-interaction and the absence of the derivative discontinuity in the exchange-correlation potential with the PBE/GGA methods.⁸⁹ The initial trend in band gap as supported by the PL experiments (**Figure 22b**) shows an increase at the K-K' point. The *in situ* FWHM map of PL Spectra (**Figure S8**) increases from 24.7 nm at 0.6 GPa to 58.7 nm at 12.5 GPa and diminishes to the background noise level at pressures over 16 GPa at room temperature. This increase in the FWHM implies a cross-over point to the direct-to-indirect band gap⁸¹ at the K-K' point at approximately 16 GPa. This direct to indirect band gap shift was further conformed by DFT calculations. The ambient theoretical band gap initially lies in-between K-K' point until a pressure of 22.3 GPa is reached. At 22.3 GPa, a direct-to-indirect transition indicates that the conduction band minima (CBM) and the valence band maxima (VBM) are no longer at the K-K' inter-band (**Figure 22c**), but rather shift to the K- Λ point.

Theoretical calculations reveal that the band gap of 2H-MoS₂ monolayer first increases up to a pressure of ~22 GPa is reached. Beyond this pressure, the band gap gradually decreases, eventually leading to the metallization of monolayer 2H-MoS₂ at around 68 GPa.

To understand the mechanism for this band gap change and the semiconductor to metal (S-M) transition under hydrostatic pressure, we analyze the contribution from different molecular orbitals by performing angular momentum projected density of states (LDOS) calculations. At lower pressures, both valence (VB) and conduction bands (CB) are mainly composed of Mo- d_x^2 , d_y^2 , d_z^2 and S- p_x , p_y orbitals (**Figure 22c**). With increasing pressure, these orbitals move away from the Fermi level, resulting in an increase in band gap up to 22.3 GPa pressure. At higher pressure, the out-of-plane compression becomes more dominant (**Figure S2b**) which makes the Mo d_z^2 , d_{xz} and p_z orbitals interact strongly with S- p_z and p_x orbitals. This strong intra-layer hybridization between the orbitals mentioned above leads to a decrease in band gap after ~22 GPa pressure and finally closing of the band gap at higher pressure (68 GPa). For the monolayer 2H-MoS₂, in-plane intra layer interactions play a dominant role in the metallization at 67.9 GPa. It was found in our previous study of the bulk MoS₂ that interlayer interactions play a critical role in the metallization.²⁸ It is therefore expected that as the number of layers increases, the critical pressure or critical volume strain (**Figure S10**) at which the metallization occurs decreases (**Figure 23a**). The metallization of the bilayer, trilayer, and bulk 2H-MoS₂ (**Figure 23a and 4b**) under high pressure can be understood by the interaction of electron-donating sulfur atoms between the van der Waals gaps.^{17, 21} The transition pressure for MoS₂ therefore decreases as the number of layers increases. As experimentally observed, the monolayer 1T'-MoS₂ shows metallic behavior (**Figure S7**), unlike the 2H-MoS₂ polytype which is semiconducting in nature.

For the 2H-MoS₂, the valence and conduction bands are mainly composed of the *d*-orbitals of Mo and *p*-orbitals of S atoms (**Figure S11a**). Upon application of hydrostatic pressure the extent of hybridization between Mo *d*-orbitals (mainly d_z^2 , d_{xy} and $d_{x^2-y^2}$) and S *p*-orbitals increases, thus increasing the overlap between conduction and valence bands resulting in an enhanced metallization (**Figure S11b**).

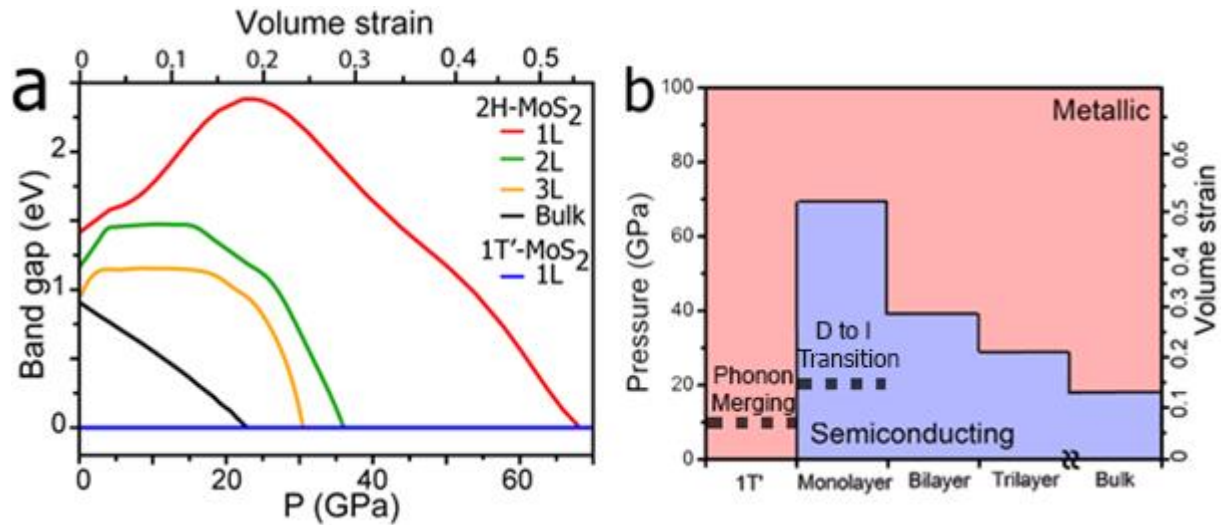


Figure 31. Electronic Structures of the MoS₂ Polytypes under Hydrostatic Pressure. (a) Band gap energies of the polytypes as a function of pressure. **(a)** Below 22.3 GPa, an increase in the direct band gap is observed for the monolayer 2H-MoS₂. While for higher pressure, the band gap decreases with strain and closes at 67.9 GPa indicating a metallization transition. A smaller critical pressure of 39.2 GPa and 29.5 GPa is observed for the bilayer and trilayer 2H-MoS₂ respectively. **(b)** Hydrostatic pressure effects on monolayer, bilayer, trilayer, bulk MoS₂ and 1T'-MoS₂. A metallic state is more easily reached in the bulk state since more interlayer interactions are present.

We have measured an 11.7% difference in the direct band gap of the 2H-MoS₂ from 1.85 eV at ambient pressure to 2.08 eV at 16 GPa before the PL signal diminished and could no longer be resolved at higher pressures and room temperature. For comparison, a 3.3% difference in direct band gap was found by S.P. Lau *et al.*¹⁰⁷ a 3.0% difference by G. A. Steele *et al.*¹²⁶ and a 5.4% difference by Dou *et al.*¹⁰⁵ for the monolayer 2H-MoS₂. To further understand the electronic and phononic properties, DFT calculations were conducted to show that a critical pressure of 67.9 GPa is required to metalize the monolayer 2H-MoS₂. The 1T'-MoS₂ behaves as a metal at ambient pressure and exhibits three more Raman active modes (J_1 , J_2 , and J_3) in comparison to the 2H-MoS₂ which exhibits just the A_{1g} and E_{2g} modes. At pressures above 10 GPa and 27 GPa, we have observed the diminishing of the out-of-plane J_1 and J_3 Raman modes respectively due to higher susceptibility to hydrostatic pressure along the out-of-plane axis. At 10 GPa, the J_3 mode

starts to merge with the E_{2g} mode. The suppression of the J_1 mode at ~ 27 GPa is attributed to the large hydrostatic pressure on the lattice implying that the effect of pressure is more pronounced for this mode and is more sensitive to pressure. Since this process is reversible for both the 2H-MoS₂ and the 1T'-MoS₂, the distortion of the lattice is predicted to be a transitory structural modification. The total energy calculation also reveals that monolayer MoS₂ is the most stable phase under the applied pressure range (**Figure S12**), and confirms that there is no phase transformation between 2H and 1T' phase within the studied range of pressure.

Strain engineering of 2D layered materials is a relatively new field with possible routes for further investigations to fully realize their potential in customizing material behavior.

Here, the interplay of the structural and optoelectronic properties is successfully described for the MoS₂ family. The monolayer 2H-MoS₂ differs from its bulk counterpart since the bandgap increases by $\sim 12\%$ with applied hydrostatic pressure due to the absence of interlayer interactions. For the intrinsically metallic 1T'-MoS₂, interlayer structural distortion is prevalent resulting in phonon merging of two Raman active modes (J_1 and E_{2g}) at high pressures. The large reversible bandgap modulation of semiconducting MoS₂ is attractive for highly tunable optoelectronics, nanoelectronics and flexible electronics and can enable new opportunities based on the dynamic strong electron-phonon coupling.

Supplementary Figures

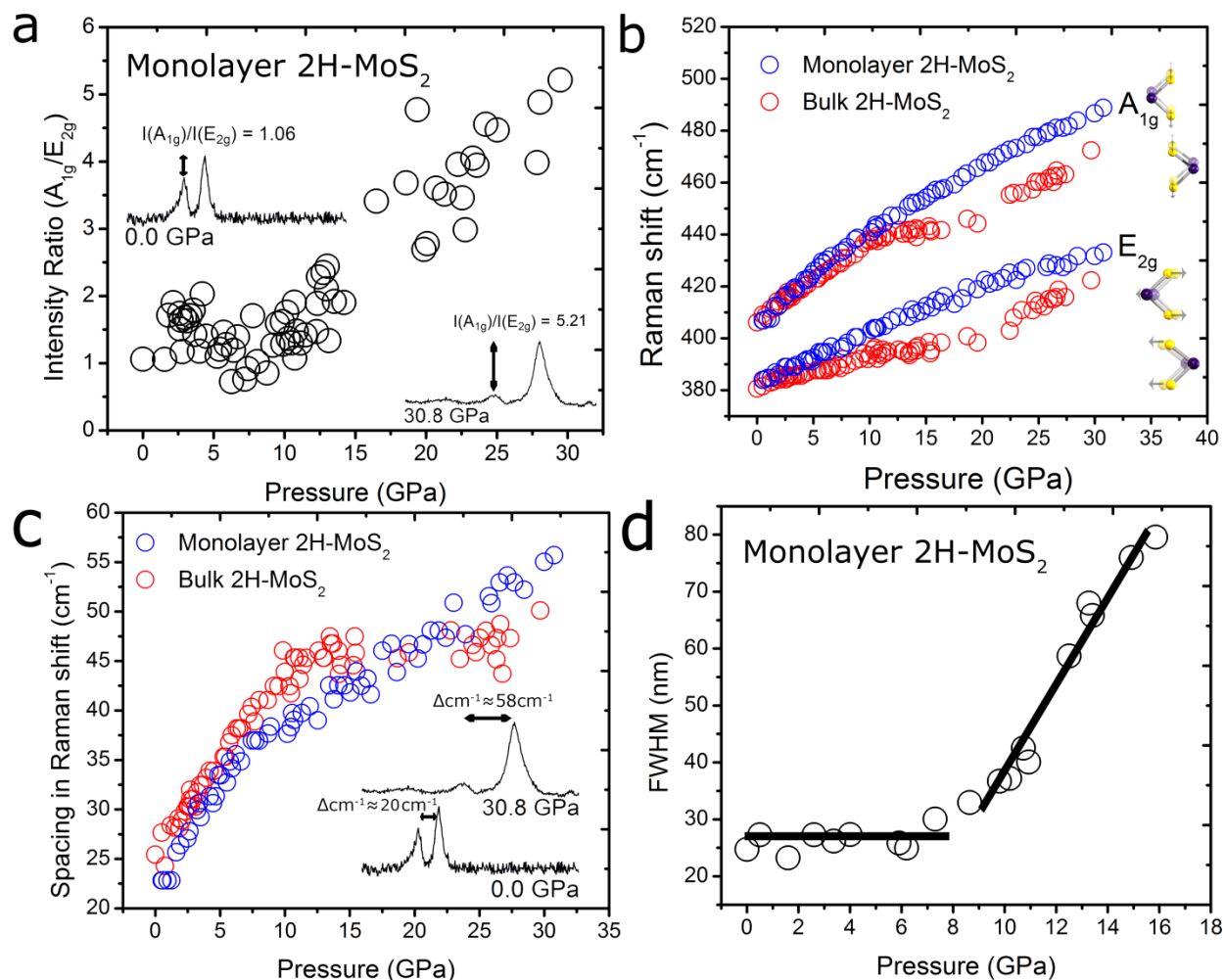


Figure 32. Vibrational and Optical Properties of Bulk and Monolayer 2H-MoS₂ at High Pressures. (a) Intensity ratio of the A_{1g} and E_{2g} peaks. The E_{2g} mode is observed to diminish in comparison to the A_{1g} . The insets show the relative intensities of the E_{2g} and A_{1g} peaks at selected pressures. (b) Pressure dependence of the Raman frequencies of the A_{1g} and the E_{2g} modes as a function of pressure. The behavior of these vibrational Raman modes in monolayer 2H-MoS₂ at high pressures (blue circles) deviates significantly from that of the bulk counterpart (red circles) due to the absence of interlayer interactions. Inset: representative vibrations involved in A_{1g} and E_{2g} modes. The A_{1g} modes originate from transverse vibrations of S-S atom, however the E_{2g} mode emerges from longitudinal vibrations of Mo and S atoms in opposite directions. (c) Raman frequency separation between the A_{1g} and E_{2g} peak as a function of pressure for monolayer and bulk 2H-MoS₂. Inset: representative Raman spectra highlighting the separation at 0 GPa and 30.8 GPa. The in-plane A_{1g} mode becomes more dominant in intensity than the E_{2g} past ~ 16 GPa for the monolayer 2H-MoS₂. (d) PL FWHM with pressure up to 16 GPa. The black lines serve as visual guidelines.

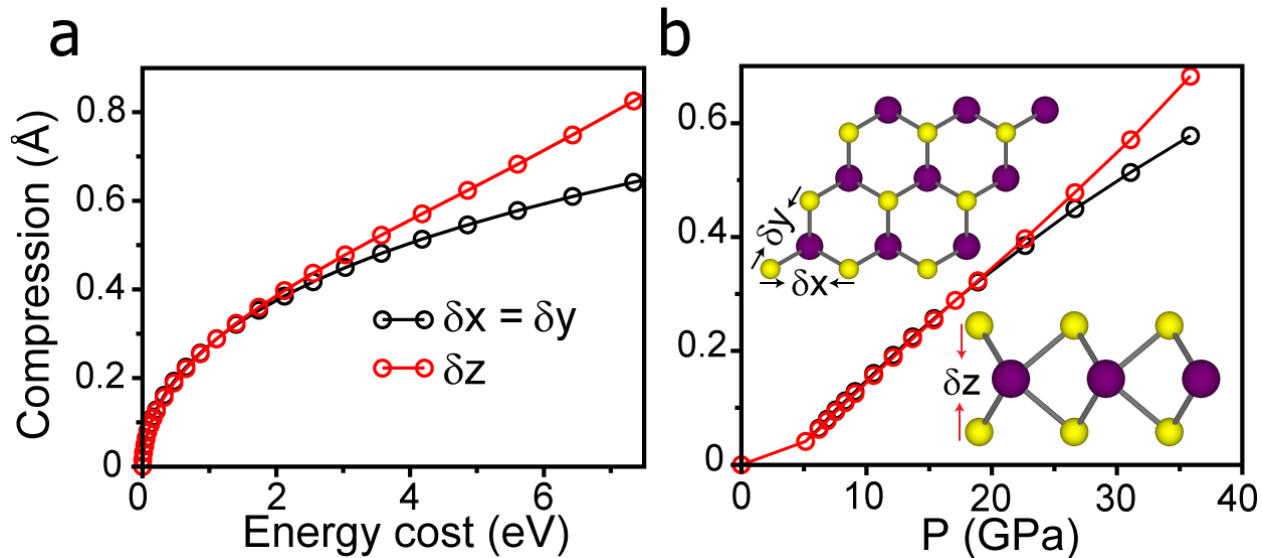


Figure 33. Modeling of hydrostatic pressure on monolayer MoS₂ (a) Compression of atoms plotted with respect to energy required to compress in-plane (x, y) and out of plane (z) bonds. (b) Compression of atoms is plotted with respect to pressure. Till 20 GPa pressure there is equal compression in all the three direction. After 18 GPa Pressure compression along z direction becomes more favorable. Inset: Schematic representing the compression of atoms in the in-plane direction (upper inset) and out-of-plane directions.

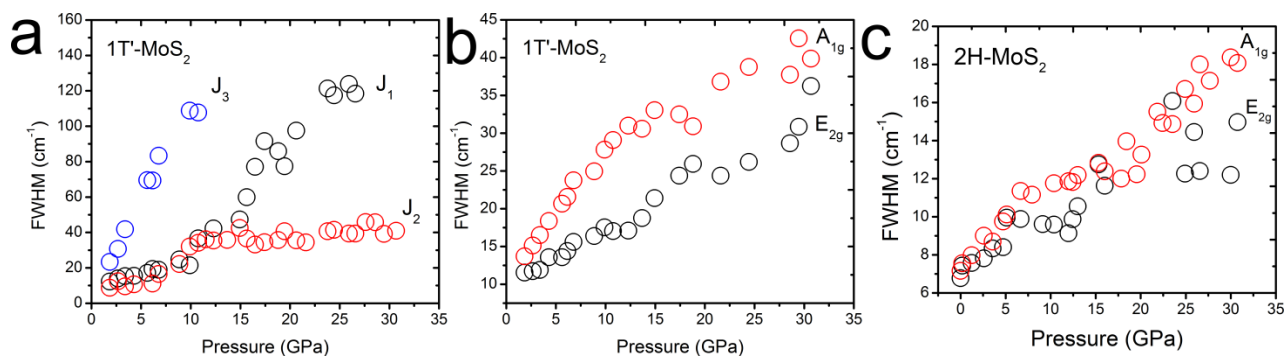


Figure 34. Raman Spectroscopic Results of Restacked 1T'-MoS₂ and monolayer 2H-MoS₂ at High Pressures. (a) FWHM of J_1 , J_2 and J_3 Raman modes. The J_3 mode tends to saturate at 10 GPa while J_2 and J_3 increase in FWHM. (b) The FWHM of the E_{2g} and A_{1g} increases with pressure. (c) The FWHM of the E_{2g} and A_{1g} Raman modes for 2H-MoS₂. The FWHM is notably smaller for the 2H-MoS₂ monolayer than the 1T'-MoS₂ since the J_3 mode merges with the E_{2g} mode.

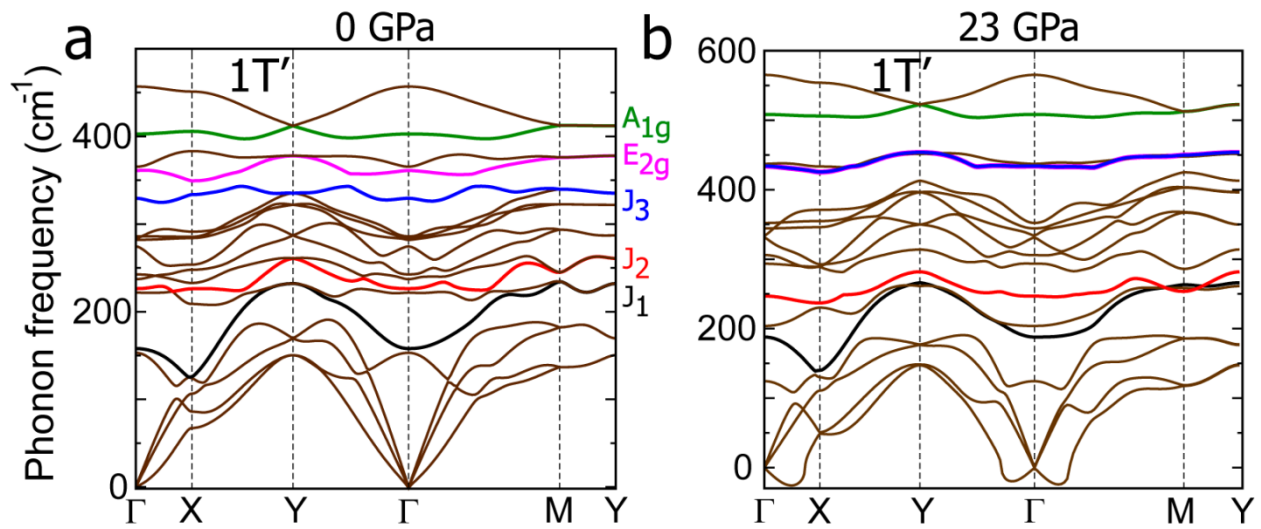


Figure 35. Phonon Dispersions for Monolayer 1T'-MoS₂ at representative pressures. The Raman active modes for 1T'-MoS₂ are highlighted with different colors for clarity at (a) 0 GPa and (b) 23 GPa. The Raman active A_{1g}, E_{2g}, J₁, J₂ and J₃ modes are identified from the dispersion curves at the Γ point. As can be seen in case of 1T'-MoS₂ three new modes J₁, J₂ and J₃ appear, whereas the frequency of the E_{2g} mode decreases significantly compared to bulk MoS₂. The J₃ mode merges with the E_{2g} mode at ~10 GPa.

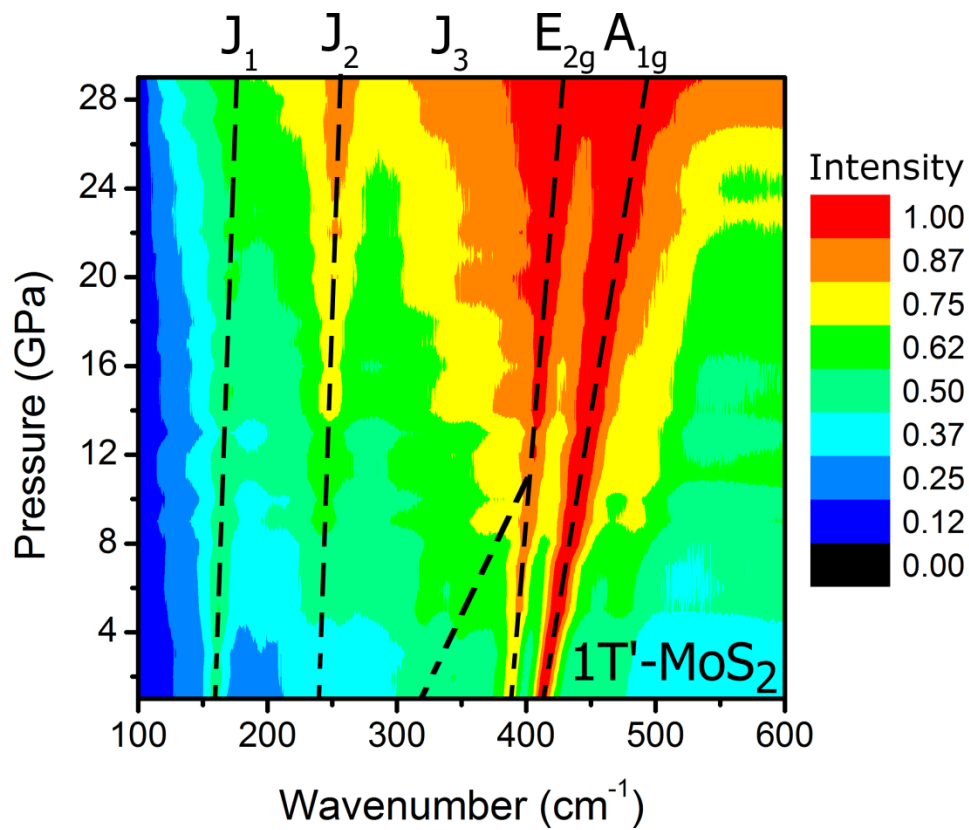


Figure 36. Raman Intensity Map of 1T'-MoS₂. The pressure dependence Raman shows the shift and broadening of the 1T'-MoS₂ Raman active modes. The dominant Raman active modes at high pressure are J₂, E_{2g}, and A_{1g}.

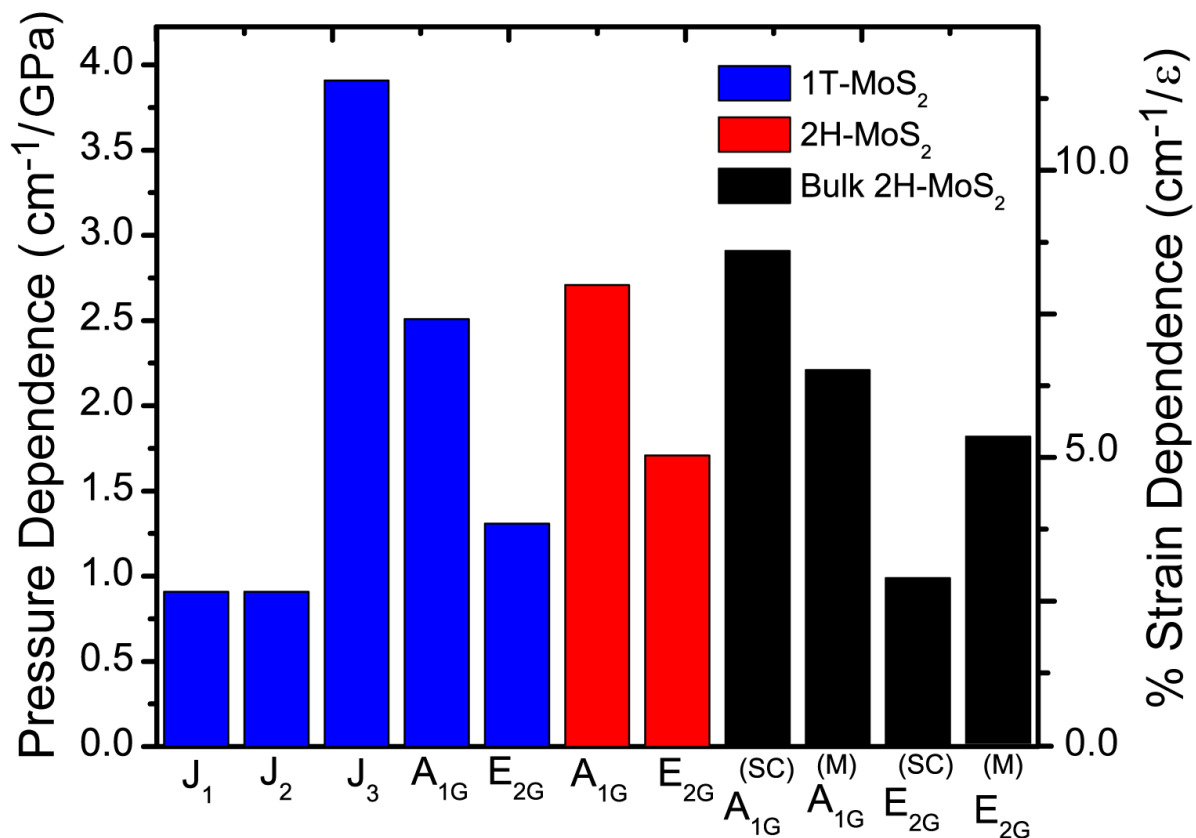


Figure 37. Raman Shift with Pressure. The pressure dependence of the Raman modes for the monolayer 2H and 1T'-MoS₂ polytypes compared to the bulk 2H-MoS₂ analog in their semiconducting (SC) and metallic (M) regime.

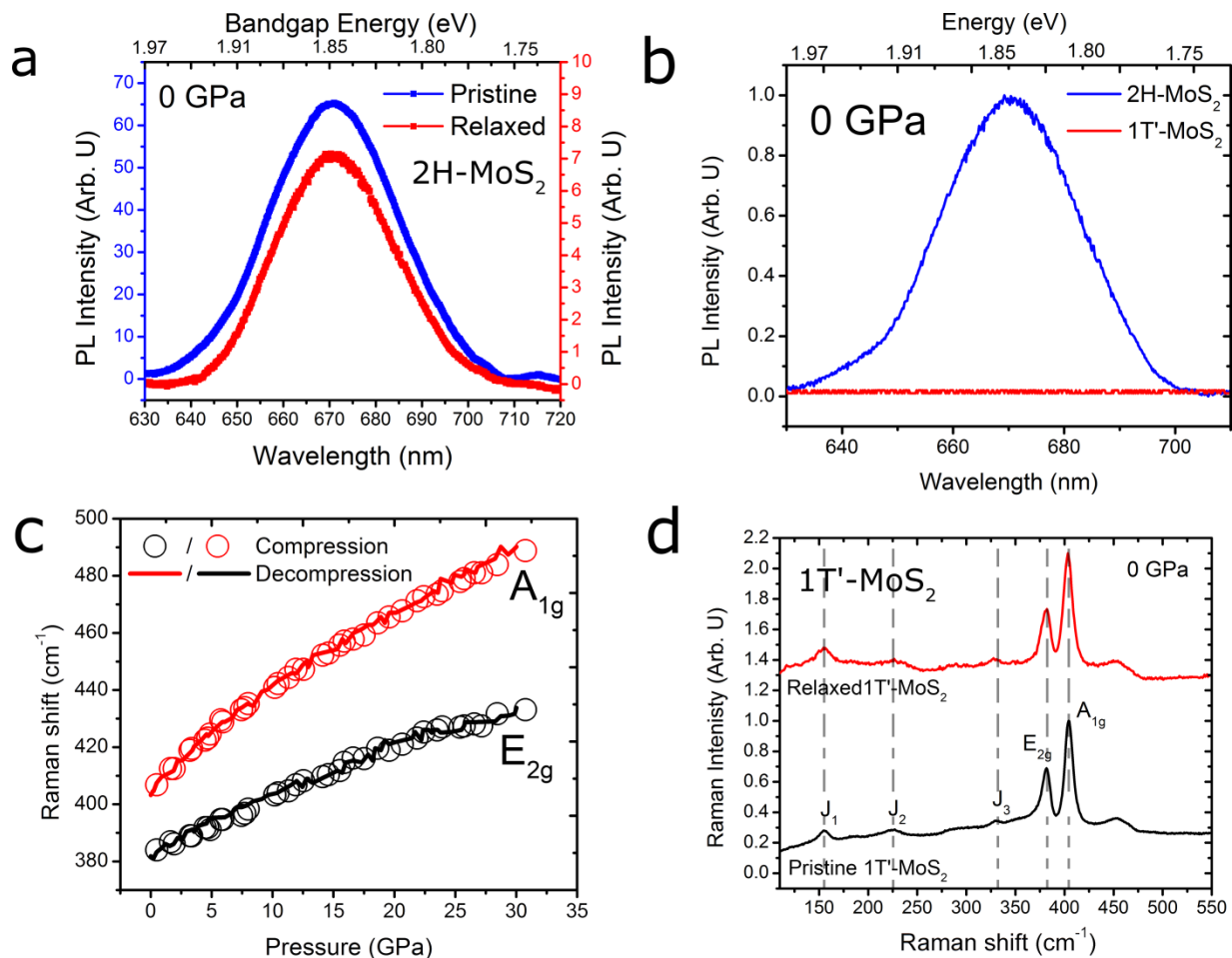


Figure 38. Reversible Pressure Effects on Monolayer MoS₂. (a) PL of from monolayer MoS₂ before and after hydrostatic pressure of 30 GPa is applied across the monolayer 2H-MoS₂. (b) The PL for the 1T'-MoS₂ and 2H-MoS₂ at 0 GPa. The 1T'-MoS₂ does not show PL behavior. (c) Upon decompression, the Raman active A_{1g} and E_{2g} modes compare well with the Raman spectra with increasing pressure, suggesting that the pressure effects are reversible. (d) Pristine and relaxed 1T'-MoS₂ show the J₁, J₂, and J₃ active modes, indicating that the pressure effects are reversible.

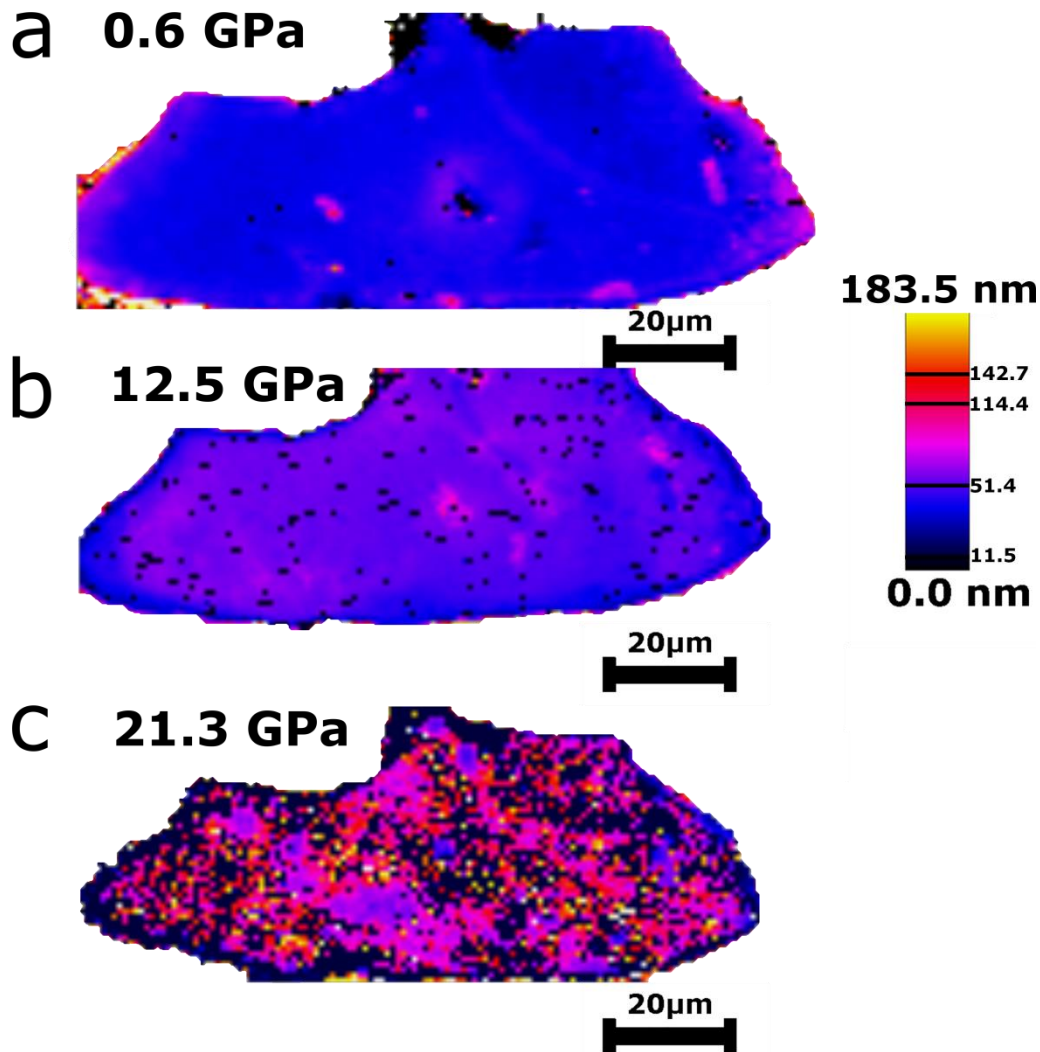


Figure 39. FWHM of the PL Spectra from Monolayer MoS₂. (a) The FWHM map showing an increase with hydrostatic pressure at 0.6 GPa (b) 12.5 GPa and (c) 21.3 GPa show the diminishing of the PL peak suggesting that the PL at high pressures is unresolvable past 16 GPa at room temperature. The black dots represent where the peaks are diminished into the background noise.

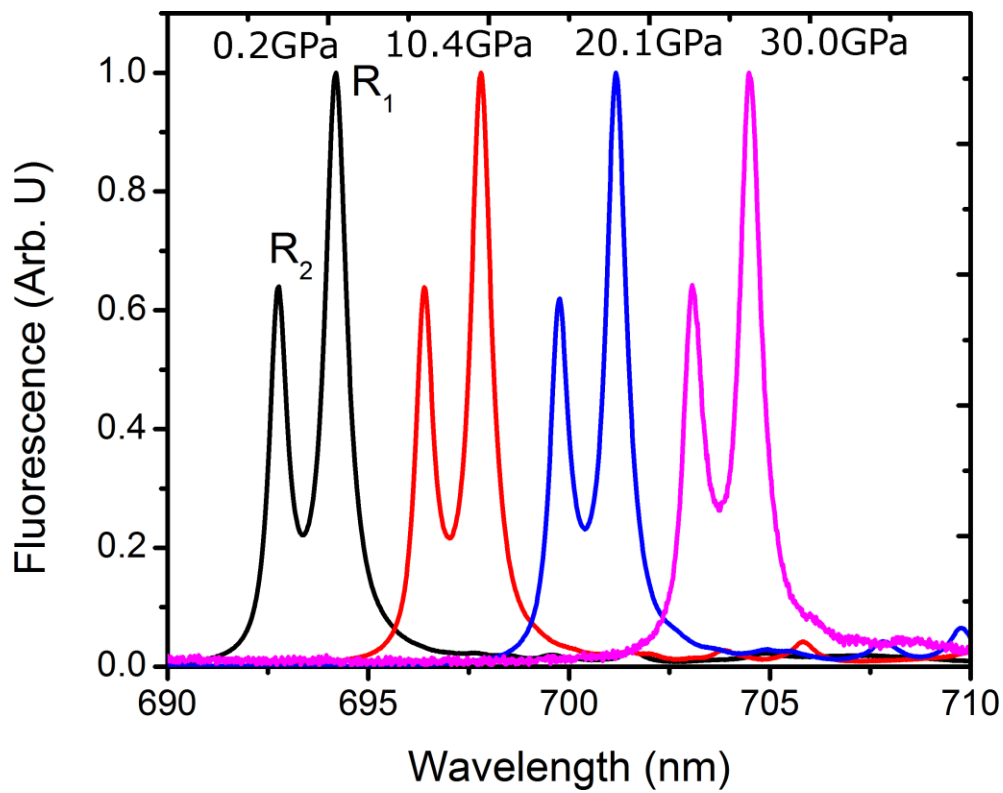


Figure 40. Fluorescence Spectra Shift in Ruby. The R₂ and R₁ ruby luminescence peaks are used to measure the pressure shift. The evolution of the PL spectra from ruby is used as a calibrant to measure the pressure experienced by the sample.

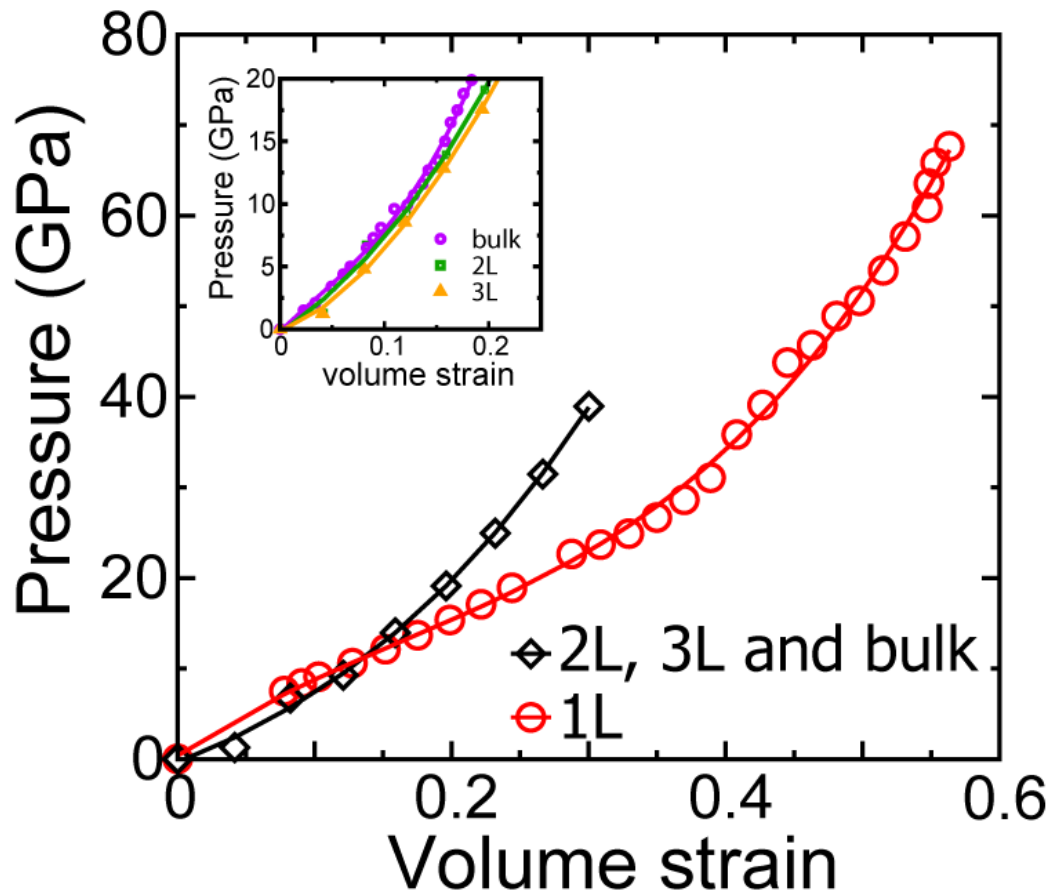


Figure 41. Relation between Volume Strain and Pressure for 2H-MoS₂ Family. 2L, 3L and Bulk Follow same trend and the data can be fitted to a third order polynomial gives as $P = -0.36 + 59.81\epsilon + 137.96\epsilon^2 + 325.93\epsilon^3$. However 1L depicts a completely different behavior, the polynomial fit of 1L data can be given as $P = 0.39 + 101.24\epsilon - 220.72\epsilon^2 + 446.7\epsilon^3$. These different behaviors arise due to absence of interlayer interaction for monolayer MoS₂. Inset: 2L, 3L and bulk have almost same dependence between volume strain and pressure.

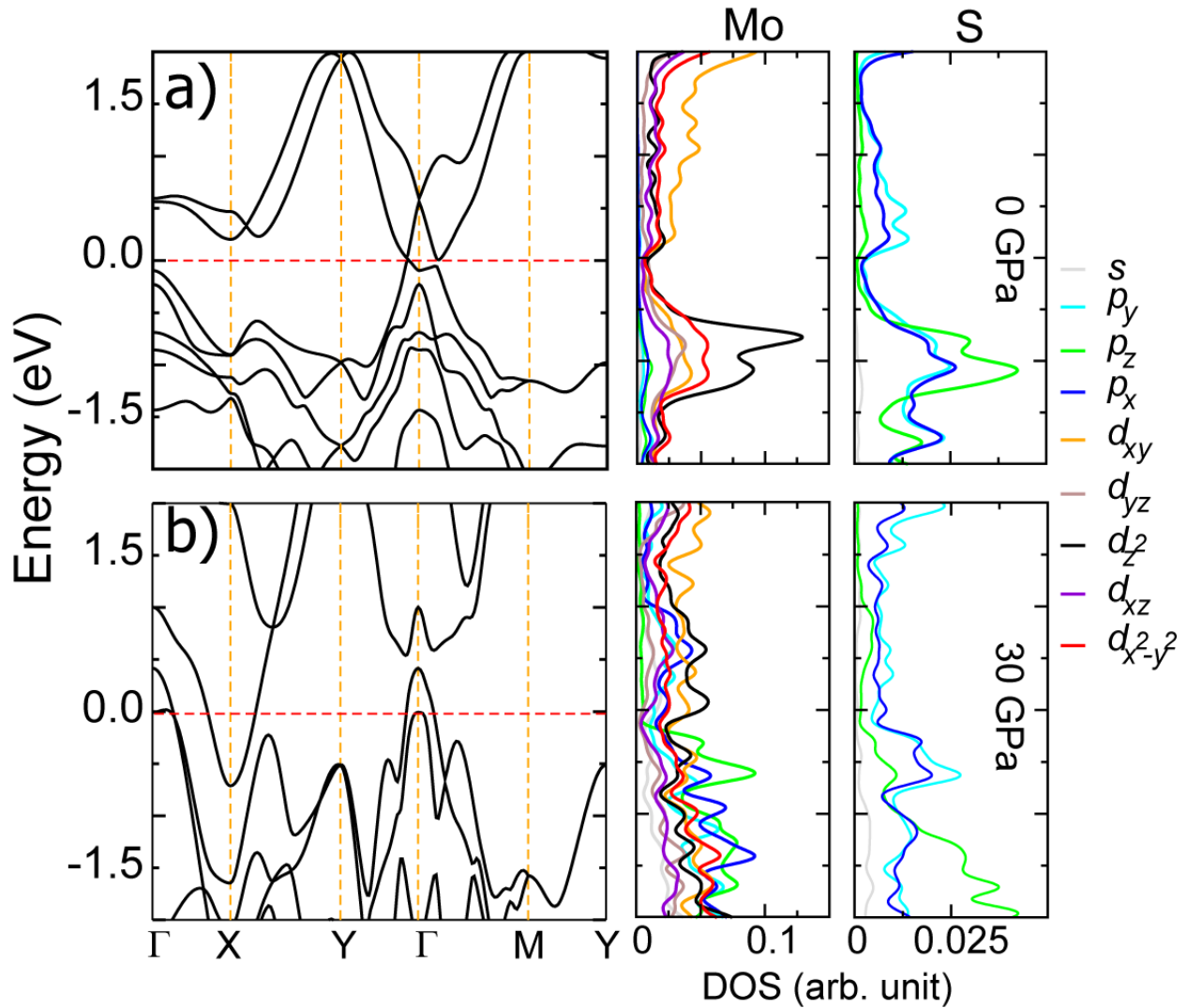


Figure 42. Band Structure and Density of States for the 1T'-MoS₂ Monolayer. (a) At 0 GPa pressure and (b) 30 GPa. The monolayer 1T'-MoS₂ is metallic and becomes more metallic under hydrostatic pressure. Upon application of hydrostatic pressure the hybridization between Mo *d*-orbitals (mainly d_z^2 , d_{xy} and $d_{x^2-y^2}$) and S *p*-orbitals increases, there is an increase in the overlap between conduction and valence bands, increasing the extent of metallization.

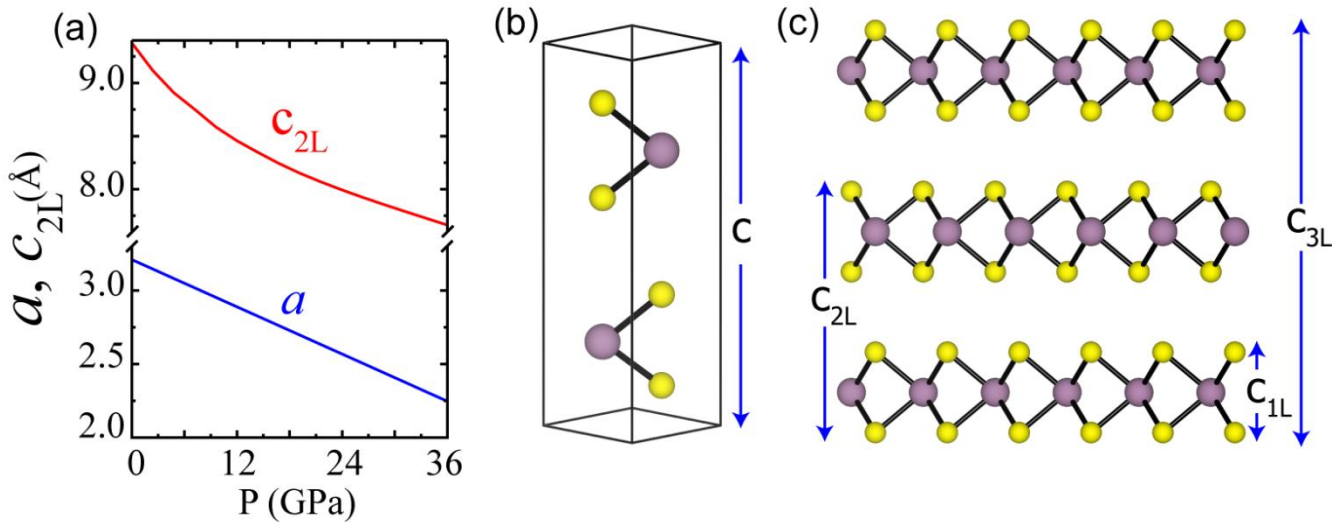


Figure 43. (a) Variation in slab thickness (c_{2L}) and in-plane lattice parameter a under hydrostatic pressure. Illustration of slab thickness for (b) bulk and (c) 1L, 2L and 3L MoS₂.

Pressure Based Large Doping and Metallization of Multilayered Tungsten Disulfide

Introduction

Due to the pronounced two-dimensional (2D) character of the transition-metal dichalcogenides (TMDs), interest in both the electronic and structural aspects of these materials have been garnered. These classes of TMDs possess a variety of electronic ground states, such as superconductivity,⁶² lattice deformation,⁶³ Mott transition,⁶⁴ and Anderson localization.⁶⁵ By changing the level of interaction in the multilayered TMDs, in our previous study, we have shown a isostructural semiconductor to metal (S-M) transition to occur.⁶³ Of these TMD materials, tungsten disulfide (WS_2) has attracted significant interest due to its unique structural,²⁰ optical,^{66,67} thermal⁶⁸ and electronic⁶⁹ properties. Unlike monolayer graphene which has sp^2 hybridization, multilayered semiconducting multilayered WS_2 has an indirect bandgap E_g of $\sim 1.3\text{eV}$. Similar to other TMDs, WS_2 is a layered TMD in the hexagonal crystal structure, in which tungsten has a trigonal prismatic coordination to sulfur and that strong in-plane covalent bonds exist between the transition metal (W) and two chalcogen (S) atoms while weak out-of-plane van der Waals forces (vdW) exists interstitially between layers. Since the out of plane atoms along the c -axis is interacting via weak vdW forces, shearing and compression is easier along this axis in comparison to the covalently bonded in-plane a -axis. This has therefore allowed for researchers to investigate WS_2 by means of mechanical exfoliation. Applying hydrostatic pressure allows for control over the vdW interlayer spacing and therefore allows for the modulation of electronic properties. Therefore, having control over the degree of disorder in crystalline materials can enable modulating electronic states in novel high gain optical switches,¹²⁷ sensing,¹²⁸ and mobility engineering.¹⁹

Experimentally, to modify the electronic properties of WS₂, several methods including intercalation,¹²⁹ layer confinement¹³⁰, chemical vapor growth,^{114,131,132} dual gating,¹⁹ and strain¹³³ have been adopted experimentally. The majority of the theoretical studies however, have concentrated their efforts on strain (i.e. uniaxial or biaxial strain) engineering electronic properties of WS₂,²⁰⁻²² allowing for better understanding on the strain-induced direct-to-indirect band gap (D-to-I) transition²³ as well as a S-M transition.^{21,24} Compared to these methods, applying hydrostatic pressure allows for dramatic changes in the structural and electronic properties.

Despite many theoretical studies²¹ suggesting metallization of multilayered WS₂, no experimental evidence for such a transition has surfaced until now. In this study, using a diamond anvil cell (DAC) apparatus (**Figure S1a**), we examine the gradual S-M transition of WS₂ up to ~35 GPa. With the six-order decrease in resistivity, the S-M transition metalizes at ~22 GPa at room temperature and a four order increase in carrier concentration is observed. Along with the experimental evidence, first-principle *ab-initio* theoretical calculations augment the experimental results to clearly understand the underlying physics responsible for the S-M transition and the increase in carrier concentration. This continuous tuning of the optical, structural, and electronic states provides a platform for developing pressure modulated electronics.

Results and Discussion

Electrical conductivity and electronic structures of WS₂

The electronic-transport measurements over the range of ~35 GPa reveals the tunability of the material properties of WS₂. Standard four-point probe *in situ* electrical resistivity measurements were conducted (**Figure S1b**). Under hydrostatic pressure, the measured electrical resistivity (ρ) shows a gradual decrease with increasing pressure and ultimately undergoes a metallization at pressure above 22 GPa (**Figure 24a**) at 280K. The resistivity profiles at different pressure are similar for various temperatures but vary in resistance values owing to the thermally activated carriers which are well understood from classical solid-state physics.¹³⁴ To find the semiconducting and metallic behavior of WS₂ at high pressures, the resistivity of the sample is measured with variation in temperature. The temperature-dependent resistivity profile shows that at low pressures (<22 GPa), a negative $d\rho/dT$ is observed, indicating the presence of a semiconducting state. At higher pressure (>22 GPa), a positive $d\rho/dT$ is observed suggesting a metallic state in multilayered WS₂ (**Figure 24b**). The transition pressure is inversely proportional to temperature due to lower thermal scattering at lower temperatures and is consistent with semiconducting and metallic behaviors.⁶³ Although we do not find evidence of a pressure induced superconducting state even at ~35 GPa at 2K, applying hydrostatic pressure onto multilayered WS₂ shows a six order magnitude decrease in the electrical resistivity from the semiconducting to metallic state.

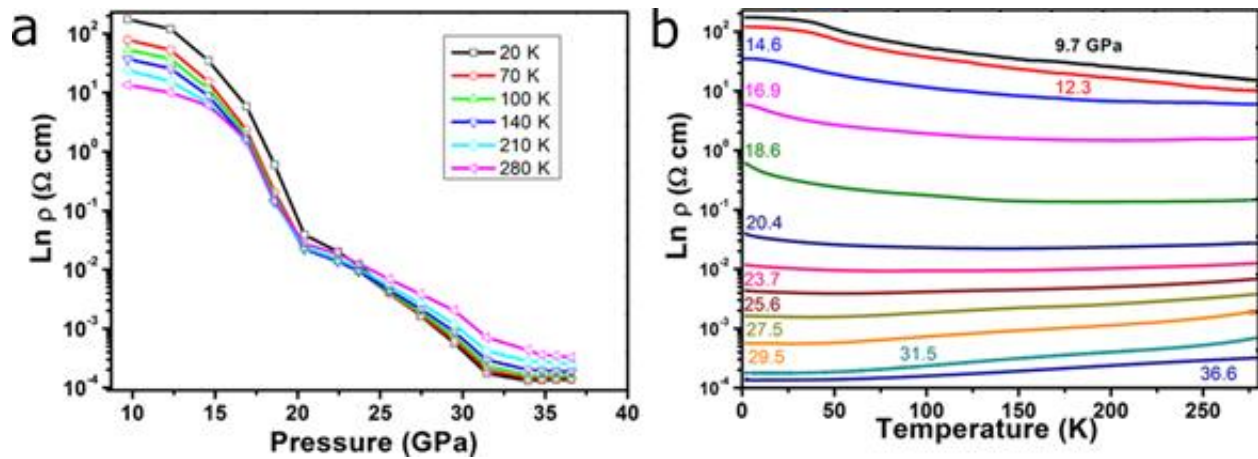


Figure 44. Pressure-induced metallization of the multilayered WS₂ in a diamond anvil cell. (a) Pressure-dependent resistivity (ρ) as function of pressure at selected temperatures shows a six order change in resistivity leading to the gradual metallization at higher pressures. (b) Temperature-dependent resistivity of the multilayered WS₂ at given high pressures shows a change in $d\rho/dT$ from negative to positive for the semiconducting to metallic state, respectively.

The pressure dependent resistivity profile at selected pressures and temperatures show the S-M transition to occur from a range of 23-28 GPa depending on the temperature (**Figure 25a**). The temperature-pressure contour shows the ρ evolution with pressure. The gradual six order resistivity decrease from $2 \times 10^2 \text{ } \Omega\text{cm}$ to $3 \times 10^{-4} \text{ } \Omega\text{cm}$ at 10 GPa and 36 GPa respectively. Unlike the abrupt drop in ρ for MoS₂ in our previous study,⁶³ gradual decrease in ρ is observed in WS₂ which suggests the tuning of the electronic structure and bandgap. To understand the S-M dependence on the transition metal (W or Mo), we compare the optical and electronics of WS₂ and MoS₂ (**Figure S2**). The band diagrams of bulk WS₂ and MoS₂ are similar and show an indirect bandgap of $\sim 1.3 \text{ eV}$ at ambient pressure. Experimentally, multilayered WS₂ metalizes at $\sim 22 \text{ GPa}$ in comparison to multilayered MoS₂ which metalizes at 19 GPa at room temperature. *In-situ* x-ray diffraction (XRD) shows the in-plane compression and out-of-plane compression for MoS₂ is more than WS₂ which infers that the pressure effects are more prominent on MoS₂ than WS₂. To further compare and contrast the behavior of WS₂ and MoS₂, we measure the pressure dependence ($\text{cm}^{-1}/\text{GPa}$), transition pressure, and the resistivity (ρ) in the semiconducting

and metallic region. Although the interlayer distance is relatively the same ($\sim 6.7\text{\AA}$), the difference in the elastic modulus of WS_2 (~ 354 GPa) in comparison to MoS_2 (~ 162 GPa) could be yet another reason for WS_2 to be more resilient to hydrostatic pressure in comparison to MoS_2 .¹³⁵

We measure the activation energy relation to pressure (**Figure 25b**) to be $E_t = 34.4 - 15e^{0.04P}$ where E_t is the thermal activation energy and P is pressure. The defect energy levels in the band gap are directly related to the activation energy and as the band gap closes, the activation energy nears zero. The good agreement between the activation energy and the metallization is suggestive of charge transport in WS_2 to be pressure activated. At pressures $P > 22$ GPa, we observe the variation in E_t to weaken. That can be explained by the fact that, at higher pressures, current transport is governed by localized states which is observed in the metallic region.

Theoretical calculations also reveal the closure of the multilayered WS_2 band gap decreasing with applied hydrostatic pressure (**Figure 25c**). Beyond 32 GPa, the valence band maxima (VBM) and the conduction band minima (CBM) cross the Fermi level indicating a complete metallization past this pressure point. With the increasing pressure, both the VBM and CBM shift their energy levels due to the increased interlayer electronic coupling, similar to that in MoS_2 particularly, since the VBM is contributed from the combination of both the antibonding p_z orbitals on S atoms and the d_{z^2} orbitals from W atoms, its energy level shifts significantly upwards upon pressure.¹³⁶ The CBM, which is also partially composed of the bonding p_z orbitals from S, shifts its energy downwards due to the increased overlap upon the decrease of the interlayer distance.

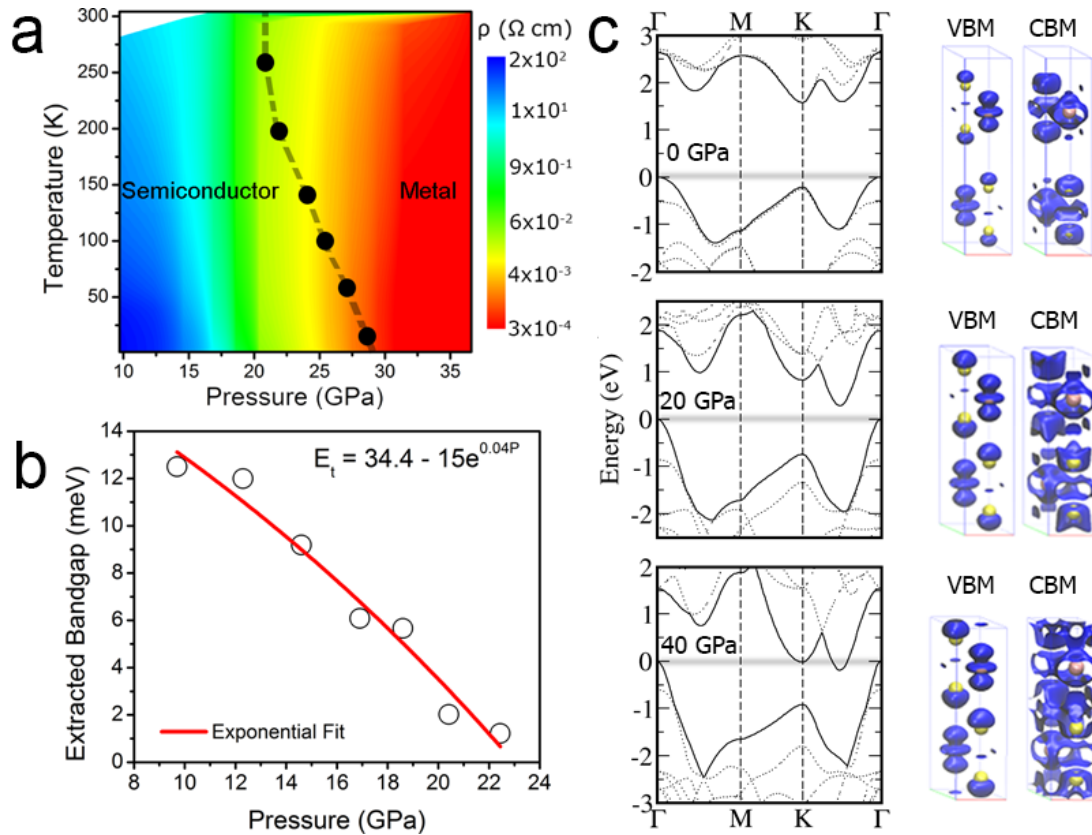


Figure 45. Metallization mechanism of the multilayered WS₂ as a function of hydrostatic pressure. (a) The temperature-pressure contour shows the transition region from the semiconductor to metallic region that is derived from experimental electrical conductivity measurements in a DAC. The dashed line is plotted to highlight the metallization P-T boundary as well as the overall negative slope of the transition. (b) The Arrhenius plot shows the activation energy exponentially decreases with pressure indicating a gradual metallization past ~22 GPa. Estimates of the semiconducting bandgap are obtained using $\ln R \propto E_g/2k_B T$ in the 50–100 K range. The value of the energy gap was derived from the resistance measurements decreased a lot with increasing of the pressure. (c) Band gap diagrams at M, K, and Γ point at three representative pressures of 0, 20.4, and 39.5 GPa from theoretical calculations depict the closing of the bandgap from 1.3 eV to 0 eV. At 39.5 GPa, the VBM and the CBM are shown to cross the Fermi level, suggesting a complete metallization. The increase in interactions between the orbitals are show with the increase in pressure.

We conducted Hall effect measurement with a magnetic field (H) perpendicular to a–b plane of the WS₂ single crystal and sweep the H at fixed temperatures (2 K, 130 K and 290 K) at selected pressures (**Figure S3**). From this, we find large Hall coefficients and resistivity of WS₂.¹³⁷ The carrier density increases with applied pressure (**Figure 26a**) shows a four order magnitude increase in carrier density compared to carrier density at room ambient pressure.¹²⁸ A gradual

increase in conductivity (**Figure 26b**) can be understood by the increase in interlayer interactions, and is consistent with our theoretical results and prior reports on multilayered MoS₂ with the increase in hydrostatic pressure.⁶³ The effect that structural disorder has on electron transport can be quantified by the resistivity ratio r_ρ , defined as ρ_{280K}/ρ_{2K} . The transition of the resistivity ratio r_ρ from values smaller than one to values larger than one is indicative of a transition from a semiconductor to a metal (**Figure 26c**). To evaluate the carrier mobility, we performed Hall measurements and find a decrease in carrier mobility from $\sim 90 \text{ cm}^2\text{V}^{-1}\text{s}^{-1}$ in the semiconducting region¹²⁸ to $\sim 60 \text{ cm}^2\text{V}^{-1}\text{s}^{-1}$ in the metallic region (**Figure 26d**). Recent reports on bilayer¹³⁸ and single-layer WS₂ gave an estimate of the mobility of charge carriers of $30 \text{ cm}^2\text{V}^{-1}\text{s}^{-1}$ and $4 \text{ cm}^2\text{V}^{-1}\text{s}^{-1}$ at room temperature respectively.¹²⁸ *Ab initio* calculations also shows the density of states increase with pressure and this increase in carrier density is associated with the $d_{x^2-y^2}$ orbital contributing significantly increase the carrier concentration in multilayered WS₂.

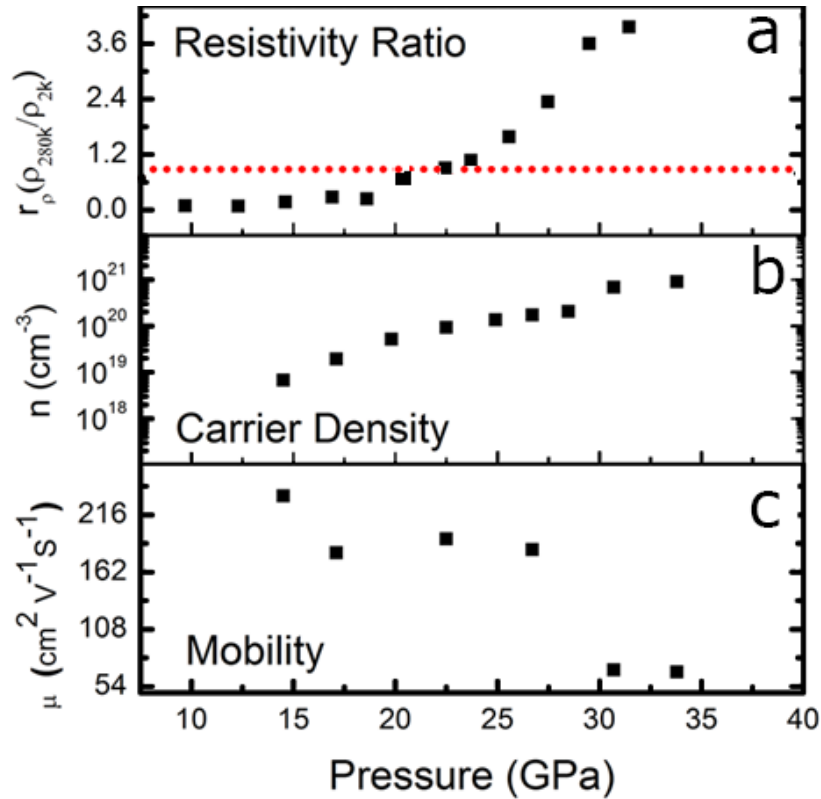


Figure 46. Electronic carrier dynamics of the multilayered WS₂ as a function of pressure. (a) The resistivity ratio (r_p) shows that above 22GPa, $r_p > 1$, which signifies a metallic state while at lower pressures, $r_p < 1$ is observed. (b) The carrier density increases by a factor of two in carrier concentration from 10^{19} cm^{-3} at 15 GPa to 10^{21} cm^{-3} at 35 GPa in the semiconductor and metallic region respectively. In comparison to the carrier density at 0 GPa, we observe a four order increase in magnitude.² (c) The mobility decreases by two orders of magnitude signifying more interlayer interaction. The mobility in the material decreases in the metallic state.

Optical and structural measurements of multilayered WS₂

Many of the electronic transitions are usually accompanied by crystal structural distortion or transformation. For many pressure induced structure phase transitions, *in-situ* XRD can be used to find the structure modification. For pressure induced isostructural phase transition however, the evidence of transition is not sensitive to XRD and *in situ* physical property measurement is used to determine this type of transition. Isostructural phase transition brings a new way to understand the mechanics and the driving forces of high-pressure phase transitions. In multilayered WS₂, we find that an isostructural transition exists since a sudden drop in volume is

not observed (**Figure 27a**). The pressure-volume relation is fit by a third-order Birch-Murnaghan (BM) EOS and no drastic discontinuity is observed (**Figure S4**). Although we do not observe a structural distortion up till 35 GPa, further increasing pressure could show layer sliding from the stable $2H_a$ phase to the $2H_c$ phase under high pressure.⁶¹

Another method to determine structural distortion is Raman spectroscopy. This has shown to be a powerful tool to determine information on the number of layers,¹³⁹ doping concentration,¹⁴⁰ and strain effect¹⁰ in TMDs. By studying the Raman pressure dependence, S-M transitions can be understood.^{63,23} Here we investigate the vibrational modes of WS_2 with varying pressure and temperature (**Figure 27b**). Selected pressure and temperature Raman profiles show phonon hardening as well as the E_{2g} mode being suppressed at high pressures which has also been observed in other TMDs (**Figure 27b**).^{30,63,141} Suppression of the intensity ratio between the A_{1g} and E_{2g} mode decreases with pressure (**Figure S5a**) and the E_{2g} mode suppressed is further evidenced by showing an increase in FWHM at higher pressures (**Figure S5b**). At higher temperatures, 2LA(M) mode is more prominent (**Figure 27b**) and the FWHM is observed to increase with temperature for all Raman modes (**Figure S5c**). The intensity ratio between the two Raman modes has also shown to decrease with increase in temperature (**Figure S5d**). At lower temperatures, there is overlap between the 2LA(M) and E_{2g} mode, and only one integral peak is observed. The temperature dependent Raman however indicates phonon softening (**Figure 27d**) at a rate of $0.02\text{cm}^{-1}/\text{K}$, $0.01\text{cm}^{-1}/\text{K}$ and $0.01\text{cm}^{-1}/\text{K}$ for all three 2LA(M), E_{2g} , and A_{1g} modes respectively. In comparison to the monolayer counterpart,¹⁴² an order of magnitude difference in the softening rate is observed in multilayered WS_2 . We attribute the difference to the double resonance scattering which is present only in monolayer WS_2 .¹³² The pressure

dependent Raman shows the A_{1g} mode being prominent at high pressures while the E_{2g} mode is suppressed (Figure 27c).

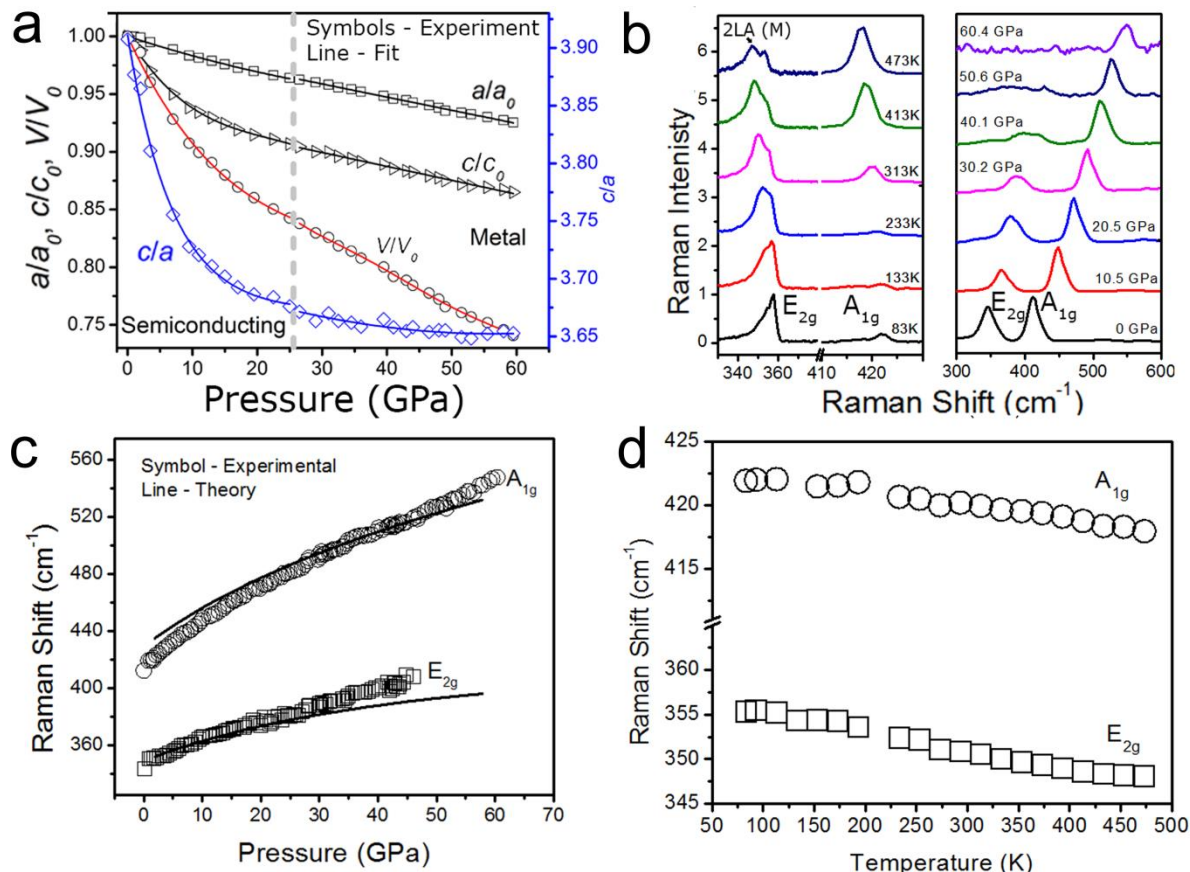


Figure 47. Optical and structural properties of the multilayered WS₂ under high pressure. (a) *In-situ* XRD shows that the sample remains in the hexagonal structure up to 60 GPa. The c axis is more compressible than the a axis at pressures below approximately 22 GPa and becomes much less compressible at pressures higher than 22 GPa where the metallization occurs. The dashed grey line shows the S-M transition pressure at ~22 GPa at 280K. (b) Raman profiles for selected temperatures and pressures. With increasing temperature, the A_{1g} mode becomes more prominent while the 2LA(M) is suppressed (left panel). Applied pressure suppressed the E_{2g} mode (right panel). (c) Pressure-dependent Raman map showing phonon hardening for both the E_{2g} and A_{1g} modes. The solid lines show the theoretical overlay which is in good agreement with observed experimental results. (d) Temperature-dependent Raman map indicating phonon softening from at a rate of $-0.02 \text{ cm}^{-1}/\text{K}$ and $-0.01 \text{ cm}^{-1}/\text{K}$ for the E_{2g} and A_{1g} modes respectively.

The temperature coefficient of single-layer WS₂ for both E_{2g} and A_{1g} mode are observed to be identical and is comparable to previous studies on other TMDs.¹⁴³ We find that the isostructural

S-M transition is heavily depended on hydrostatic pressure rather than on the temperature further highlighting the isostructural effects of hydrostatic pressure.

Conclusion

In conclusion, we study the electronic behavior of multilayered WS₂ under hydrostatic pressure. We find a metallization occurs at past ~22 GPa at 280K. To further understand this metallization, we conduct *ab-initio* calculations to reveal the underlying orbital contribution for the metallization. The change in slope in the temperature-resistivity characteristics as well as *in-situ* Raman spectroscopy showing the E_{2g} phonon softening are all evidence of metallization. Although, we observe metallic behavior past 35 GPa, further increasing pressure could increase interactions in the band structure perhaps resulting in superconducting and anomalous behavior.

Supplementary Figures

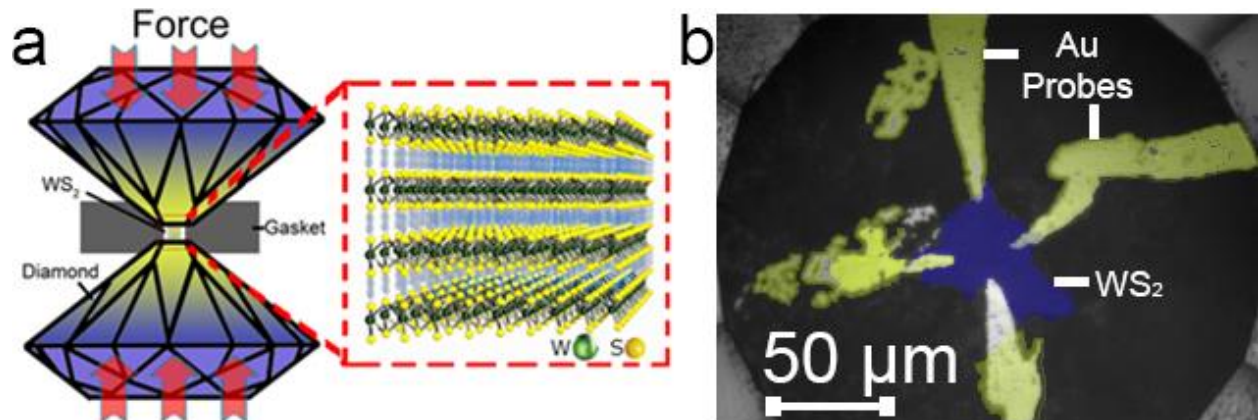


Figure 48. The diamond anvil cell setup. (a) Schematics of the diamond anvil cell is used for studying multilayered WS₂ at quasi-hydrostatic high-pressure conditions. The interlayer interactions (indicated by the blue glow) between the layers promote the metallization of WS₂. (b) Representative optical image of the WS₂ sample in a DAC at ~37 GPa. The multilayered WS₂ is connected to four gold electrical probes for measuring the electrical resistivity in a DAC and the diameter of the DAC surface is 300 μm.

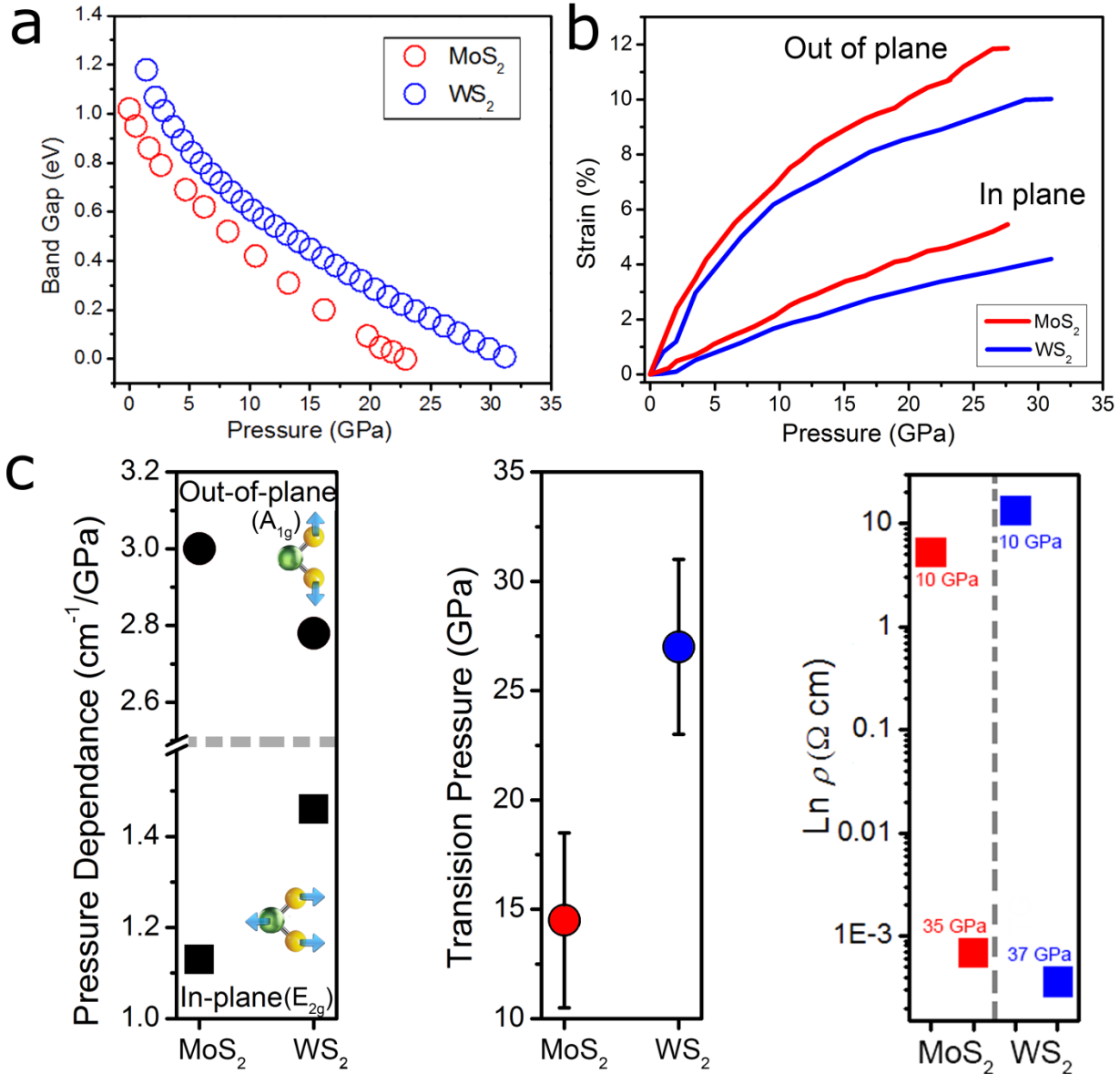


Figure 49. Comparison of high-pressure behavior of multilayered WS₂ and MoS₂. (a) Due to the pressure resilience of WS₂ in comparison to MoS₂, the theoretical bandgap with change in hydrostatic pressure of MoS₂ and WS₂ show the metallization of MoS₂ to occur at a faster rate (eV/GPa) than WS₂. (b) Larger out-of-plane (*c*-axis) strain is experienced in comparison to in-plane (*a*-axis) for both WS₂ and MoS₂. In comparison to WS₂, MoS₂ experiences more strain along the *a*-axis as well as the *c*-axis. (c) In-plane Raman pressure dependence (cm⁻¹/GPa) of WS₂ is smaller than MoS₂ suggesting that the W atom is more resistant to hydrostatic pressure. The transition pressure for a S-M transition for MoS₂ is lower than WS₂, but interestingly we do not observe as drastic of a drop in resistivity in WS₂. When comparing the resistivity values of MoS₂ and WS₂ at semiconductor (~10 GPa) and metallic (~36 GPa) regions, we observe a six order of magnitude drop in WS₂.

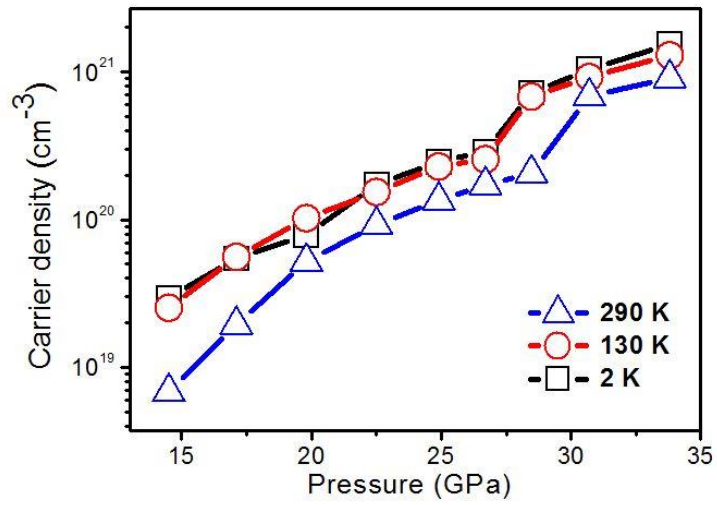


Figure 50. Carrier density variation with temperature and pressure. The carrier density increases by two orders of magnitude from ~15 GPa to ~35 GPa.

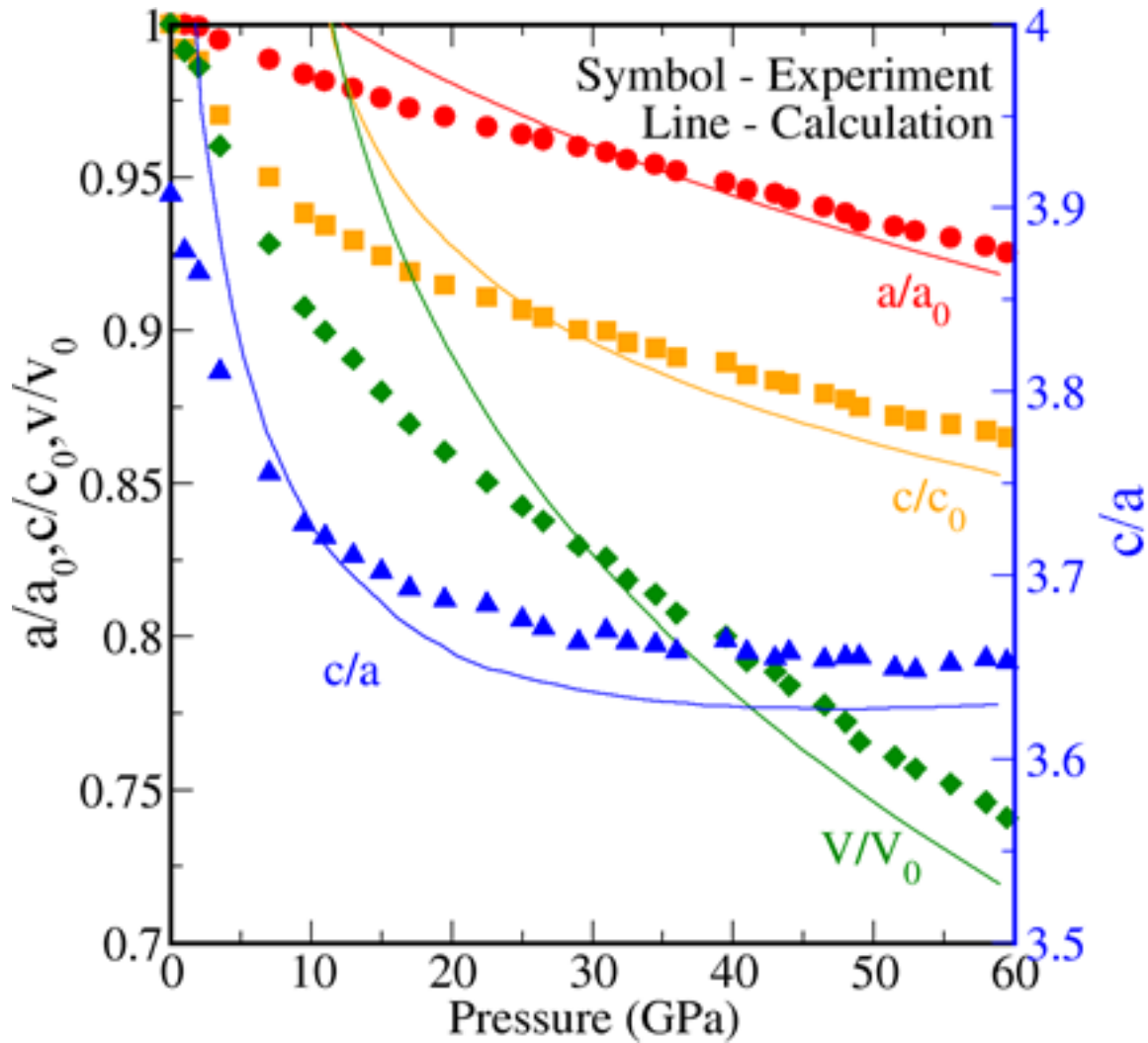


Figure 51. Lattice distortion with increase in hydrostatic pressure. Theoretical calculations agree with experimental results show distortion along the out-of-plane (c -axis) and in-plane (a -axis) axis. The c -axis is more compressible in comparison to the a -axis due to weak Van der Waals in-between layers.

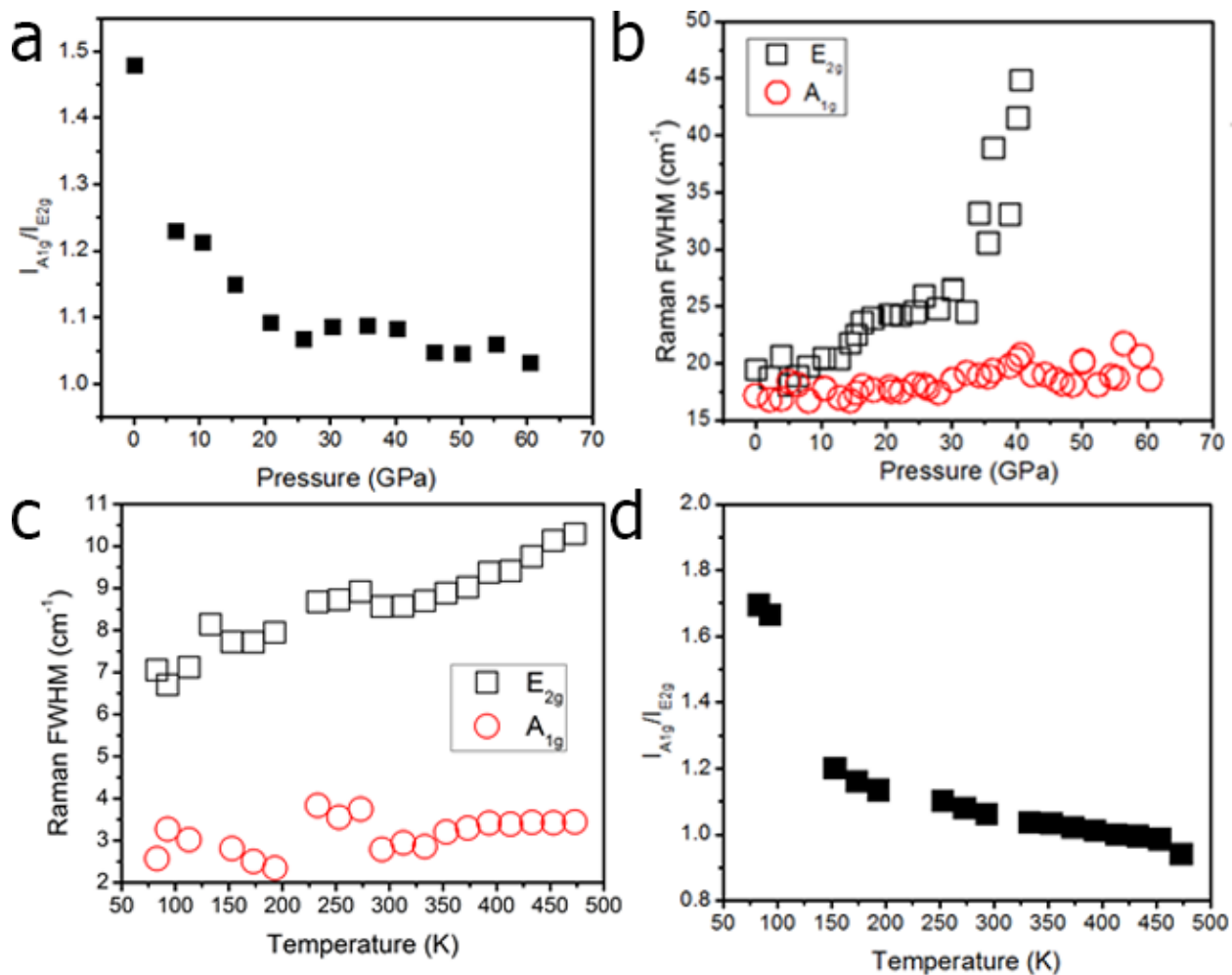


Figure 52. Raman full width half max, pressure and temperature dependence. (a) The pressure and (b) temperature dependence of the E_{2g} and A_{1g} Raman modes and the associated full width half max (FWHM). (c) The intensity ratio between the A_{1g} and E_{2g} peaks show the E_{2g} mode being repressed at higher pressures. (d) The intensity ratio between the A_{1g} and E_{2g} peak shows the A_{1g} peak decreasing at higher temperatures.

Chapter 3. Experimental Procedures and Setup

Acoustic Irradiation

The important factors to consider for reproducible results during the ultrasonication process are frequency and power of the acoustic waves, time of irradiation, solution temperature, type of solution, beaker diameter, ultrasonic probe tip/horn, and reaction environment. For the results stated, we find that using $90\text{W}\cdot\text{cm}^{-2}$ at 20kHz (an average of 130W), 60 minutes of irradiation (in a 200ml beaker with a 1 inch diameter), 1cm above the base of the beaker, at room ambient conditions in aqueous solution of 3.5mMol of h-BN platelets gives us >90% h-BN platelets that are dark. VCX 650X (with a horn tip diameter of 1.3cm) from Sonics and Materials was used to acoustically irradiate h-BN platelets (Momentive, PT110) with the specifications stated above (Figure 27).

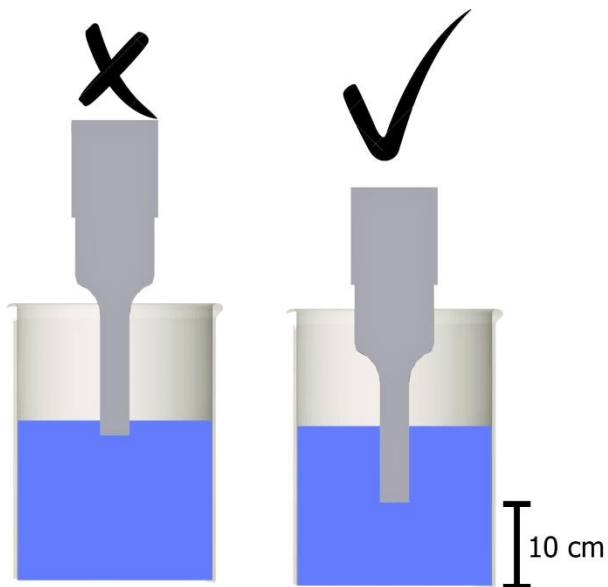
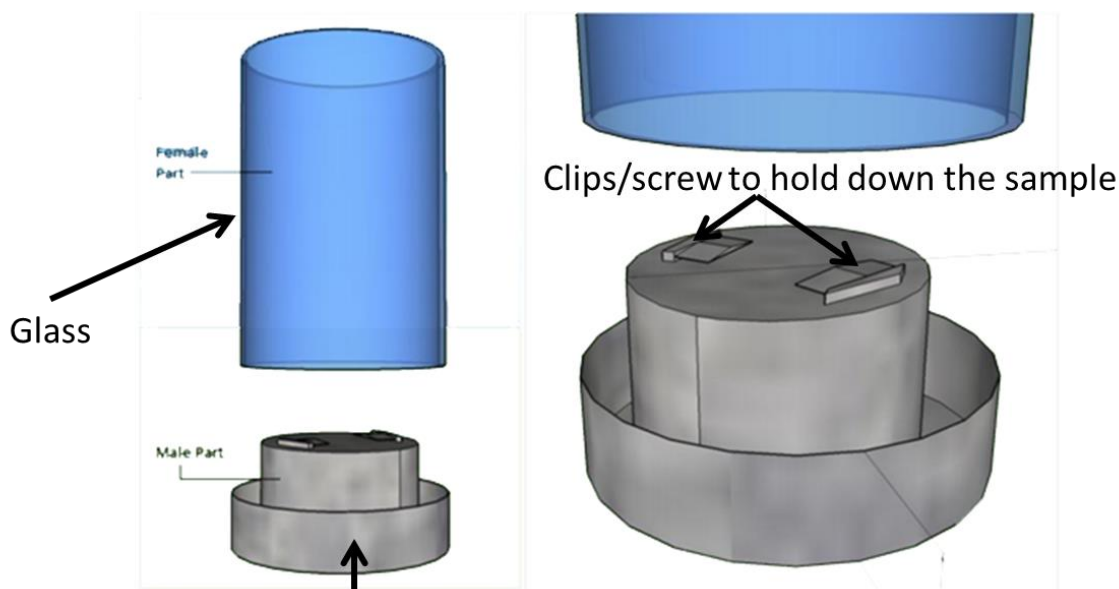


Figure 53. Horn position for ultrasonication irradiation. For optimal acoustic irradiation of h-BN, the horn tip needs to be 10 cm above the base of the 200ml beaker.

If direct deposition or growth on a substrate needs to be made, it's vital to include a substrate in situ ultrasonication irradiation. To stabilize the substrate in the beaker, a specific setup needs to

be built (**Figure 28**) which would ensure that the sample would not move while ultrasonication irradiation.



PTFE plastic (to avoid reacting with chemicals)

Figure 54. Designer ultrasonication chamber. This setup would allow for the stability of the sample while the ultrasonication irradiation is in progress.

All samples were imaged using a Quanta 650 FEG FE-SEM with Energy-dispersive X-ray spectroscopy (EDS) capability. Cary 5000 UV-VIS NIR Spectrometer was used to obtain the optical absorbance curves. The electrical measurements (Cascade B1500/Agilent 4156C semiconductor parameter analyzer) along with x-ray diffraction (XRD) (Philips X'Pert Pro X-ray system) were done at room ambient conditions. The SEM-EDS, XPS and TOF-SIMS measurements were performed in ultra-high vacuum (UHV) on h-BN platelets that were dispersed on a 40nm Au coated Si substrate. The acquisition time for each SEM-EDS profile was three minutes with the same working distance for all samples.

XPS spectra were recorded using a commercial x-ray photoelectron spectrometer (Kratos Axis Ultra, 2007). The detection angle of photoelectrons was normal to the sample surface and 45°

with respect to the X-ray beam ($\text{Al K}\alpha$; $h\nu = 1486.5\text{eV}$). The pressure in the analysis chamber was typically 4×10^{-9} Torr during data acquisition. Casa XPS analysis software was used for peak analysis. To reduce the oxide signals from the substrate, metal o-rings were used to cap the material (**Figure 29**).

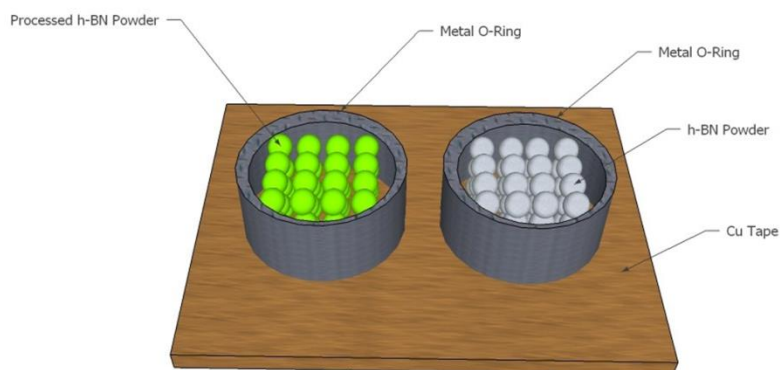


Figure 55. XPS sample preparation. To avoid oxide signals from the substrate, the samples (before and after processing) were placed directly on the o-ring such that the substrate did not play any effect on the sample signal.

Designed as a method to interrogate the outermost molecular (or atomic) layers (few Angstroms) of solid surfaces, Time-of-Flight Secondary Ion Mass Spectrometer (TOF-SIMS) not only determines the presence of chemical species at the surface but also divulges information regarding the chemical composition of the species being investigated. Absolute quantification of interesting species is not generally possible with TOF-SIMS due to variations in the secondary ion signal generated from the same species located in different matrices (i.e. chemical environments). However, relative quantification based on reference samples (i.e. samples that maintain as much as possible the matrix of the sample under investigation and contain the species of interest at TOF-SIMS detectable levels) is possible. Furthermore, if the interesting species in the reference sample have a known concentration one can determine their absolute concentration in other samples that have an identical or similar matrix. In our case, TOF-SIMS is

employed with the purpose of (1) detecting changes in chemical composition and (2) relative quantification of species of interest between the pristine and irradiated h-BN. An absolute determination of the interesting species' concentration is not important as we interrogate the relative chemical difference resulting from treating the h-BN flakes.

Sample Characterization

MoS₂ single crystals were purchased from SPI Supplies (CAS# 1317-33-5). The purity of the crystals was characterized and estimated to be greater than 99% by SPI supplies. The crystals were then thinned down to flakes of approximately 150 nm thick and 100 μm in length. Cross-section HR-TEM analyses of the sample flakes showed chemically and physically homogeneous layer surfaces at the nanometer scale. To understand the characteristics of the pristine as well as pressure-quenched samples (up to approximately 35 GPa and then quenched to ambient pressure), HR-TEM was used to analyze the lattice structures at the nanometer scale. Pristine MoS₂ was exfoliated onto a Cu TEM grid (SPI# 2040C-XA), while the quenched MoS₂ was transferred onto the Cu TEM grid using a micro tip-needle for HR-TEM analyses. The beam spot size was 5 nm in the TEM-EDX and an aperture size of 160 nm was used for the selected area electron diffraction (SAED). HR-TEM analyses of the recovered samples from DAC compression experiments show that their crystallinity and hexagonal lattice structure have not been altered drastically by compression and decompression in the diamond anvil cell.

For the sample characterization, it is vital to understand the effects of the probe tip that will be used to transfer the sample. While moving the sample from the diamond anvil culet to the target substrate, one must be aware of the contamination that the probe tip could have on the sample.

To avoid contamination, the sample must be “picked up” from the edge of the sample and not the area that will be characterized. Here are a few steps that need to be undertaken to avoid cross contamination (**Figure 30**).

Step	Details
1	Keep sample in a enclosed environment
2	The packaged sample needs to be kept in a vaccumm sealed chamber
3	10um edged tip needs to be scratched on diamond coated sand paper (2 minutes)
4	The tip should then be immersed in acetone and ultrasonicated (5 minutes)
5	Scratch the surface of the diamond anvil culet with sandpaper (until clean)
6	Clean the tip of the culet with the cotton earbuds to get rid of contaminants on the sufrage
7	Using the micro-tweezer, the sample needs to be picked up from the edge
8	Rubbing the side of the tip could help in creating static which could help pick up the sample
9	After the sample is placed on the diamond anvil culet, the tip should be re-cleaned (steps 3-4)

Figure 56. Procedure to avoid external contamination. The main causes of contamination are that the sample is exposed to air (i.e. not in a vacuum sealed container), the needle tip that is being used is not clean, and the target transfer substrate is not clean.

High-Pressure Electrical Resistance Measurements

Four-point probe electrical technique was employed to measure the electrical resistivity of the single-crystal multilayered MoS₂ as a function of pressure. Resistivity measurements as a function of temperature were also conducted in the semiconductor (SC), intermediate state (IS), and metallic state. A modified short symmetric DAC having a pair of anvil culets of 400 μm or 500 μm was used in two separate runs to ensure reproducibility. A rhenium gasket was pre-indented from a thickness of 250 μm to 40 μm at approximately 20 GPa, and a hole with a diameter of 200 μm was drilled in the center of the pre-indented area. Cubic BN (c-BN) fine powders were used as an insulating layer that was pressed into the pre-indented area and the drilled hole. Consequently, another hole of 100 μm in diameter was drilled at the center of the 200 μm hole filled with c-BN, which was then further filled with soft h-BN fine powders as the pressure transmitting medium while neon was used as the gas medium (**Figure 31**). A MoS₂

single crystal of 150 nm thick with dimensions of approximately $100\ \mu\text{m} \times 266\ \mu\text{m}$ was loaded into the sample chamber, together with three ruby spheres as the pressure calibrant and four Au electrodes with a length of $12.5\ \mu\text{m}$ for EC measurements. The resistivity of the sample was obtained by measuring the DC current changes in a pair of Au probes while sweeping DC voltages in another pair. The sample resistivity was derived by measuring the slope of the current-voltage (I-V) plot after taking the sample thickness into account.¹⁴⁴ For electrical measurements using the 4156C Agilent system, the firmware in built in the tool needs to be used to measure the I-V characteristics. The instructions on how to four-point probe a device can be read here ([link](#)). Quenched samples were further examined using cross-sectional SEM for potential dimensional changes of the samples to ensure reliable EC correction. For the opto-electronic measurements under high pressure, a green laser with 532 nm wavelength (2.3 eV) was focused down to a $10\ \mu\text{m} \times 10\ \mu\text{m}$ window to ensure that the laser was exclusively on the sample.

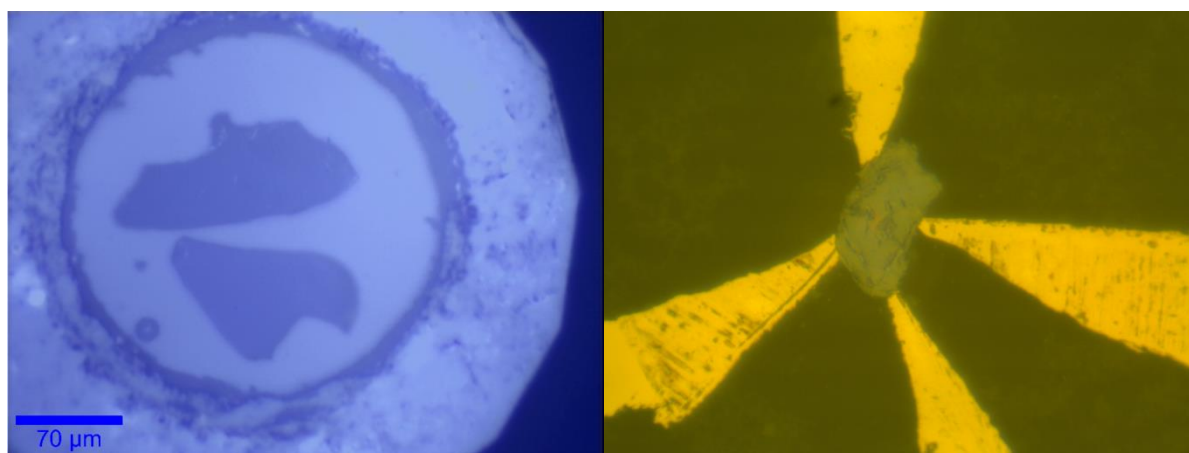


Figure 57. Sample loading in a DAC. (a) Two samples gas loaded in a DAC with the ruby which can be probed using optical spectroscopy. **(b)** One sample c-BN loaded in DAC with four probes connected for electrical resistivity measurements.

High-Pressure Laser Raman Spectroscopy

Raman spectra were measured using a green 532 nm Coherent Verdi V2 laser. The scattered light was dispersed by a 1800 grooves/mm grating and collected by an EMCCD (Andor Technology) resulting in a spectral resolution of approximately 1 cm^{-1} . The highest laser power level of 4 mW with a focused laser beam size of $10 \text{ }\mu\text{m}$ was used for the measurements to avoid potential over-heating or oxidation of the samples. Ruby fluorescence spectra were also collected using the same system for pressure calibrations; pressures and their uncertainties were determined from multiple measurements of the ruby spheres close to the sample in the sample chamber of the DAC before and after each Raman measurement.

Only the short-symmetric diamond anvil cell can be used with the Witec Alpha 300 micro-Raman confocal microscope (488 nm laser) system. The limitation to the setup is the 20x large working distance objective microscope which cannot resolve anything past the 20x limit. Care needs to be taken to place the DAC below the objective such that the DAC does not come in contact with the microscope. The final setup to measure the Raman while under high pressure in the DAC should have both the objective and the DAC not in contact (**Figure 32**).

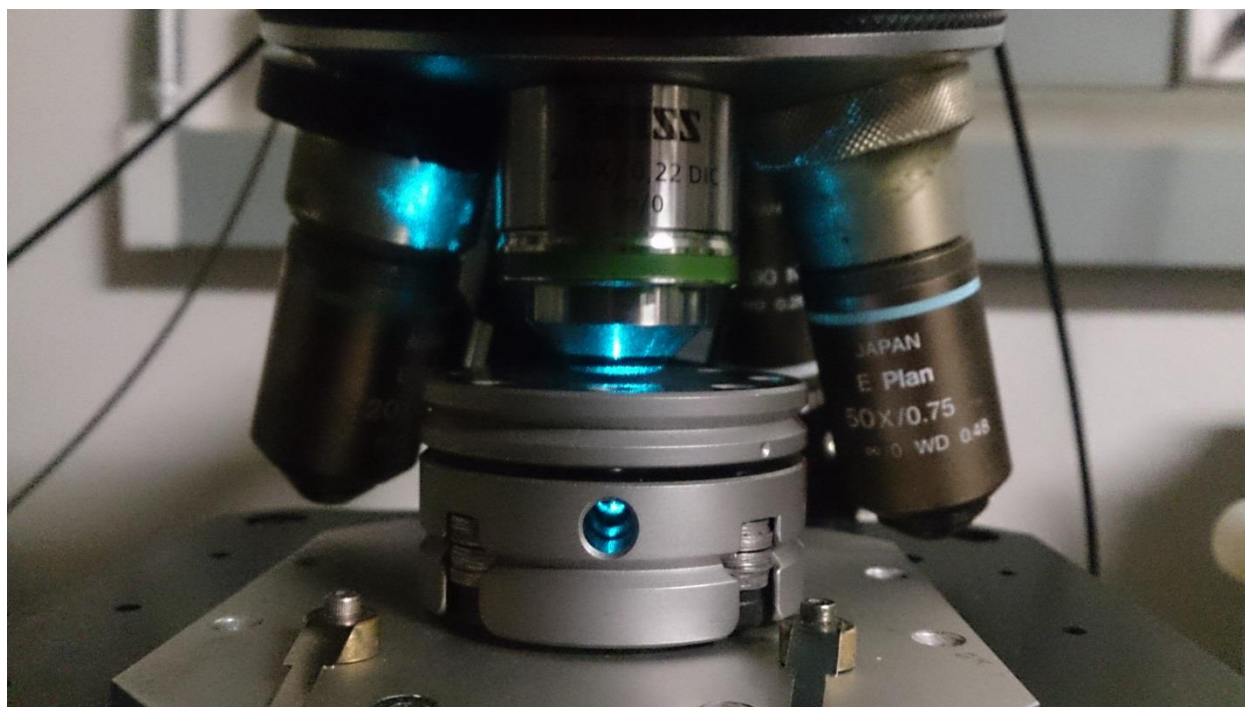


Figure 58. Setup for measuring Raman under high pressure. The completed configuration of the DAC and the objective microscope for Raman spectroscopy under high pressure.

Chapter 4. Conclusions

Partially Oxidized Hexagonal Boron Nitride

It is evident from the research that 2D materials can change their properties when exposed to high pressure environments. Notably, we have observed that optical and electronic properties of h-BN considerably change when exposed to shock treatments of heat and pressure by nonlinear acoustic waves and imposition of cavitation bubbles. This exposure to rapid heat and pressure causes a ~60% decrease in transmission (**Figure 6b-c**) showing the color change in h-BN from white to dark. A threefold increase in conductivity is also observed in PO-hBN. Due to the partial oxidization of h-BN (PO-hBN), optical measurements show that the band gap shifts from 5.5eV to 3.9eV (**Figure 6d**). While the vibrational properties remain the same in h-BN in comparison to PO-hBN (**Figure 8b**), notable shifts in the XPS and a β -B₂O₃ XRD peak indicate the surface modification of h-BN (**Figure 8a/c**). To further delve into this surface modification, ToF-SIMS was employed to measure the B⁺, BO⁺ and OH⁺ ions present on the surface of PO-hBN (**Figure 10c**). A ToF-SIMS depth profile (**Figure 10d-f**) also shows that the concentrations of BO⁺ and OH⁺ ions decrease with depth indicating that the optical and electrical changes are caused due to the surface modification of h-BN.

Pressure-Induced Semiconducting to Metallic Transition in Multilayered MoS₂

We find that a semiconductor to metal transition occurs in MoS₂ when subjected to extreme pressures inside of a diamond anvil cell. When inducing a quasi-hydrostatic pressure onto a material, changes in the vibrational properties as well as its electronic properties are studied. A

clear indication of a semiconductor to metal transition is observed at 19GPa (**Figure 13c-d**). Furthermore, a FWHM drop is observed indicating a semiconducting to metallic transition (**Figure 15d**). Adept understanding of this transition extends itself for theoretical charge density calculations (**Figure 14a-d**). The accumulation and depletion of charges observed between the out-of-plane S-S interactions show that the majority of the carrier concentration is due to the interactions between layers and not in-plane. In support of this, optical vibrations suggest that E_{2g} out of plane intensity diminish with pressure while the in-plane A_{1g} mode does not vary drastically in intensity (**Figure 15a-c**). The energy between the conduction and valance band tend to decrease with pressure therefore causing the band gap to decrease. This change in band gap is estimated theoretically (**Figure 16a**) and the current gain (I_{on}/I_{off} ratio) is measured experimentally to allude to the overlap of the conduction and valance bands at 19GPa. To determine whether this is a structural change as well as an electronic transition, *in situ* XRD was conducted to determine that no crystal structure transformation was observed (**Figure 17a-b**), therefore making it a iso-structural transition.

Pressure-Dependent Optical and Vibrational Properties of Monolayer MoS₂

Controlling the band gap by tuning the lattice structure through pressure engineering is a relatively new route for tailoring the optoelectronic properties of two dimensional (2D) materials. Here we investigate the electronic and lattice vibrational dynamics of the distorted monolayer 1T-MoS₂ (1T') and the monolayer 2H-MoS₂ *via* a diamond anvil cell (DAC) and density functional theory (DFT) calculations. The direct optical band gap of the monolayer 2H-MoS₂ increases by 11.7% from 1.85 eV to 2.08 eV, which is the highest reported for a 2D transition metal dichalcogenide (TMD) material. DFT calculations reveal a subsequent decrease in the band gap with eventual metallization of the monolayer 2H-MoS₂, an overall complex

structure-property relation due to the rich band structure of MoS₂. Remarkably, the metastable 1T'-MoS₂ metallic state remains invariant with pressure, with the J₂, A_{1g}, and E_{2g} modes becoming dominant at high pressures. This substantial reversible tunability of the electronic and vibrational property of the MoS₂ family can be extended to other 2D TMDs. These results present an important advance toward controlling the band structure and optoelectronic properties of monolayer MoS₂ via pressure, which has vital implications for enhanced device applications.

Pressure Based Large Doping and Metallization of Multilayered WS₂

Tungsten disulphide (WS₂) is a layered transition metal dichalcogenide (TMD) which differs from other two-dimensional compounds such graphene due to its unique semiconducting properties. Uniaxial and biaxial strain engineering on TMDs has allowed for fine tuning their electronic properties for the purpose of optimal device implications, while applying hydrostatic pressure at higher strains has recently elucidated intriguing electronic and optical behaviors such as metallization, bandgap opening, as well as direct-indirect bandgap transition especially for monolayered and multilayered TMDs. Thus far, the electronic properties of multilayered WS₂ at high-strain conditions (i.e. strain rates > 12%) remains elusive. Here we have studied the structural, electronic, and vibrational properties of multilayered WS₂ at hydrostatic pressures up to ~35 GPa experimentally in a diamond anvil cell and theoretically using first-principles *ab-initio* calculations. WS₂ undergoes an isostructural semiconductor-metal (S-M) transition at approximately 22 GPa at 280K, which arises from the overlap of the highest valance and lowest conduction bands. The S-M transition is caused by increased sulfur–sulfur interactions as the interlayer spacing reduces with applied hydrostatic pressure. Changes in the electronic structures across the metallization transition are shown to contribute to unprecedented changes in charge carrier characteristics including a six-order decrease in resistivity, two-order decrease in mobility, and a four-order increase in carrier concentration. These changes in electronic properties are the highest reported to our knowledge. These results show that pressure-tuned electronic and optical properties of multilayered WS₂ can enable novel pressure tunable electronics.

Chapter 5. Implications and Opportunities

High pressure research has allowed for an abundance of new physics to be understood. The majority of high pressure physics research however, is conducted by geologists studying the earth interior. This allows for new opportunities from different regions of academia to study the electrical and material properties under high pressure. Recently, due to the advent of 2D materials, significant interest has emerged in modifying their material properties. Very few studies have been conducted on the hydrostatic pressure on 2D materials and therefore leave a lot of room for exciting opportunities and challenges to be undertaken. Some of the interesting properties that can be explored are phonon splitting (as seen in WSe_2) and merging (as seen in $1\text{T}'\text{-WS}_2$) in materials which have overlapping Raman frequencies at ambient pressure.

Although challenging, probing 2D materials under high pressure allows for a varied range of physics to be explored including superconductivity, spin-transitions, and metal-to-semiconductor (bandgap opening) transition, and semiconductor-to-metal (bandgap closing) transition to electrically probed. The I-V characteristics of these materials under high pressure could lead to space-charge limited transport due to the diamond-material interface. Furthermore, since hydrostatic pressure alters the band structure, the capacitance can also be measured by conducting C-V measurements.

Due to the stacking structure of the 2D materials, a new class of hybrid structures can be probed by optical measurements. This opens up opportunity in artificially engineering a new class of materials by applying hydrostatic pressure onto bilayer materials. By decreasing the interlayer distance and increasing interaction between the two layers, a new two-dimensional simple cubic or wurtzite structures could be formed. Using ultrafast laser spectroscopy (ps to fs laser pulses)

can also allow for thermal and phonon decay of these materials to be studied under high pressure.

Applying pressure as well as temperature onto 2D materials can also lead to phase diagrams to be developed which would widely vary from the bulk counterpart. High pressure physics can also be used to cause permanent changes to materials that could allow for new materials to be used at ambient conditions (as seen in black phosphor). Due to the surface of topological insulators containing conducting states, similar 2D material properties have been observed in these materials. Applying high pressure to these topological insulators could allow for superconducting states to be tapped (as seen in Sb_2Te_3).²⁹

Research on high pressure physics on 2D materials is only at its elementary stage. Applying pressure onto these 2D materials can open up new avenues for applications that have not yet been explored.

List of Publications

A. P. Nayak, A. Dolocan, J. Lee, H-Y Chang, T. Pandhi, M. Holt, L. Tao, and D. Akinwande, *Inversion of the Electrical and Optical Properties of Partially Oxidized Hexagonal Boron Nitride*, Nano, World Scientific, October 2013, DOI: 10.1142/S1793292014500027 ([link](#))

A. P. Nayak, S. Bhattacharyya, J. Zhu, J. Liu, X. Wu, T. Pandey, C. Jin, A. K. Singh, D. Akinwande, J. F. Lin, *Pressure-Induced Electronic Transition in Multilayered Molybdenum Disulfide*, Nature Communications, May 2014. DOI: 10.1038/ncomms4731 ([link](#))

A. P. Nayak, T Pandey, D Voiry, J Liu, ST Moran, A Sharma, C Tan, CH Chen, LJ Li, M Chhowalla, JF Lin, AK Singh, D Akinwande. *Pressure-Dependent Optical and Vibrational Properties of Monolayer Molybdenum Disulfide*, December 2014. DOI: 10.1021/nl5036397 ([link](#))

Presentations and Conferences

A. P. Nayak, D. Koh, and D. Akiwnande, “Thickness Dependence of Electrical Breakdown in h-BN dielectric using C-AFM microscopy”, APS Meeting, Mar. 2012.

A. P. Nayak, “Pressure Induced structure-property tuning of Two Dimensional Materials”, SemiTech, March. 2015.

A. P. Nayak, S. Bhattacharyya, J. Zhu, J. Liu, X. Wu, T. Pandey, C. Jin, A K. Singh, D. Akinwande, J-F Lin. "Pressure-induced semiconducting to metallic transition in multilayered molybdenum disulphide" **Invited**. EFree Conference. Washington DC. 2013

A. P. Nayak, J. Zhu, J-F Lin, D. Akinwande. "Tuning the electrical and optical properties of MoS₂ under high pressure." Thermec conference. Las Vegas, Nevada 2013.

A. P. Nayak, J. Zhu, J-Fu Lin, D. Akinwande. "Optical Bandgap tuning of MoS₂ under High Pressure" APS conference. Seattle, Washington. 2013.

A. P. Nayak, J. Liu, C. Tan , X. Wang , T. Pandhi , L. Tao, J-Fu Lin, D. Akinwande. "Physics of monolayer and bilayer graphene" Deep Carbon Observatory Conference. Los Angeles, California, 2014.

A. P. Nayak, T. Pandey, D. Voiry, J. Liu, S. Moran, A. Sharma, C. Tan, C-H Chen, L-J Li, M. Chhowalla, J-Fu Lin, A.K. Singh, D. Akinwande "Pressure-Dependent Optical and Vibrational Properties of Monolayer Molybdenum Disulfide" APS. San Antonio, Texas. 2015.

References

- 1 Wang, H., Yuan, H., Sae Hong, S., Li, Y. & Cui, Y. Physical and chemical tuning of two-dimensional transition metal dichalcogenides. *Chemical Society Reviews*, doi:10.1039/C4CS00287C (2015).
- 2 Matthes, T. W. *et al.* Imaging of dopants in surface and sub-surface layers of the transition metal dichalcogenides WS₂ and WSe₂ by scanning tunneling microscopy. *Appl Phys A* **66**, 1007-1011, doi:10.1007/PL00022813 (1998).
- 3 Avila, A. G. & Hinstroza, J. P. Smart textiles: Tough cotton. *Nat Nano* **3**, 458-459 (2008).
- 4 Kostoff, R., Koytcheff, R. & Lau, C. Y. Structure of the nanoscience and nanotechnology applications literature. *J Technol Transfer* **33**, 472-484, doi:10.1007/s10961-007-9042-2 (2008).
- 5 Michel, K. H. & Verberck, B. Theory of elastic and piezoelectric effects in two-dimensional hexagonal boron nitride. *Physical Review B* **80**, 224301 (2009).
- 6 Geim, A. K. & Novoselov, K. S. The rise of graphene. *Nat Mater* **6**, 183-191 (2007).
- 7 Peng, Q. & De, S. Outstanding mechanical properties of monolayer MoS₂ and its application in elastic energy storage. *Physical Chemistry Chemical Physics* **15**, 19427-19437, doi:10.1039/C3CP52879K (2013).
- 8 Choi, W. *et al.* High-Detectivity Multilayer MoS₂ Phototransistors with Spectral Response from Ultraviolet to Infrared. *Advanced Materials* **24**, 5832-5836, doi:10.1002/adma.201201909 (2012).

- 9 Lee, J., Tao, L., Hao, Y., Ruoff, R. S. & Akinwande, D. Embedded-gate graphene transistors for high-mobility detachable flexible nanoelectronics. *Applied Physics Letters* **100**, 152104-152104 (2012).
- 10 Akinwande, D., Petrone, N. & Hone, J. Two-dimensional flexible nanoelectronics. *Nat Commun* **5**, doi:10.1038/ncomms6678 (2014).
- 11 Mermin, N. D. & Wagner, H. Absence of Ferromagnetism or Antiferromagnetism in One- or Two-Dimensional Isotropic Heisenberg Models. *Physical Review Letters* **17**, 1133-1136 (1966).
- 12 Klein, A., Landau, L. & Shucker, D. On the absence of spontaneous breakdown of continuous symmetry for equilibrium states in two dimensions. *J Stat Phys* **26**, 505-512, doi:10.1007/BF01011431 (1981).
- 13 Ohring, M. *The Materials Science of Thin Films*. (Academic Press, 1992).
- 14 Goswami, A. *Thin Film Fundamentals*. (New Age International Pub, 1996).
- 15 Novoselov, K. S. *et al.* Electric Field Effect in Atomically Thin Carbon Films. *Science* **306**, 666-669, doi:10.1126/science.1102896 (2004).
- 16 Song, L. *et al.* Large Scale Growth and Characterization of Atomic Hexagonal Boron Nitride Layers. *Nano Letters* **10**, 3209-3215, doi:10.1021/nl1022139 (2010).
- 17 Liu, Z. *et al.* Direct Growth of Graphene/Hexagonal Boron Nitride Stacked Layers. *Nano Letters* **11**, 2032-2037, doi:10.1021/nl200464j (2011).
- 18 Guo, H., Yang, T., Tao, P., Wang, Y. & Zhang, Z. High pressure effect on structure, electronic structure, and thermoelectric properties of MoS₂. *Journal of Applied Physics* **113**, - (2013).

- 19 Radisavljevic, B. & Kis, A. Mobility engineering and a metal–insulator transition in monolayer MoS₂. *Nat Mater* **12**, 815-820, doi:10.1038/nmat3687 (2013).
- 20 Duerloo, K.-A. N., Li, Y. & Reed, E. J. Structural phase transitions in two-dimensional Mo- and W-dichalcogenide monolayers. *Nat Commun* **5**, doi:10.1038/ncomms5214 (2014).
- 21 Bhattacharyya, S. & Singh, A. K. Semiconductor-metal transition in semiconducting bilayer sheets of transition-metal dichalcogenides. *Physical Review B* **86**, 075454 (2012).
- 22 Amin, B., Kaloni, T. P. & Schwingenschlogl, U. Strain engineering of WS₂, WSe₂, and WTe₂. *RSC Advances* **4**, 34561-34565, doi:10.1039/C4RA06378C (2014).
- 23 Nayak, A. P. *et al.* Pressure-Dependent Optical and Vibrational Properties of Monolayer Molybdenum Disulfide. *Nano Letters*, doi:10.1021/nl5036397 (2014).
- 24 Scalise, E., Houssa, M., Pourtois, G., Afanas'ev, V. & Stesmans, A. Strain-induced semiconductor to metal transition in the two-dimensional honeycomb structure of MoS₂. *Nano Res.* **5**, 43-48, doi:10.1007/s12274-011-0183-0 (2012).
- 25 Mason, T. J. & Peters, D. *Practical sonochemistry: Power ultrasound uses and applications*. (Horwood Publishing Limited, 2004).
- 26 Weir, C. E. Infrared studies in the 1-to 15-micron region to 30,000 atmospheres. *Journal of research of the National Bureau of Standards. Section A. Physics and chemistry* **63**, 55 (1959).
- 27 Dubrovinsky, L., Dubrovinskaia, N., Prakapenka, V. B. & Abakumov, A. M. Implementation of micro-ball nanodiamond anvils for high-pressure studies above 6[thinsp]Mbar. *Nat Commun* **3**, 1163,

- doi:http://www.nature.com/ncomms/journal/v3/n10/supinfo/ncomms2160_S1.html
(2012).
- 28 Nayak, A. P. *et al.* Pressure-induced semiconducting to metallic transition in multilayered molybdenum disulphide. *Nat Commun* **5**, 1-9 (2014).
- 29 Zhu, J. *et al.* Superconductivity in Topological Insulator Sb₂Te₃ Induced by Pressure. *Sci. Rep.* **3**, doi:10.1038/srep02016 (2013).
- 30 Bandaru, N. *et al.* Effect of Pressure and Temperature on Structural Stability of MoS₂. *The Journal of Physical Chemistry C* **118**, 3230-3235, doi:10.1021/jp410167k (2014).
- 31 Ci, L. *et al.* Atomic layers of hybridized boron nitride and graphene domains. *Nat Mater* **9**, 430-435,
doi:<http://www.nature.com/nmat/journal/v9/n5/abs/nmat2711.html#supplementary-information> (2010).
- 32 Terrones, M. *et al.* Experimental and Theoretical Studies Suggesting the Possibility of Metallic Boron Nitride Edges in Porous Nanourchins. *Nano Letters* **8**, 1026-1032,
doi:10.1021/nl072713m (2008).
- 33 Gierz, I., Riedl, C., Starke, U., Ast, C. R. & Kern, K. Atomic Hole Doping of Graphene. *Nano Letters* **8**, 4603-4607, doi:10.1021/nl802996s (2008).
- 34 Koehler, F. M., Jacobsen, A., Ensslin, K., Stampfer, C. & Stark, W. J. Selective Chemical Modification of Graphene Surfaces: Distinction Between Single- and Bilayer Graphene. *Small* **6**, 1125-1130, doi:10.1002/sml.200902370 (2010).
- 35 Dean, C. R. *et al.* Boron nitride substrates for high-quality graphene electronics. *Nat Nano* **5**, 722-726,

- doi:<http://www.nature.com/nnano/journal/v5/n10/abs/nnano.2010.172.html#supplementary-information> (2010).
- 36 Miremadi, B. K. & Morrison, S. R. The intercalation and exfoliation of tungsten disulfide. *Journal of Applied Physics* **63**, 4970-4974, doi:10.1063/1.340441 (1988).
- 37 Zhi, C., Bando, Y., Tang, C., Kuwahara, H. & Golberg, D. Large-Scale Fabrication of Boron Nitride Nanosheets and Their Utilization in Polymeric Composites with Improved Thermal and Mechanical Properties. *Advanced Materials* **21**, 2889-2893, doi:10.1002/adma.200900323 (2009).
- 38 Han, W.-Q., Wu, L., Zhu, Y., Watanabe, K. & Taniguchi, T. Structure of chemically derived mono- and few-atomic-layer boron nitride sheets. *Applied Physics Letters* **93**, 223103-223103 (2008).
- 39 Lin, Y. *et al.* Aqueous Dispersions of Few-Layered and Monolayered Hexagonal Boron Nitride Nanosheets from Sonication-Assisted Hydrolysis: Critical Role of Water. *The Journal of Physical Chemistry C* **115**, 2679-2685, doi:10.1021/jp110985w (2011).
- 40 Lee, C. H., Zhang, D. & Yap, Y. K. Functionalization, Dispersion, and Cutting of Boron Nitride Nanotubes in Water. *The Journal of Physical Chemistry C* **116**, 1798-1804, doi:10.1021/jp2112999 (2011).
- 41 Wang, Q. H., Kalantar-Zadeh, K., Kis, A., Coleman, J. N. & Strano, M. S. Electronics and optoelectronics of two-dimensional transition metal dichalcogenides. *Nature nanotechnology* **7**, 699-712 (2012).
- 42 Butler, S. Z. *et al.* Progress, Challenges, and Opportunities in Two-Dimensional Materials Beyond Graphene. *ACS Nano* **7**, 2898-2926, doi:10.1021/nn400280c (2013).

- 43 Fontana, M. *et al.* Electron-hole transport and photovoltaic effect in gated MoS₂ Schottky junctions. *Sci. Rep.* **3** (2013).
- 44 Yin, Z. *et al.* Single-Layer MoS₂ Phototransistors. *ACS Nano* **6**, 74-80, doi:10.1021/nm2024557 (2011).
- 45 Lee, H. S. *et al.* MoS₂ Nanosheet Phototransistors with Thickness-Modulated Optical Energy Gap. *Nano Letters* **12**, 3695-3700, doi:10.1021/nl301485q (2012).
- 46 Behnia, K. Condensed-matter physics: Polarized light boosts valleytronics. *Nat Nano* **7**, 488-489 (2012).
- 47 Zeng, H., Dai, J., Yao, W., Xiao, D. & Cui, X. Valley polarization in MoS₂ monolayers by optical pumping. *Nat Nano* **7**, 490-493 (2012).
- 48 Ghorbani-Asl, M. *et al.* Electromechanics in MoS₂ and WS₂: nanotubes vs. monolayers. *Sci. Rep.* **3**, doi:10.1038/srep02961 (2013).
- 49 Cheiwchanchamnangij, T. & Lambrecht, W. R. L. Quasiparticle band structure calculation of monolayer, bilayer, and bulk MoS₂. *Physical Review B* **85**, 205302 (2012).
- 50 Splendiani, A. *et al.* Emerging Photoluminescence in Monolayer MoS₂. *Nano Letters* **10**, 1271-1275, doi:10.1021/nl903868w (2010).
- 51 Sachs, B. *et al.* Doping Mechanisms in Graphene-MoS₂ Hybrids. *ArXiv e-prints* **1304**, 2236 (2013).
- 52 Ataca, C., Şahin, H., Aktürk, E. & Ciraci, S. Mechanical and Electronic Properties of MoS₂ Nanoribbons and Their Defects. *The Journal of Physical Chemistry C* **115**, 3934-3941, doi:10.1021/jp1115146 (2011).

- 53 Tongay, S. *et al.* Thermally Driven Crossover from Indirect toward Direct Bandgap in 2D Semiconductors: MoSe₂ versus MoS₂. *Nano Letters* **12**, 5576-5580, doi:10.1021/nl302584w (2012).
- 54 Eda, G. *et al.* Photoluminescence from Chemically Exfoliated MoS₂. *Nano Letters* **11**, 5111-5116, doi:10.1021/nl201874w (2011).
- 55 Ataca, C. & Ciraci, S. Functionalization of Single-Layer MoS₂ Honeycomb Structures. *The Journal of Physical Chemistry C* **115**, 13303-13311, doi:10.1021/jp2000442 (2011).
- 56 Qiu, H. *et al.* Hopping transport through defect-induced localized states in molybdenum disulphide. *Nat Commun* **4**, doi:10.1038/ncomms3642 (2013).
- 57 Fu, D. *et al.* Mechanically modulated tunneling resistance in monolayer MoS₂. *Applied Physics Letters* **103**, - (2013).
- 58 Johari, P. & Shenoy, V. B. Tuning the Electronic Properties of Semiconducting Transition Metal Dichalcogenides by Applying Mechanical Strains. *ACS Nano* **6**, 5449-5456, doi:10.1021/nl301320r (2012).
- 59 Wei, L., Jun-fang, C., Qinyu, H. & Teng, W. Electronic and elastic properties of MoS₂. *Physica B: Condensed Matter* **405**, 2498-2502, doi:10.1016/j.physb.2010.03.022 (2010).
- 60 Dave, M., Vaidya, R., Patel, S. G. & Jani, A. R. High pressure effect on MoS₂ and MoSe₂ single crystals grown by CVT method. *Bulletin of Materials Science* **27**, 213-216 (2004).
- 61 Hromadová, L., Martoňák, R. & Tosatti, E. Structure change, layer sliding, and metallization in high-pressure MoS₂. *Physical Review B* **87**, 144105 (2013).

- 62 Castro Neto, A. H. Charge Density Wave, Superconductivity, and Anomalous Metallic Behavior in 2D Transition Metal Dichalcogenides. *Physical Review Letters* **86**, 4382-4385 (2001).
- 63 Nayak, A. P. *et al.* Pressure-induced semiconducting to metallic transition in multilayered molybdenum disulphide. *Nat Commun* **5**, doi:10.1038/ncomms4731 (2014).
- 64 Siegrist, T. *et al.* Disorder-induced localization in crystalline phase-change materials. *Nat Mater* **10**, 202-208 (2011).
- 65 Thouless, D. Anderson localization in the seventies and beyond. *International Journal of Modern Physics B* **24**, 1507-1525, doi:doi:10.1142/S0217979210064496 (2010).
- 66 Jo, S., Ubrig, N., Berger, H., Kuzmenko, A. B. & Morpurgo, A. F. Mono- and Bilayer WS₂ Light-Emitting Transistors. *Nano Letters* **14**, 2019-2025, doi:10.1021/nl500171v (2014).
- 67 He, J. *et al.* Electron transfer and coupling in graphene–tungsten disulfide van der Waals heterostructures. *Nat Commun* **5**, doi:10.1038/ncomms6622 (2014).
- 68 Gandi, A. N. & Schwingenschlögl, U. WS₂ As an Excellent High-Temperature Thermoelectric Material. *Chemistry of Materials* **26**, 6628-6637, doi:10.1021/cm503487n (2014).
- 69 Ovchinnikov, D., Allain, A., Huang, Y.-S., Dumcenco, D. & Kis, A. Electrical Transport Properties of Single-Layer WS₂. *ACS Nano* **8**, 8174-8181, doi:10.1021/nn502362b (2014).
- 70 Dong, L. *et al.* Theoretical study on strain induced variations in electronic properties of 2H-MoS₂ bilayer sheets. *Applied Physics Letters* **104** (2014).

- 71 Liu, B. *et al.* Pressure Induced Semiconductor-Semimetal Transition in WSe₂. *The Journal of Physical Chemistry C* **114**, 14251-14254, doi:10.1021/jp104143e (2010).
- 72 Proctor, J. E. *et al.* High-pressure Raman spectroscopy of graphene. *Physical Review B* **80**, 073408 (2009).
- 73 Jayaraman, A. Diamond anvil cell and high-pressure physical investigations. *Reviews of Modern Physics* **55**, 65-108 (1983).
- 74 Ashcroft, N. W. & Mermin, N. D. Solid State Physics. *Rinehart and Winston, New York* **19761** (1976).
- 75 Yue, Q. *et al.* Mechanical and electronic properties of monolayer MoS₂ under elastic strain. *Physics Letters A* **376**, 1166-1170 (2012).
- 76 Lee, C. *et al.* Anomalous Lattice Vibrations of Single- and Few-Layer MoS₂. *ACS Nano* **4**, 2695-2700, doi:10.1021/nn1003937 (2010).
- 77 Livneh, T. & Sterer, E. Resonant Raman scattering at exciton states tuned by pressure and temperature in 2H-MoS₂. *Physical Review B* **81**, 195209-195209, doi:10.1103/PhysRevB.81.195209 (2010).
- 78 Molina-Sánchez, A. & Wirtz, L. Phonons in single-layer and few-layer MoS₂ and WS₂. *Physical Review B* **84**, 155413 (2011).
- 79 Livneh, T. & Sterer, E. Resonant Raman scattering at exciton states tuned by pressure and temperature in 2H-MoS₂. *Physical Review B* **81**, 195209 (2010).
- 80 Nicolle, J., Machon, D., Poncharal, P., Pierre-Louis, O. & San-Miguel, A. Pressure-Mediated Doping in Graphene. *Nano Letters* **11**, 3564-3568, doi:10.1021/nl201243c (2011).

- 81 Conley, H. J. *et al.* Bandgap Engineering of Strained Monolayer and Bilayer MoS₂. *Nano Letters* **13**, 3626-3630, doi:10.1021/nl4014748 (2013).
- 82 Mittal, R. *et al.* Phonon Softening and Pressure-Induced Phase Transitions in Quartz Structured Compound, FePO₄. *arXiv preprint arXiv:0903.1550* (2009).
- 83 Hearn, C. J. Phonon softening and the metal-insulator transition in VO₂. *Journal of Physics C: Solid State Physics* **5**, 1317 (1972).
- 84 Yan, J., Henriksen, E. A., Kim, P. & Pinczuk, A. Observation of Anomalous Phonon Softening in Bilayer Graphene. *Physical Review Letters* **101**, 136804 (2008).
- 85 Huang, M. *et al.* Phonon softening and crystallographic orientation of strained graphene studied by Raman spectroscopy. *Proceedings of the National Academy of Sciences* **106**, 7304-7308, doi:10.1073/pnas.0811754106 (2009).
- 86 Kudo, K., Takasuga, M., Okamoto, Y., Hiroi, Z. & Nohara, M. Giant Phonon Softening and Enhancement of Superconductivity by Phosphorus Doping of BaNi₂As₂. *Physical Review Letters* **109**, 097002 (2012).
- 87 Bera, A. *et al.* Sharp Raman Anomalies and Broken Adiabaticity at a Pressure Induced Transition from Band to Topological Insulator in Sb₂Se₃. *Physical Review Letters* **110**, 107401 (2013).
- 88 Kam, K. K. & Parkinson, B. A. Detailed photocurrent spectroscopy of the semiconducting group VIB transition metal dichalcogenides. *The Journal of Physical Chemistry* **86**, 463-467, doi:10.1021/j100393a010 (1982).
- 89 Perdew, J. P. & Zunger, A. Self-interaction correction to density-functional approximations for many-electron systems. *Physical Review B* **23**, 5048-5079 (1981).

- 90 Heyd, J., Scuseria, G. E. & Ernzerhof, M. Hybrid functionals based on a screened Coulomb potential. *The Journal of Chemical Physics* **118**, 8207-8215 (2003).
- 91 Hedin, L. New Method for Calculating the One-Particle Green's Function with Application to the Electron-Gas Problem. *Physical Review* **139**, A796-A823 (1965).
- 92 Von Dreere, R. B. & Larson, A. C. General structure analysis system. *Regents of the University of California* (2001).
- 93 Kobayashi, H., Takeshita, N., Mōri, N., Takahashi, H. & Kamimura, T. Pressure-induced semiconductor-metal-semiconductor transitions in FeS. *Physical Review B* **63**, 115203 (2001).
- 94 Feinleib, J. & Paul, W. Semiconductor-To-Metal Transition in V₂O₃. *Physical Review* **155**, 841-850 (1967).
- 95 Berglund, C. N. & Guggenheim, H. J. Electronic Properties of VO₂ near the Semiconductor-Metal Transition. *Physical Review* **185**, 1022-1033 (1969).
- 96 Kudo, K., Takasuga, M., Okamoto, Y., Hiroi, Z. & Nohara, M. Giant Phonon Softening and Enhancement of Superconductivity by Phosphorus Doping of BaNi₂As₂. *Physical Review Letters* **109**, 097002 (2012).
- 97 Bera, A. *et al.* Sharp Raman Anomalies and Broken Adiabaticity at a Pressure Induced Transition from Band to Topological Insulator in Sb₂Se₃. *Physical Review Letters* **110**, 107401 (2013).
- 98 Aksoy, R. *et al.* X-ray diffraction study of molybdenum disulfide to 38.8 GPa. *Journal of Physics and Chemistry of Solids* **67**, 1914-1917 (2006).
- 99 Mak, K. F., Lee, C., Hone, J., Shan, J. & Heinz, T. F. Atomically Thin MoS₂: A New Direct-Gap Semiconductor. *Physical Review Letters* **105**, 136805 (2010).

- 100 Chhowalla, M. *et al.* The chemistry of two-dimensional layered transition metal dichalcogenide nanosheets. *Nat Chem* **5**, 263-275 (2013).
- 101 Artyukhov, V. I., Liu, M. & Yakobson, B. I. Mechanically Induced Metal–Insulator Transition in Carbyne. *Nano Letters* **14**, 4224-4229, doi:10.1021/nl5017317 (2014).
- 102 Chang, H.-Y. *et al.* High-Performance, Highly Bendable MoS₂ Transistors with High-K Dielectrics for Flexible Low-Power Systems. *ACS Nano* **7**, 5446-5452, doi:10.1021/nn401429w (2013).
- 103 Restrepo, O. D., Mishra, R., Goldberger, J. E. & Windl, W. Tunable gaps and enhanced mobilities in strain-engineered silicane. *Journal of Applied Physics* **115**, -, doi:doi:http://dx.doi.org/10.1063/1.4860988 (2014).
- 104 Frank, O. *et al.* Development of a universal stress sensor for graphene and carbon fibres. *Nat Commun* **2**, 255 (2011).
- 105 Dou, X., Ding, K., Jiang, D. & Sun, B. Tuning and Identification of Interband Transitions in Monolayer and Bilayer Molybdenum Disulfide Using Hydrostatic Pressure. *ACS Nano* **8**, 7458-7464 (2014).
- 106 Pérez Garza, H. H., Kievit, E. W., Schneider, G. F. & Staufer, U. Controlled, Reversible, and Nondestructive Generation of Uniaxial Extreme Strains (>10%) in Graphene. *Nano Letters* **14**, 4107–4113 (2014).
- 107 Hui, Y. Y. *et al.* Exceptional Tunability of Band Energy in a Compressively Strained Trilayer MoS₂ Sheet. *ACS Nano* **7**, 7126-7131 (2013).
- 108 Najmaei, S. *et al.* Tailoring the Physical Properties of Molybdenum Disulfide Monolayers by Control of Interfacial Chemistry. *Nano Letters* **14**, 1354-1361, doi:10.1021/nl404396p (2014).

- 109 Ganatra, R. & Zhang, Q. Few-Layer MoS₂: A Promising Layered Semiconductor. *ACS Nano* **8**, 4074-4099 (2014).
- 110 Lee, J. *et al.* Multi-finger flexible graphene field effect transistors with high bendability. *Applied Physics Letters* **101**, -, doi:doi:http://dx.doi.org/10.1063/1.4772541 (2012).
- 111 Duerloo, K.-A. N., Li, Y. & Reed, E. J. Structural phase transitions in two-dimensional Mo- and W-dichalcogenide monolayers. *Nat Commun* **5**, 1-9, doi:10.1038/ncomms5214 (2014).
- 112 Bissett, M. A., Tsuji, M. & Ago, H. Strain engineering the properties of graphene and other two-dimensional crystals. *Physical Chemistry Chemical Physics* **16**, 11124-11138 (2014).
- 113 Guo, H., Lu, N., Wang, L., Wu, X. & Zeng, X. C. Tuning Electronic and Magnetic Properties of Early Transition-Metal Dichalcogenides via Tensile Strain. *The Journal of Physical Chemistry C* **118**, 7242-7249 (2014).
- 114 Chen, Y. *et al.* Tunable Band Gap Photoluminescence from Atomically Thin Transition-Metal Dichalcogenide Alloys. *ACS Nano* **7**, 4610-4616, doi:10.1021/nn401420h (2013).
- 115 Espejo, C., Rangel, T., Romero, A. H., Gonze, X. & Rignanese, G. M. Band structure tunability in MoS₂ under interlayer compression: A DFT and GW study. *Physical Review B* **87**, 245114 (2013).
- 116 Terrones, H. *et al.* New First Order Raman-active Modes in Few Layered Transition Metal Dichalcogenides. *Sci. Rep.* **4**, 1-9 (2014).
- 117 Sugai, S. & Ueda, T. High-pressure Raman spectroscopy in the layered materials 2H-MoS₂, 2H-MoSe₂, and 2H-MoTe₂. *Physical Review B* **26**, 6554-6558 (1982).

- 118 Aksoy, R., Selvi, E. & Ma, Y. X-ray diffraction study of molybdenum diselenide to 35.9GPa. *Journal of Physics and Chemistry of Solids* **69**, 2138-2140 (2008).
- 119 Chi, Z.-H. *et al.* Pressure-Induced Metallization of Molybdenum Disulfide. *Physical Review Letters* **113**, 036802 (2014).
- 120 Sercombe, D. *et al.* Optical investigation of the natural electron doping in thin MoS₂ films deposited on dielectric substrates. *Sci. Rep.* **3**, 1-6 (2013).
- 121 Ling, X. *et al.* Raman Enhancement Effect on Two-Dimensional Layered Materials: Graphene, h-BN and MoS₂. *Nano Letters* **14**, 3033-3040, doi:10.1021/nl404610c (2014).
- 122 Li, H. *et al.* From Bulk to Monolayer MoS₂: Evolution of Raman Scattering. *Advanced Functional Materials* **22**, 1385-1390 (2012).
- 123 Jiménez Sandoval, S., Yang, D., Frindt, R. F. & Irwin, J. C. Raman study and lattice dynamics of single molecular layers of MoS₂. *Physical Review B* **44**, 3955-3962 (1991).
- 124 Calandra, M. Chemically exfoliated single-layer MoS₂: Stability, lattice dynamics, and catalytic adsorption from first principles. *Physical Review B* **88**, 245428 (2013).
- 125 Tongay, S. *et al.* Monolayer behaviour in bulk ReS₂ due to electronic and vibrational decoupling. *Nat Commun* **5**, 1-6 (2014).
- 126 Castellanos-Gomez, A. *et al.* Local Strain Engineering in Atomically Thin MoS₂. *Nano Letters* **13**, 5361-5366 (2013).
- 127 Tsai, D.-S. *et al.* Few-Layer MoS₂ with High Broadband Photogain and Fast Optical Switching for Use in Harsh Environments. *ACS Nano* **7**, 3905-3911, doi:10.1021/nn305301b (2013).
- 128 Iqbal, M. W. *et al.* Deep-ultraviolet-light-driven reversible doping of WS₂ field-effect transistors. *Nanoscale* **7**, 747-757, doi:10.1039/C4NR05129G (2015).

- 129 Ohuchi, F. S., Jaegermann, W., Pettenkofer, C. & Parkinson, B. A. Semiconductor to metal transition of WS₂ induced by K intercalation in ultrahigh vacuum. *Langmuir* **5**, 439-442, doi:10.1021/la00086a026 (1989).
- 130 Georgiou, T. *et al.* Electrical and optical characterization of atomically thin WS₂. *Dalton Transactions* **43**, 10388-10391, doi:10.1039/C3DT52353E (2014).
- 131 Yen, P. C., Huang, Y. S. & Tiong, K. K. The growth and characterization of rhenium-doped WS₂ single crystals. *Journal of Physics: Condensed Matter* **16**, 2171 (2004).
- 132 Gutiérrez, H. R. *et al.* Extraordinary Room-Temperature Photoluminescence in Triangular WS₂ Monolayers. *Nano Letters* **13**, 3447-3454, doi:10.1021/nl3026357 (2012).
- 133 Voiry, D. *et al.* Enhanced catalytic activity in strained chemically exfoliated WS₂ nanosheets for hydrogen evolution. *Nat Mater* **12**, 850-855, doi:10.1038/nmat3700 (2013).
- 134 Stretman, B. G. *Solid state electronic devices*. (Pearson Education, Limited, 1972).
- 135 Li-na, Z. *et al.* Microstructure and tribological properties of WS₂/MoS₂ multilayer films. *Applied Surface Science* **258**, 1944-1948, doi:10.1016/j.apsusc.2011.06.148 (2012).
- 136 Cao, B. & Li, T. Interlayer Electronic Coupling in Arbitrarily Stacked MoS₂ Bilayers Controlled by Interlayer S–S Interaction. *The Journal of Physical Chemistry C* **119**, 1247-1252, doi:10.1021/jp5101736 (2015).
- 137 van der Pauw, L. J. A method of measuring specific resistivity and Hall effect of discs of arbitrary shape. *Philips Res. Rep.* **13**, 1 (1958).

- 138 Braga, D., Gutiérrez Lezama, I., Berger, H. & Morpurgo, A. F. Quantitative Determination of the Band Gap of WS₂ with Ambipolar Ionic Liquid-Gated Transistors. *Nano Letters* **12**, 5218-5223, doi:10.1021/nl302389d (2012).
- 139 Berkdemir, A. *et al.* Identification of individual and few layers of WS₂ using Raman Spectroscopy. *Sci. Rep.* **3**, doi:10.1038/srep01755 (2013).
- 140 Laskar, M. R. *et al.* p-type doping of MoS₂ thin films using Nb. *Applied Physics Letters* **104**, -, doi:10.1063/1.4867197 (2014).
- 141 Bandaru, N. *et al.* Structural stability of WS₂ under high pressure. *International Journal of Modern Physics B* **28**, 1450168, doi:doi:10.1142/S0217979214501689 (2014).
- 142 M, T. & Late, D. J. Temperature Dependent Phonon Shifts in Single-Layer WS₂. *ACS Applied Materials & Interfaces* **6**, 1158-1163, doi:10.1021/am404847d (2013).
- 143 Late, D. J., Shirodkar, S. N., Waghmare, U. V., Dravid, V. P. & Rao, C. N. R. Thermal Expansion, Anharmonicity and Temperature-Dependent Raman Spectra of Single- and Few-Layer MoSe₂ and WSe₂. *ChemPhysChem* **15**, 1592-1598, doi:10.1002/cphc.201400020 (2014).
- 144 Schroder, D. K. *Semiconductor material and device characterization*. (John Wiley & Sons, 2006).